Characterizing Conformational Dynamics and Catalytic Activity of Enzymes by Hydrogen-Deuterium Exchange Mass Spectrometry

Ruth Aurora Knox

A DISSERTATION SUBMITTED TO THE FACULTY OF GRADUATE STUDIES IN PARTIAL FULFILLMENT OF THE REQUIREMENTS FOR THE DEGREE OF

DOCTOR OF PHILOSOPHY

GRADUATE PROGRAM IN CHEMISTRY
YORK UNIVERSITY
TORONTO, ONTARIO

June 2019

ABSTRACT

Determining the conformational dynamics of enzymes as they undergo catalysis has been challenging for decades due to the short timescale and limitations of traditional analysis, including techniques such as CPMG 2D NMR and X-ray crystallography. Herein is the study of two proteins: TEM-1 β-lactamase, the most common enzyme responsible for the hydrolysis of antibiotics in gram-negative bacteria, and yeast alcohol dehydrogenase (YADH), responsible for facilitating the hydride transfer to NAD^+ for energy production in prokaryotes. In the catalysis of both antibiotics and NAD^+ reduction the specific residues involved in each binding mode remain under debate. By using a microfluidics workflow and an adjustable reaction volume, time resolved HDX experimentation was used to monitor deuteration events concurrently with catalytic activity on the millisecond to second timescale. Native mass spectrometry enabled studies into binding affinity and monitoring of substrate inactivation on a measured time course. Ion mobility mass spectrometry (IM-MS) was used to provide definitive MS/MS results for protein coverage and prov ide spatial resolution for all protein/substrate complexes. Additionally, collision induced unfolding (CIU) within the ion mobility cell provides a comparative binding affinity scale for the inhibitory drugs used in the study of TEM-1. Using this wide range of analytical techniques facilitated important discoveries including the isolation of specific residues of TEM-1 mapped to their involvement in different binding modes during catalysis, and subsequently the differentiation in inactivation pathways depending on substrate concentration and type. Further work has isolated residues involved in the turnover event of NAD^+ along with residues that display a significant decrease in dynamics with the catalysis of deuterated ethanol compared to the non-deuterated ethanol.

ACKNOWLEDGMENTS

First and foremost, I would like to express my thanks to Dr. Derek Wilson, who welcomed me into his lab knowing that I had little background in bioanalytical chemistry but was willing to learn quickly. Thanks also to my committee members, Dr. Demian Ifa and Dr. Gerald Audette, who challenged me to think critically and helped me problem solve in the first couple of years of my experiments. Time has passed quickly but I am so grateful to have learned extensively about mass spectrometry techniques from such an insightful mentor and group. Thank you to the Wilson group members, Kerene Brown, Cristina Lento, Dr. Shaolong Zhu, Dr. Peter Liuni, Irina Oganesyan, Xiaojing Huang, Lisa Szymkowicz, Lucienne Nouchikian, Dr. Bin Deng and John van Nostrand. In particular I wanted to thank Cristina Lento, Kerene Brown and Shaolong Zhu, three mentors that were instrumental in teaching me the basics of cell culturing and the components of the mass spectrometers. This thesis is dedicated to my parents, Bill Knox and Yola Grant, for their continuous support of my unending educational process; my supportive friends, Lily Spare and Nick MacFarlane, who helped me get through the tougher times and kept me hopeful, and to my idol, Beyoncé Giselle Knowles Carter, my biggest inspiration.

TABLE OF CONTENTS

Abstract----ii

Acknowledgements----iii

Table of Contents----iv

List of Figures----vii

List of Abbreviations----ix

List of Publications----x

Chapter 1: Introduction----1

1.1. Mass Spectrometry----1

1.1.1. Electrospray Ionization----1

1.1.2. Nanoelectrospray Ionization----6

1.1.3. Mechanism of Electrospray Ionization----6

1.1.4. Quadrupole Time-of-Flight Mass Spectrometers----9

1.2. Ion-Mobility Spectrometry- Introduction----14

1.2.1. Collision Induced Unfolding----16

1.2.2. Traveling-Wave Ion Mobility Spectrometry----17

1.3. Hydrogen Deuterium Exchange----19

1.3.1. Fundamental Theory----20

1.3.2. Pulsed vs. Continuous Labelling Experiments----25

1.3.3. Time-Resolved Hydrogen Deuterium Exchange----26

1.3.4. Microfluidic Devices for Hydrogen Deuterium Exchange----28

1.4. Enzymes Producing Antimicrobial Resistance----29

1.4.1. Antibiotic Drug Development----29

1.4.2. Role of Penicillin Binding Proteins in Bacterial Cells----30

1.4.3. Generation of β-lactam Antibiotics----32

1.4.3.1. Differences in Antibiotic Families----32

1.4.4. Evolution of β-lactamases----34

1.4.4.1. TEM-1 β-lactamase Introduction----35

1.5. Enzymes Involved in Energy Metabolism----36

1.5.1. Energy Formation in Prokaryotes and Lower Eukaryotes----36

1.5.2. NAD^+ and NADH Background----37

1.5.3. Yeast Alcohol Dehydrogenase----39

1.5.3.1. Hydride Transfer and Tunneling----39

1.5.3.2. Kinetic Isotope Effect on Catalysis of Yeast Alcohol Dehydrogenase----40

1.5.3.3. Mechanism of Catalysis----------40
1.6. Research Objectives----------41

Chapter 2: Mapping Conformational Dynamics to Individual Steps in the TEM-1 β-Lactamase Catalytic Mechanism ----------43

2.1. Summary----------44
2.2. Introduction----------44
2.3. Results and Discussion----------47
2.3.1. Native MS of TEM-1 and Formation of Acyl-enzyme Intermediates----------47
2.3.2. TEM-1 Conformational Dynamics in the Presence of Substrate, Partial Inhibitor and Covalent Inhibitors----------48
2.3.3. Backbone Dynamics of TEM-1 during Binding----------52
2.3.4. Backbone Dynamics of TEM-1 during Productive Acylation----------54
2.3.5. Backbone Dynamics of TEM-1 during Slow Deacylation----------56
2.3.6. Backbone Dynamics of TEM-1 during Deacylation Failure----------57
2.4. Conclusion----------59
2.5. Methods----------60
2.5.1. Expression and Purification of TEM-1 β-lactamase----------61
2.5.2. Digest Preparation----------61
2.5.3. Chip Design----------61
2.5.4. Microfluidics Workflow----------62
2.5.5. Data Analysis----------63

Chapter 3: Collision-Induced Unfolding and Hydrogen/Deuterium Exchange Mass Spectrometry as Tools for Comparing Binding Affinity of TEM-1 β-lactamase Inhibitors --64

3.1. Summary----------65
3.2. Introduction----------65
3.3. Results----------68
3.3.1. Measuring Inhibitor Byproduct Formation by Mass Spectrometry----------69
3.3.2. Local HDX Coverage of TEM-1 β-lactamase----------73
3.3.3. Comparison of Inhibitor Binding Affinity by Collision Induced Unfolding Mass Spectrometry----------75
3.4. Discussion----------79
3.5. Conclusions----------80
3.6. Methods----------81
3.6.1. Collision Induced Unfolding Mass Spectrometry of TEM-1 with Inhibitor Substrates----------81
3.6.2. Native Mass Spectrometry of Inhibitor Binding----------81

3.6.3. Data Analysis of Global and Local HDX----------82

Chapter 4: Monitoring Catalysis and Associated Conformational Effects in Yeast Alcohol Dehydrogenase by Millisecond-Scale HDX Mass Spectrometry ----------83

4.1. Summary----------84
4.2. Introduction----------84
4.3. Results----------86
4.3.1. Optimization of the Oligomeric YADH----------88
4.3.2. Global HDX of YADH Catalysis----------90
4.3.3. Local HDX of YADH Catalysis----------94
4.4. Discussion----------97
4.4.1. The Structural Implications of NAD^+ Docking----------97
4.4.2. Subtleties in Local Dynamics During Catalysis----------99
4.5. **Conclusions----------102**
4.6. **Methods----------103**
4.6.1. Oligomeric Optimization Through Back Pressure Manipulation----------103
4.6.2. Global HDX of YADH----------103
4.6.3. Local HDX Workflow----------104

Chapter 5: Conclusions and Future Work----------105
5.1. Summary----------106
5.2. Future Work----------108
5.2.1. Combatting Drug Resistance in Tropical Medicine----------108
5.2.2. Leishmania Overview----------109
5.2.3. Microfluidic Design Proposal for Changing Environmental Conditions----------109
5.2.4. Microfluidic Design Proposal for Simultaneous Host Environment Diagnostics-110

References----------112

Appendix A: Supplemental Figures for Chapter 2----------139

Appendix B: Supplemental Figures for Chapter 3----------145

LIST OF FIGURES

Figure 1.1: Magnification of Electrospray Ionization Droplet Formation in Positive Ion Mode

Figure 1.2: Electrospray Ionization Evaporation Models

Figure 1.3: Quadrupole Ion Separation

Figure 1.4: A Schematic of IM-MS Used to Differentiate Ligand Binding to Large Protein Complexes on a Synapt G2

Figure 1.5: Cross Section of a Travelling-Wave IMS Collision Cell with various CCS

Figure 1.6: Schematic of a Bottom-up Proteomics HDX Workflow

Figure 1.7: Schematic of Acid (B and C) and Base (A)-catalyzed Hydrogen/Deuterium Exchange Reaction Mechanisms with Backbone Amides

Figure 1.8: A Chevron Plot of $\log k_{ex}$ vs pH for two Peptides, poly-D, L-alanine (PDLA) and poly-D, L-lysine (PDLL) Protium/Tritium Exchange Reactions

Figure 1.9: Schematic of the Wilson Group Time-Resolved HDX Capillary Workflow

Figure 1.10: Schematic of a New Generation Microfluidics Chip

Figure 1.11: Mechanism of Peptidoglycan Formation by Penicillin Binding Proteins in the Cell

Figure 1.12: Chemical Structures of β-lactam Antibiotics Currently on the Market

Figure 1.13: TEM-1 Crystal Structure with 3 Drug Families used in TRESI-HDX Experiments

Figure 1.14: NAD-facilitated Ethanol Oxidation

Figure 1.15: Yeast Alcohol Dehydrogenase Bi-bi Mechanism of the Catalytic Cycle

Figure 2.1: Schematic Depiction of the TRESI-HDX Experimental Setup

Figure 2.2: Native Mass Spectra of TEM-1 Binding Clavulanate

Figure 2.3: Time-Resolved Deuterium Uptake for TEM-1 with 3 Substrates

Figure 2.4: Kinetic Deuterium Uptake for Binding Dynamics of TEM-1

Figure 2.5: Kinetic Deuterium Uptake for Acylation and Deacylation Dynamics of TEM-1

Figure 2.6: Kinetic Deuterium Uptake for Inhibition Dynamics of TEM-1

Figure 3.1: TEM-1 Inhibitors and Potential Fragmentation Products

Figure 3.2: Native Mass Spectrometry Inhibitor Binding Study With 1000:1 Ratio

Figure 3.3: Native Mass Spectrometry Inhibitor Binding Study With 10:1 Ratio

Figure 3.4: Deuterium Uptake Plot for 1000:1 Incubation with Inhibitors

Figure 3.5: Local HDX Workflow for TRESI-HDX and IMS-MS Experiments

Figure 3.6: CIU Heat Maps of Binding Affinity for TEM-1 and Inhibitors with a 1000:1 Ratio of Inhibitor to TEM-1.

Figure 3.7 CIU Heat Maps of Binding Affinity for TEM-1 and Inhibitors with a 10:1 Ratio of Inhibitor to TEM-1.

Figure 4.1: Schematic of Residues of Interest in Reduction of NAD^+ to NADH

Figure 4.2: Optimization of Oligomeric Forms of Yeast Alcohol Dehydrogenase

Figure 4.3: Global HDX results for $(NAD^+)_2$ occupied YADH

Figure 4.4: Global HDX Results for YADH with $(NAD^+)_4$ Occupancy During Catalysis

Figure 4.5: Single Time Point Local HDX Results for EtOH Catalysis

Figure 4.6: Single Time Point Local HDX Results for D_2-EtOH Catalysis

Figure 4.7: Rigidification of YADH with NAD^+ Incubation

Figure 4.8: Isolation of Dynamics Associated with the Deuterated Ethanol During Catalysis

LIST OF ABBREVIATIONS

AA: Amino acid

CIU: Collision Induced Unfolding

%CV: Percent Coefficient of Variation

Da: Daltons

D_2O: Deuterium Oxide

E. coli: Escherichia coli

ESBL: Extended Spectrum β-lactamase

ESI: ElectroSpray Ionization

HDX: Hydrogen-Deuterium Exchange

HDX-MS: Hydrogen-Deuterium Exchange Mass Spectrometry

IMS: Ion-Mobility Spectrometry

IPTG: Isopropyl β-D-1-thiogalactopyranoside

kDA: kilo Daltons

LC-MS: Liquid Chromatography Mass Spectrometry

MS: Mass Spectrometry

MW: Molecular Weight

n: Number of Replicates

NMR: Nuclear Magnetic Resonance

OD_{600}: Optical Density at 600nm

PBP: Penicillin Binding Protein

pI: Isoelectric point

PMMA: Poly (methyl methacrylate)

Q-ToF: Quadrupole Time-of-Flight Mass Analyzer

SDS-PAGE: Sodium Dodecyl Sulfate Polyacrylamide Gel Electrophoresis

TRESI: Time-Resolved ElectroSpray Ionization

UV: Ultra Violet

LIST OF PUBLICATIONS

1) **Knox R**, Wilson DJ “Yeast Alcohol Dehydrogenase as a Model Enzyme for Monitoring Catalysis and Cooperative Binding by Millisecond-Scale HDX Mass Spectrometry” (*in preparation*)
2) **Knox R**, Wilson DJ “Collision-Induced Unfolding and Hydrogen/Deuterium Exchange Mass Spectrometry as Tools for Quantitating Binding Affinity of TEM-1 β-lactamase Inhibitors” (*in preparation*)
3) **Knox R**, Lento C, and Wilson DJ (2018) "Mapping conformational dynamics to individual steps in the TEM-1 β-Lactamase catalytic mechanism", Journal of Molecular Biology, 430, 3311-3322.
4) Lento C, Zhu S, Brown KA, **Knox R**, Liuni P, and Wilson DJ (2017) "Time-resolved ElectroSpray Ionization Hydrogen-deuterium Exchange Mass Spectrometry for Studying Protein Structure and Dynamics", Journal of Visualized Experiments, 122.

1. Introduction

1.1 Mass Spectrometry

Mass spectrometry is the science of measuring atomic mass, first reported in the early 20th century by J.J. Thomson. Thomson was the first to report on isotopes and the electron, thus advancing our knowledge of atomic masses and generating a new field of science. Thomson's work was greatly influenced by the earlier work of Wilhelm Wien[1], who decades earlier discovered that particles within a cathode ray would deflect under the influence of an electric field with a velocity proportional to the mass of the particle. Wien proposed that the angle and velocity of deflection within the cathode ray is only reproducible by particles of identical mass, thus generating a new field of science with high mass specificity.

The field of mass spectrometry has ballooned in the last century with great advancements made in ionization methods and mass detectors, that lower the limit of detection and increase the mass sensitivity of the instruments, making mass spectrometry a vital component of analytical chemistry[2]. Mass spectrometers can now be used at atmospheric pressure and with soft ionization methods that do not destroy the sample using two methods: matrix assisted laser desorption ionization (MALDI)[3] and electrospray ionization (ESI)[4]. Both techniques are considered relatively gentle, as the species under study is not degraded during the ionization process and entrance into the instrument.

1.1.1 Electrospray Ionization (ESI)

Due to the gentler nature of ionization, electrospray ionization is often used in biological sciences as a method that can analyze proteins at physiological conditions. ESI-MS is extremely useful in

the field of catalysis, as it allows for immediate on-line analysis of a reaction as it is occurring. This could prove to be crucial for the determination of enzyme-catalyzed products[5]. Due to the formation of multiply-charged ions during ESI, this technique is especially useful in the detection of high mass analytes on instruments with limited *m/z* range[6,7]. ESI was a technique popularized by John Fenn[8] as a means of creating a link between liquid chromatography and traditional gaseous mass spectrometry analysis. In brief, a sample is vaporized at the ion source by being passed through a heated capillary with an electric potential applied, often with the addition of a volatile solvent to aid in protonation or deprotonation of the species[9,10]. A potential difference of a few kV is supplied between the capillary needle and the chamber walls of the mass spectrometer (the counter electrode)[7]. The potential applied at the capillary can be either positive or negative. In positive ion mode, the positive charge applied to the capillary causes the negatively charged ions participating in the electrochemical reaction to flow towards the capillary walls, generating a solution with primarily positively charged ions along the capillary axis and the negatively charged analytes are along the capillary walls. With this concentration of charged ions along the capillary axis, there is an accompanying decrease in pH and formation of positively charged analyte ions from a neutral analyte due to the interaction with solvent (usually H_3O^+) as the solution nears the tip of the capillary:

$$M + H^+ \rightarrow [M + zH]^{z+} \quad (1)$$

Where *M* is the analyte and *z* is the number of charges/protonation events occur during the formation of the analyte ions. The composition of the charged liquid will be altered to contain mostly positively-charged ions (in the case of a positive voltage applied to the capillary) primarily

due to the redox reactions occurring at the metal-liquid capillary interface where negative potential has built up[11,12].

There are a couple of methods to prevent the charge imbalance buildup that occurs with positively charged ions exiting from the capillary tip during electrospray[13]. If the spray capillary is metal, the metal could be ionized and causing a release of electrons to the electrode (equation 2). Another potential redox reaction would be the removal of negatively charged ions present in solution with an oxidation reaction at the metal surface (shown below for aqueous solutions, equations 3 and 4)[7,14]:

$$M_{(s)} \rightarrow {M^{2+}}_{(aq)} + 2e^- \quad (2)$$

$${4OH^-}_{(aq)} \rightarrow {O_2}_{(g)} + 2H_2O + 4e^- \quad (3)$$

$$2H_2O \rightarrow {O_2}_{(g)} + 4H^+ + 4\,e^- \quad (4)$$

The reaction displayed in equation 2 is dependent on the material of the metal electrode, with the dominant reaction between equations 3 and 4 dependent on the lowest oxidation potential[12,13]. With a voltage applied to the capillary generating an electric field, an inhomogeneous distribution of charged species will occur. Ions inside the spraying capillary are subjected to the electric field (E_c) calculated by Loeb[15]:

$$E_c = \frac{2V_c}{r_c \ln\left({4d}/{r_c}\right)} \quad (5)$$

Where V_c is the applied potential, r_c is the outer radius of the capillary and d is the capillary tip-counter electrode distance[11]. The energy required for onset of instability in the Taylor cone (E_{on}) that causes electrospray can be related to equation 5 is given below[16]:

$$E_{on} = \left(\frac{2\gamma cos\theta_0}{\varepsilon_0 r_c}\right)^{1/2} \quad (6)$$

Where γ is the surface tension of the liquid, θ_0 is the half-angle of the liquid cone at the capillary tip and r_c is the inner radius of the capillary. To determine the voltage required for electrospray to occur, equations 5 and 6 can be combined. For example, if we substitute θ_0=49.3^0 and ε_0= 8.8x10^{-12} J^{-1}c^{2}m^{-1}, we get the following simplified equation to determine the capillary voltage for the onset of electrospray:

$$V_{on} = 2x10^5(\gamma r_c)^{1/2}\ln(\frac{4d}{r_c}) \quad (7)$$

Ionization of the liquid sample for generating gas phase ions can be split up into three steps: nebulization of the liquid sample at the capillary tip, vaporization of neutral solvent molecules and ion evaporation of the remaining solvent from the charged droplet[7,9,10,17]. This positively charged solution has repulsive interaction within the capillary, and the strong electric field propels the liquid phase ion towards the liquid gas interface, generating a spray of randomly charged droplets at the capillary and forming a Taylor cone at the tip (nebulization)[9,10,18]. Charged droplets are ejected and begin to evaporate at the Rayleigh limit (where surface tension is equal to coulombic repulsion) and emit as a spray[4]. Vaporization of the neutral solvent molecules and volatile solute (such as ammonium acetate) through desolvation by a counterflowing gas causes the radius of the charged droplets to decrease, generating a higher field strength at the surface of the charged droplets[9,17]. These highly charged parent droplets travel towards the mass spectrometer, where with increasing repulsion due to increased surface charge density and decrease in droplet radius they break apart by fission into progeny droplets of various charges[4,7,11]. The ion stream then enters the ion source at atmospheric pressure, with

a gradual reduction in pressure as the ion stream travels through various quadrupoles towards the mass analyzer[19].

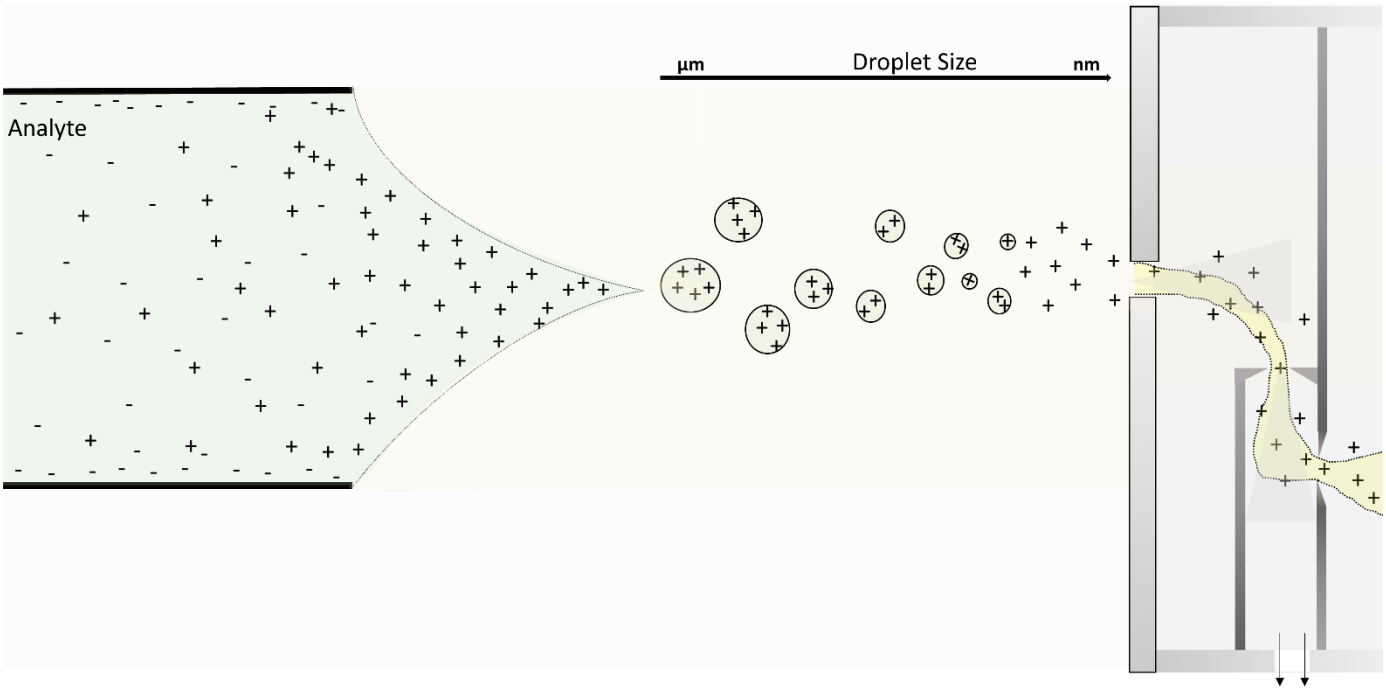

Figure 1.1 Magnification of Electrospray Ionization Droplet Formation in Positive Ion Mode. The analyte solution flows through a metal capillary with an electric potential applied. Positive ions are repulsed away from the capillary, generating a Taylor cone of positively charged species at the tip. When the columbic repulsion exceeds the surface tension of droplets formed, progeny droplets are ejected from the large droplets, generating a cycle of fission events. Having a volatile solvent along with fission events allows for efficient evaporation of solvent around the charge analyte molecules, as the spray droplet size is reduced from µm to nm before entering the mass spectrometer (grey box, right) that is the counter electrode of this electrochemical reaction. Image depicts at Waters Q-ToF mass spectrometer with a Z-spray ion source. The analyte enters into the mass spectrometer orifice where the ion beam is collimated (yellow outline) with decreasing pressure as the neutral gas molecules are pumped out of the mass spectrometer by the curtain gas.

1.1.2 Nanoelectrospray Ionization (nanoESI)

Nanospray ionization has benefitted protein mass spectrometry considerably. As shown in equation 7, the radius of the capillary used in electrospray is linearly proportional to the voltage required for spraying to occur. With a smaller radius, the voltage required for ionization is also decreased, providing gentler desolvation conditions that can allow for less volatile solvent systems[17]. In addition, a reduction in flow rate within the capillary originally reported an increase in desolvation efficiency as 510 times higher with a nanoESI source equipped, likely due to a lower potential for clustering and a reduction in curtain gas[20]. By using a nanoelectrospray source we expand the possibilities for physiological conditions at the source and an analysis of non-covalent complexes[21].

1.1.3 Mechanism of Electrospray Ionization

In contrast with the electrochemistry occurring at the capillary during electrospray ionization, the ionization of the gas phase ions is in free space and can be generated through various mechanisms. The ambient gas pressure during ionization is necessary for supressing electric gas discharge and maintaining the temperature of the droplets are they undergo continuous evaporation[12]. The manner in which the soft ionization of proteins and other analytes occurs has been subject to considerable study, with three prevailing theories as to how the desolvated analyte is produced: the charged residue mechanism (CRM), proposed by Dole[22]; the ion evaporation model (IEM), proposed by Iribarne and Thomson[23]; and the third theory of the chain ejection model (CEM), proposed by Konnermann[24]. In the CRM, a charged droplet containing one

ion within a liquid droplet is expelled through coulombic fission or goes through complete evaporation of the liquid exterior in a cycle until the ion remains with little to no solvent[12,25]. The relationship between the charge of the ion and the size of the droplet must not exceed Rayleigh's limiting charge and can be calculated using the following equation:

$$ez_R = q_R(R_i) = 8\pi(\gamma\varepsilon_0 R_i^3)^{\frac{1}{2}} \quad (7)$$

Where q_R is Rayleigh's limiting charge for a droplet, γ is the surface tension of the solvent, and R_i is the radius of the large ion. Progeny droplets undergoing evaporation and coulombic ejection from parent droplets will have charges lower than q_R (70-100%)[6,25].

In contrast to the coulombic repulsion and ejection model of CRM, IEM predicts that low molecular weight species will be ejected from the droplet due to the high electric field caused by excess charge carriers in the droplet and coulomb repulsion between cationic side chains and therefore acquire charge locally, likely with a smaller charge than would be produced by CRM[6,24]. Droplets shrink by evaporation until the field strength is large enough for ions to be ejected from the droplet. The energy associated with the large electric field is sufficient to compensate for the energy required for the solvated ion expulsion[26].

More simply, the difference between these two theories can be isolated to the method in which the analyte molecules separate from each other and the droplet: for IEM, a single analyte is present per solvent droplet and will desorb into the gas phase and reduce the coulombic repulsion of the droplet. In CRM, this analyte ejection occurs through multiple fission events until only one molecule of analyte is present in a droplet[11].

The CEM theory can be described as a combination of the original two proposals, in that the behaviour of the macromolecular analyte is dependent on it's conformation; species that are unfolded or hydrophobic will exhibit IEM-like ejection, while polymers that are folded or hydrophilic will behave like the CRM model[6]. As protein is unfolded, the polarity of the macromolecule changes from hydrophilic to exposing the primarily hydrophobic core, causing the polymer chain to migrate towards the droplet surface for ejection due to the electrostatic repulsion[24,27]. The main difference between the CEM and IEM is the way ejection from the solvent molecule occurs. For the IEM, the species will acquire charge locally as it is ejecting. In the CEM, the species will be ejected in a sequential manner, one charged residue at a time. This generates a higher charge on the species than by IEM alone[26].

Bearing these models in mind, native globular proteins are believed to follow the CRM, as charged polar residues would be facing the solvent and more susceptible to fission events[24], while smaller analytes follow the IEM, driven by hydrophobic interactions. The CEM is proposed to represent behaviour of proteins under non-native conditions, such as protein unfolding during electrospray.

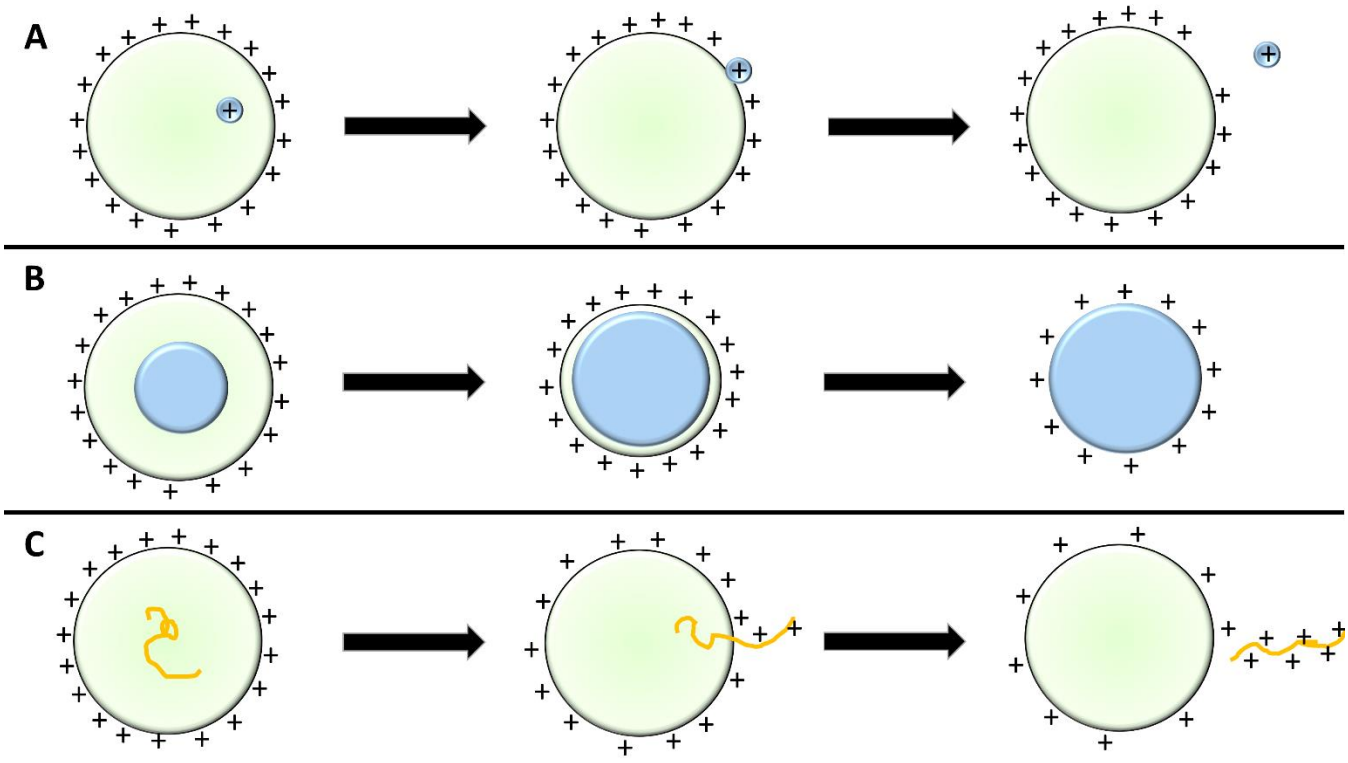

Figure 1.2 Electrospray Ionization Evaporation Models. The blue circle represents the charged ion, while the larger green circle represents the charged solvent. A) Ion Evaporation Model (IEM)[23], suggests that low molecular weight species within a droplet will eject and acquire charge locally as they exit the charged droplet. B) The Charged Residue Model (CRM)[22] proposes that the droplet will gradually lose all solvent due to evaporation and the a charged species will retain the overall charge of the droplet prior to evaporation (but not exceeding Rayleigh's limiting charge). Given the same species in solution, the IEM process would produce an ionized species of lower overall charge. C) The Chain Ejection Model, which depicts the ejection of an unfolded protein, that acquires charge locally as ejection is occurring.

1.1.4 Quadrupole Time-of-Flight (Q-ToF) Mass Spectrometers

Mass spectrometers with a time-of-flight analyzer are now routinely used for the analysis of large macromolecular structures, with increasing use in transmission of high *m/z* species[28–30].

Quadrupole Time-of-flight instruments (Q-ToFs) are able to combine high sensitivity and mass accuracy for precursor and product ions with a small limit on the size of the species, allowing low charge states of macromolecules can be examined[19]. Traditionally, there are 3 quadrupoles (Q0, Q1 and Q2) where ion separation and transmission occur, followed by the time-of-flight (ToF) mass analyzer at the back end of the instrument.

A quadrupole mass filter contains 4 parallel and electrically isolated electrodes that generate a hyperbolic electric field between them using both RF and DC-fields, causing ions to be focused down the quadrupole center. Q0 operates as the ion guide, responsible for focusing the ion beam; Q1 is the mass filter, Q2 is the collision cell (utilizing neutral gas molecules) and the ToF carries out the mass separation. In a triple quadrupole instrument, Q0 and Q2 are in RF-only mode; this helps confine the ion beam of the parent and fragment ions[31]. This confinement also reduces ion motion, slowing down the flow of ions and reducing beam amplitude into the mass analyzer, effectively increasing the quantity of ions reaching the analyzer[31]. When the quadrupoles are used as a mass analyzer, they can operate with both RF and DC-voltages applied, with the Mathieu parameters of each component (q_M is for the RF-voltage, a_M is for the DC-voltage) calculated using the following equations[31]:

$$q_M = \frac{4eV}{(\frac{m}{z})\omega^2 r_0^2} \; ; \; a_M = \frac{8eU}{(\frac{m}{z})\omega^2 r_0^2} \tag{8}$$

For the RF-voltage parameter (q_M), e is the charge of an electron, ω is the angular frequency and V is the amplitude. For the DC-voltage parameter (a_M), U is the DC-voltage, and r_0 is the radius of the quadrupole. When in RF-only mode, the quadrupoles rely only on the q_M parameter, with ions that have a q_M<0.908 being rejected during the mass filtering[31].

For tandem MS, the Q1 operates as a mass filter, allowing only the parent ion of interest to pass into Q2. Within Q2, the ions undergo collision induced dissociation (CID) after collisions with neutral gas molecules (generally argon or nitrogen). After collisions, the ions are again focused by the RF-field and re-accelerated into a parallel beam for entrance into the ToF analyzer[31]. At the entrance of the ToF, an orthogonal electric field is pulsed through the ion beam, pushing the ions into the accelerating column, where mass separation occurs[28]. Because the ions are accelerated with the same energy, ions with different *m/z* will acquire different velocities and reach the mass detector at different rates.

In order to avoid spectral overlap of the pulsed ion beams passing through the ToF analyzer, an injection pulse at the modulator cannot be applied until after the slowest ion has reached the detector at the end of the analyzer. The slowest ions will travel a distance *D* and have an ion beam length Δ*l* that can be detected, generating an upper limit to the duty cycle of this particular *m/z* value that can be calculated using the following:

$$duty\ cycle\ \left(\frac{m}{z}\right) = \frac{\Delta l}{D}\sqrt{\frac{m/z}{m/z_{max}}} \tag{9}$$

Where m/z_{max} is generated from the flight time that is the inverse of ToF pulse frequency[31]. Most ToF instruments operate with a duty cycle of 5-30%[8]. The resolution of in a ToF mass spectrometer is calculated as:

$$R_{FWHM} = \frac{m}{\Delta m} = \frac{t}{2\Delta t} = \frac{L_{eff}}{2\Delta z} \tag{10}$$

Where Δ*m* and Δ*t* are the peak widths measured at half mass and time (respectively), *m* and *t* are the mass and flight times of the ion, Δ*z* is the thickness of the ion packet and L_{eff} is the effective

length of the ToF analyzer. The relationship between the flight time of the ion and the mass of the ion is:

$$t = \frac{L_{eff}}{\sqrt{2eU_{acc}}} \sqrt{m/z} \quad (11)$$

Where U_{acc} is the accelerating voltage in the ToF[31]. Although the mass range that a ToF can analyze is unlimited in theory, there are practical limitations that arise based on the availability of the ion transmission through the quadrupoles, dependent on the RF amplitude[28]. The highest *m/z* value achievable at the quadrupole of each instrument (M_{max}) can be calculated using the following equation:

$$M_{max} = \frac{7*10^6 V_m \cos(2\pi ft)}{f^2 r_0^2} \quad (12)$$

Where $V_m\cos(2\pi ft)$ is the applied RF voltage (the oscillation rate of the alternating current) applied between rods, f is the frequency (Hz), t is the time of transmission (s) and r_o is the inner radius of the quadrupoles (m)[28]. The safest way to increase mass range in a ToF instrument is by increasing the frequency, to the detriment of instrument resolution (shown in equations 10 and 11). For high resolution, a narrow transmission window is required, lowering the amount of duty cycles that are carried out by the mass spectrometer.

Mass spectra for ESI-MS are recorded using a time-to-digital converter (TDC) at the end of the ToF channel, with a multiple anode detector as an add on for increasing the dynamic range of this ion-counting technique. The TDC records the arrival time of the electric pulse in conjunction with the start time of the same pulse, generating a spectrum of arrival times summed over the course of the acquisition time.

Microchannel plates (MCPs) are another form of detector, that have a flat conversion surface area, beneficial for recording large amounts of ion packets (in the y-dimension) in a transient manner. They are an analog system that digitizes the ion current. One significant problem with using a MCP as a detector is the time window in which ions hit the detector, as differing degrees of penetration will produce a large variation in detection time[31]. They also do not have a large dynamic range, and as such are generally used for MALDI systems.

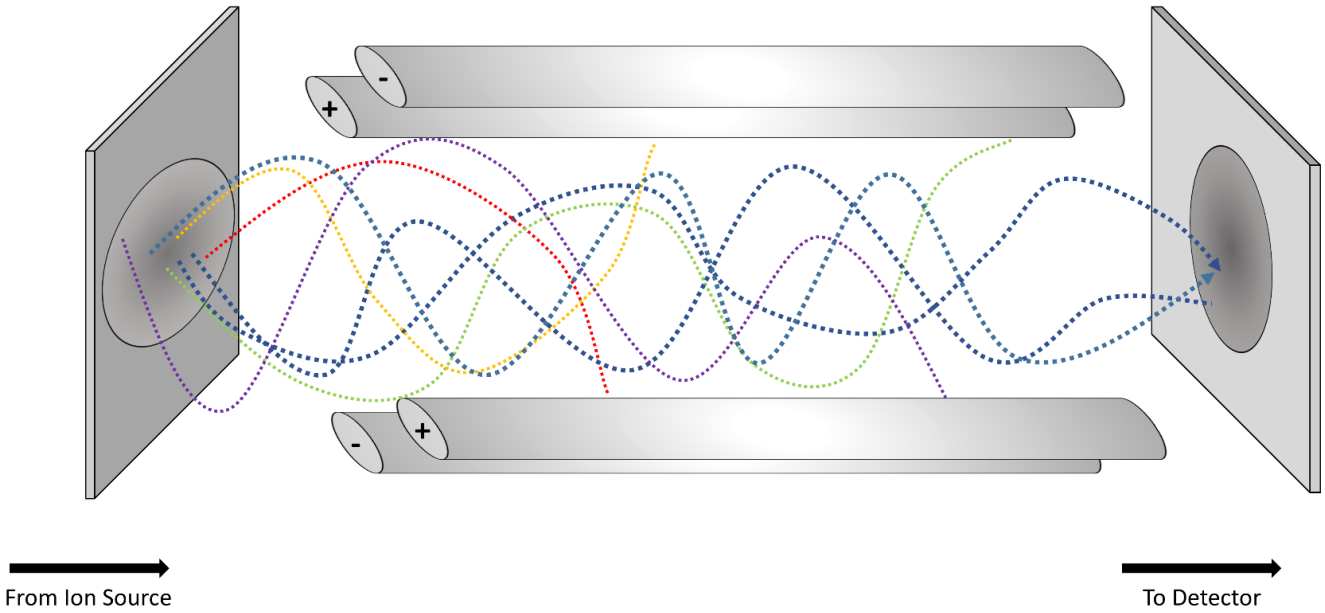

Figure 1.3 Quadrupole Ion Separation. Ions of various masses (depicted by multiple coloured lines) enter through the ion guide (left) in parallel into the quadrupole, which can act as a transmission guide (for single MS) or as a mass filter of parent ions (for tandem MS). The quadrupoles are electrodes, with opposing charged rods connected with the same DC voltage and RF-field. The applied RF-field generates a potential well that is essential for radially confining the ions, providing collisional buffering of ion movement[31]. Non-resonant ions to the RF-field will collapse into the quadrupoles, not passing through to the detector (unlike the resonant ions, in blue) of the mass spectrometer.

1.2. Ion-Mobility Mass Spectrometry- Introduction

Protein unfolding can be captured using ion-mobility mass spectrometry (IM-MS)[32–34], which measures the collisional cross-section (CCS) and drift time of ions passing through the IMS cell of a mass spectrometer. Travelling-wave IMS is predated by the drift tube IMS (DT-IMS)[33], a method of separating ions within the collision cell using a high pressure gas environment and a low-potential electric field to cause ion separation by size. As ions are passing through the weak electric field applied to the drift tube, collisions with inert gas molecules will slow down the progress of larger ions, generating a separation of ions that is dependent on the ion's size and shape[35]. This method has the limitation of having high error associated with comparing to literature[36]. In a drift tube, along with the RF-ion confinement there is also a linear voltage gradient, responsible for moving the ions along the cell towards the mass analyzer[36]. Ions move through the drift tube with ion velocity proportional to the electric field:

$$v = KE \tag{13}$$

Where *v* is the ion velocity, *K* is the ion mobility and *E* is the electric field. This ion velocity is used to calculate the drift time, related to the length of the drift tube by the following equations:

$$t_D = \frac{length}{KE} + t_0 \tag{14}$$

Where t_D is the drift time and t_0 is the transport time of ions from the end of the drift region to the ToF-mass analyzer. Drift time IMS has very low sensitivity due to the pulsing analysis and ensuing reduction in duty cycle due to the time lost between measurement of ion packets[32].

Within the drift cell, the length of the cell and potential applied can be varied in order to change the average amount of collisions with the drift gas. The time for the ionized species to pass

through the mobility cell is correlated to the CCS, with species with a smaller CCS travelling faster through the countercurrent drift gas because of reduced drag[32]. The reduced mobility coefficient (K_0) can be calculated from the following[37]:

$$K_0 = \frac{L}{t_D E} * \frac{P}{760} * \frac{273.15}{T} \quad (15)$$

Where L is the length of the drift tube (m), P is the pressure (Torr), t_D is the average drift time (s), T is the temperature (K) and E is the electric field strength (V/m). Equation 15 does not consider the charge state of the species within the mobility cell, which would also influence the drift time of the charged ion species. The equation for CCS takes the charge state into consideration.

$$\Omega = \frac{(18\pi)^{\frac{1}{2}}}{16} * \frac{ze}{(k_B T)^{\frac{1}{2}}} * \left[\frac{1}{m_I} + \frac{1}{m_B}\right] * \frac{N}{K_0} \quad (16)$$

Where z is the charge state, *e* is the elementary charge (C), *T* is the temperature (K), k_B is the Boltzmann constant, m_I and m_B are the masses of ion and buffer gases (respectively, in kg), and N is the neutral gas number density (m^{-3}). With K_0 defined in equation 15, and the parameters of E, L, P and t_D being easily measurable during experimentation, CCS calculations have great precision[37,38]. Using the above calculations, IMS-MS can distinguish species entering the mobility cell by size, shape and stability[39,40]. IM-MS is useful for examining large protein complexes as the topography of an ionized complex is sensitive and unique to each sample[38,41]. Careful consideration must be made to optimize the ionization conditions within the mobility cell to encourage ion separation but discourage non-covalent complex dissociation, such as reducing collisional heating or gas pressure within the collision cell to avoid complex dissociation[42–44].

1.2.1. Collision Induced Unfolding Mass Spectrometry

Collision-induced unfolding (CIU) is a relatively new technique used in analytical and medicinal chemistry to provide evidence of comparative binding affinity between protein substrates and study unfolding pathways[45–48]. The charged ion species is bombarded with neutral gas at increasing voltages within the collision cell of the IMS section of the mass spectrometer to encourage intermolecular collisions, eventually leading to complete dissociation of the complex. When looking at the same charge state across a panel of protein-ligand complexes, unfolding transition states can be visualized using heat maps (see figure 1.4 below), which are used to infer comparative binding affinity[49].

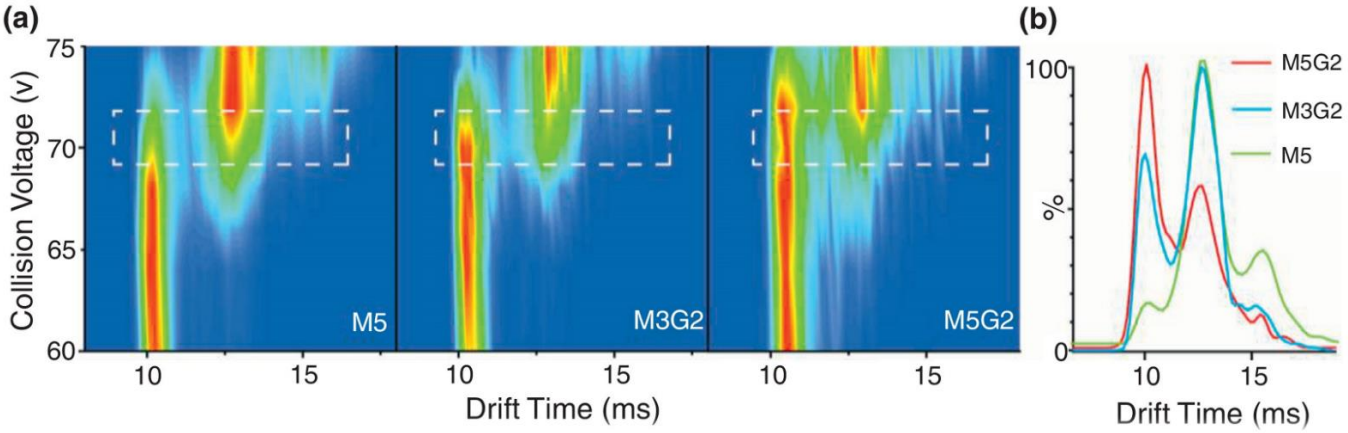

Figure 1.4 A schematic of IM-MS is used to differentiate ligand binding to large protein complexes on a Synapt G2. A) Panels of collision voltage (V) vs drift time (ms) of the Concanavlin A tetramer with 3 different manosyl sugars: 3α,6α -mannopentaose (M5), 3α,6α-mannotriose-di-(N-acetyl-D-glucosamine) (M3G2) and 3α,6α mannopentaose-di-(N-acetyl-D-glucosamine) (M5G2). Highlight white box is examined on the right. B) Drift times for each complex demonstrate the relative stability of each protein-ligand complex. Adapted from Niu et al[49].

1.2.2. Traveling-Wave Ion Mobility Spectrometry

On the Waters Synapt G2 instrument, the IMS cell is equipped with travelling-wave (TW-IMS) component that significantly increases sensitivity, compared to the traditional drift tube IMS (DT-IMS) workflow[33]. The CCS values for TW-IMS are not specifically determined from measured drift times as they are in DT-IMS. Instead, they are determined through calibrating ions of interest to ions of known CCS values[36]. This travelling-wave refers to an electric pulse applied to the ion guide, causing ion propulsion through the ion guide at a specific radio frequency. This DC travelling wave is overlaid over the RF voltage that is already applied to the stack of ion guides, causing the ions to be propelled, reducing transit time through the cell[32].

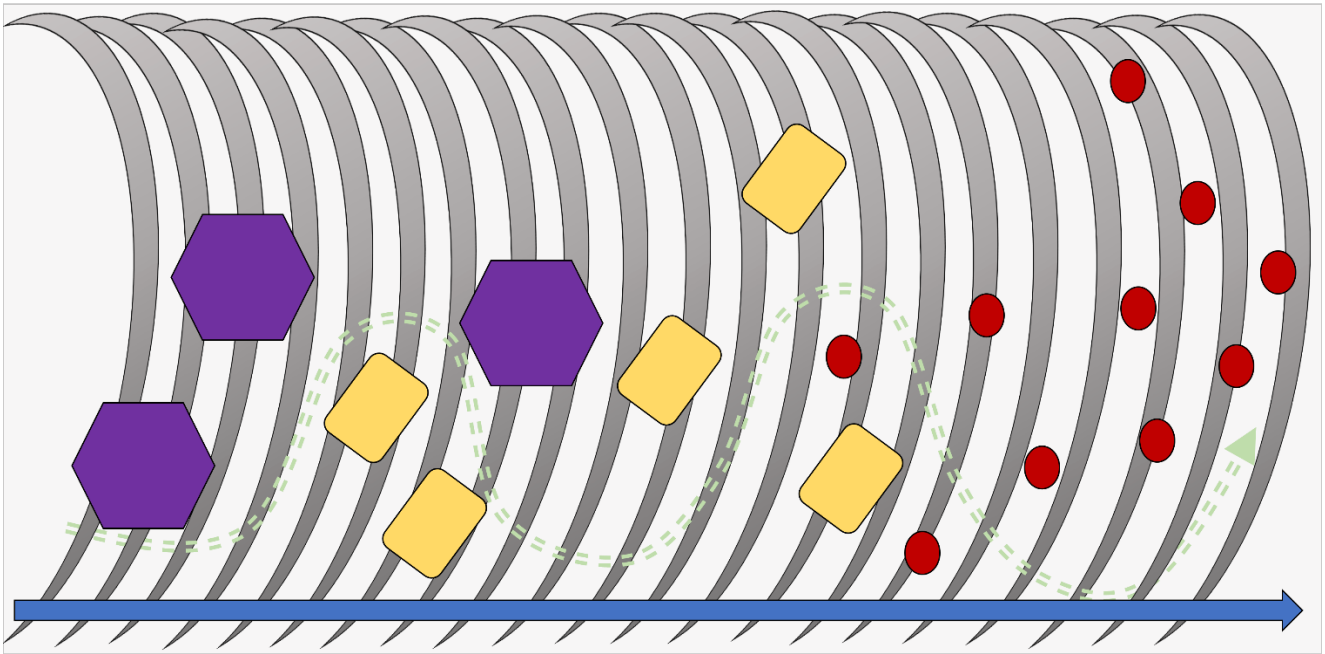

Figure 1.5 Cross Section of a Travelling-Wave IMS Collision Cell with various CCS[50]. Ring electrodes (in grey) line the collision cell, with a direct current being applied over the typical RF-voltage. This alternation of current generates a "wave" voltage that moves ions through the cell, depicted above as a dotted green line. Depending on the size of the ions, they may remain in the collision cell after the voltage pulse passes through (high mobility ions, purple and yellow shapes), or be pushed out of the cell, travelling with the wave (low mobility ions, red spheres). More compact and aerodynamic ions will travel through the collision cell faster, generating lower arrival times than bulkier ions or complexes. Further separation and resolution can be obtained by increasing the length of the collision cell.

1.3. Hydrogen Deuterium Exchange

Hydrogen Deuterium eXchange (HDX) is an analytical probing technique that provides a relationship between protein function and dynamics by measuring backbone amide deuterium uptake with a variety of experiments[51]. HDX-MS supplements traditional HDX-NMR labelling by

being able to label transient intermediates[52] and is incredibly useful for studying the conformational dynamics of intrinsically disordered proteins[53], antibody/antigen binding[54] and mapping catalytic processes to binding modes[55].HDX-MS is particularly useful due to the low quantity of protein required and ability to separate heterogeneous mixtures with chromatographic systems[51]. HDX-MS can also be used to study unfolding rates and kinetics, such as myoglobin[56]. For example, Chait and Katta used the HDX technique as a means of probing global conformational dynamics of proteins by mass spectrometry as an alternate to the more popular solution-phase NMR or circular dichroism, to identify protein intermediates[57,58]. By incubating bovine ubiquitin in deuterium, followed by acidification with deuterated acetic acid, they were able to demonstrate an increase in charge state with unfolding after a range of incubation times followed by an analysis of the various protein states elucidated. Currently, HDX-MS of proteins is most often carried out through a "bottom-up" proteomics workflow, popularized by Smith[59], that entail the following steps: incubation of protein in deuterium, followed by an acidic quenching step and proteolytic digestion before entering the ion source of a mass spectrometer. Through bottom-up HDX analysis, amino acid-level resolution can now give global structural information into protein dynamics[60].

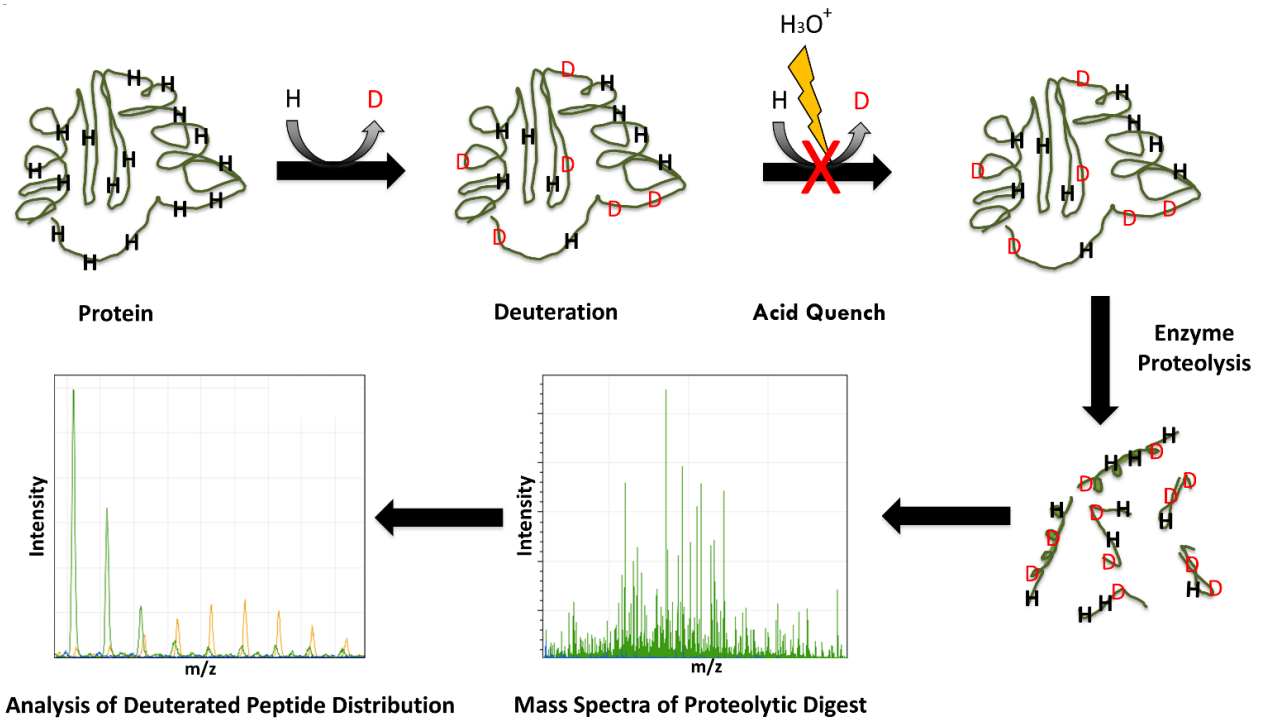

Figure 1.6 Schematic of a bottom-up proteomics HDX workflow. Protein is displayed with labile hydrogens in black. After deuteration, some labile hydrogens have been replaced with deuterium, depending on the time of incubation and dynamic nature of the protein. Following an acidic quenching step to drastically reduce the rate of back exchange, the deuterated protein is digested by proteolytic enzymes, such as pepsin or protease XVIII. Following digestion, the peptide mass shifts with and without deuteration are recorded. The relative isotopic distributions of peptides with deuteration (bottom left, in yellow) compared to without (bottom left, green) demonstrate the amount of deuterium uptake (recorded as a mass increase or as a percentage of the overall number of exchangeable hydrogens) on average for that peptide.

1.3.1. Fundamental Theory

Hydrogen/Deuterium exchange was first theorized by Linderstrom-Lang, who examined the deuteration rate of insulin and proposed the theory of protein dynamics and hydrogen exchange that we use to this day[61,62]. In solution there is a constant hydrogen exchange with solvent as

protein fluctuates between various conformational states, limited only by the pKa of each functional group associated with each amino acid. Main chain amides exchange more slowly than other hydrogen groups in the primary structure, and their exchange rate can be easily manipulated through temperature and pH variation to be measurable on a ms-s timescale[63–65]. HDX can be carried out in acidic or basic environments. The acid-catalyzed exchange being facilitated through an amidate mechanism[66,67] while the base-catalyzed mechanism operates through N-protonation or O-protonation.

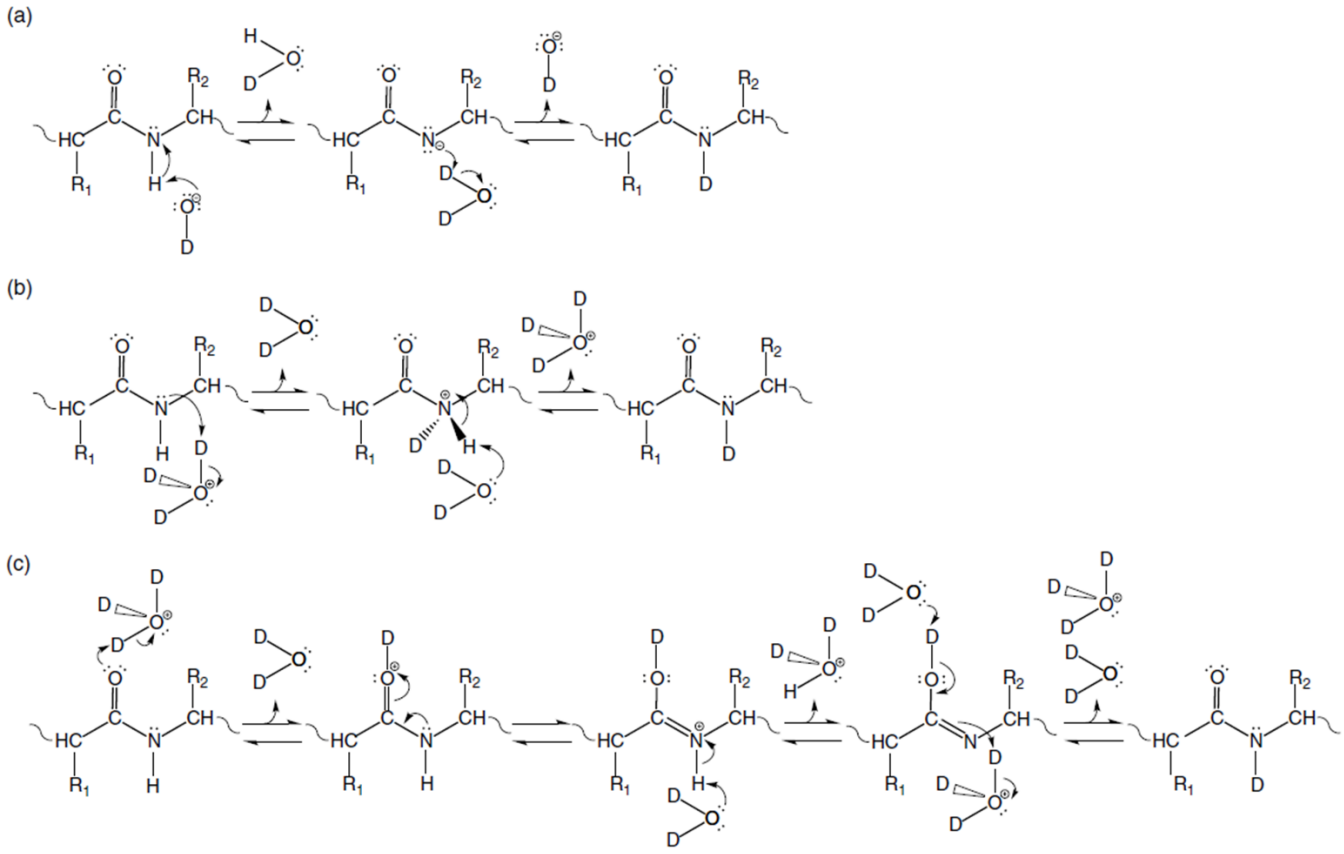

Figure 1.7 Schematic of acid (B and C) and base (A)-catalyzed hydrogen/deuterium exchange reactions mechanisms with backbone amides. A) Base-catalyzed exchange, where OD^- deprotonates the amide group, generating an amidate ion which is then protonated by D_2O. B) Acid-catalyzed exchange, where the N-atom of the amide is responsible for deprotonating D_3O^+, followed by deprotonation of the amide to remove the proton. C) Acid-catalyzed exchange, with the amide O-atom initiating protonation with D_3O^+, followed by acidification of the NH proton and formation of an imidic acid. Adapted from Weis[68].

Although the N-protonation mechanism is favoured, the O-protonation pathway is more basic. With either type of catalyzed exchange reaction, the rate of back exchange with the solvent is limited by a decrease in temperature and pH, with 0^0 C and a pH of 2.5 providing the slowest rate of back exchange[69–71].

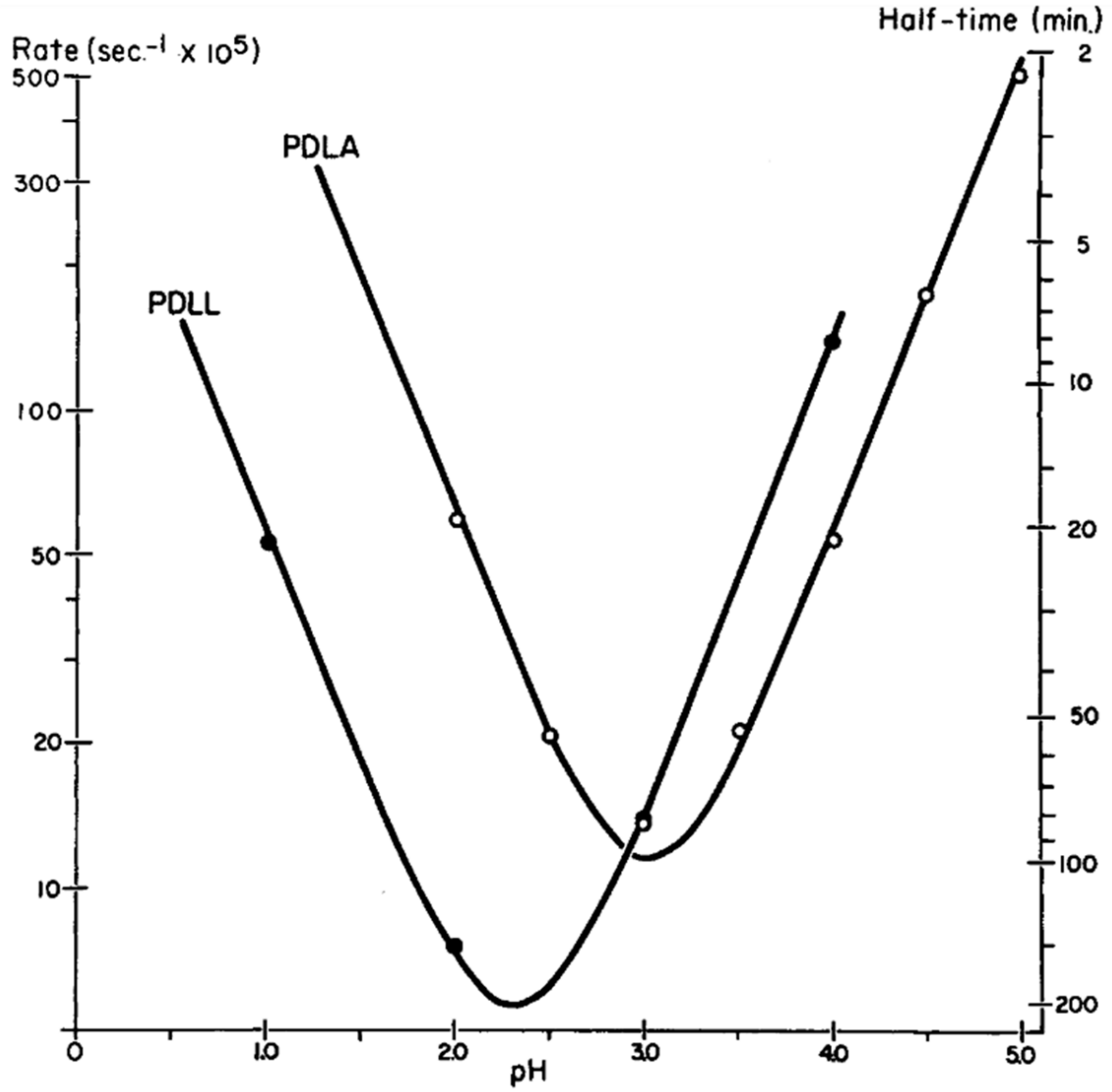

Figure 1.8 A chevron plot of logk_{ex} vs pH for two peptides, poly-D, L-alanine (PDLA) and poly-D, L-lysine (PDLL) protium/tritium exchange reactions. The original experiment that demonstrated the effect of pH on amide hydrogen exchange rates, showing a minimum rate of exchange in the pH range of 2.0-3.0 for both PDLL and PDLA species. Heavy isotope exchange was measured after incubation in tritium and column separation to remove excess tritium at fixed time points. Concentration of tritiated polymer was measured spectroscopically. Adapted from Englander and Poulsen[69].

As shown in the original work of Englander and Poulsen, in the pH range of 2.5-3.0, acid and base-catalyzed exchange mechanisms have approximately the same rate (see figure 1.8) for proteins (and peptides)[68,69]. Below pH 2.0, exchange reactions are primarily acid-catalyzed, while above pH 3.0, base-catalyzed exchange is most common. Therefore at physiological conditions (pH 7) the base-catalyzed mechanism is favoured[68]. By reducing the pH of the solution after the deuteration event, the rate of exchange will decrease by up to 4 orders of magnitude, making an acidic quenching step ideal for efficient and accurate HDX analysis[68,69]. In general, protein dynamics are thought to fluctuate between several conformations, with the most simplistic model of deuteration events depicting a rate of "open" and "closed" conformations, referring specifically solvent accessibility for deuteration events to occur with main chain amide groups.

$$NH_{cl} \underset{k_{cl}}{\overset{k_{op}}{\rightleftharpoons}} NH_{op} \xrightarrow{k_{ch}} ND \tag{17}$$

Where k_{op} is the rate of protein unfolding/opening, k_{cl} is the rate of folding/closing and k_{ch} is the chemical exchange rate (dependent on experimental conditions)[64]. Under steady state conditions, the rate can be calculated with the following equation[63]:

$$k_{ex} = \frac{k_{op}k_{ch}}{k_{op}+k_{cl}+k_{ch}} \tag{18}$$

Assuming a stable structure ($k_{cl} >> k_{op}$), equation 18 reduces to:

$$k_{ex} = \frac{k_{op}k_{ch}}{k_{cl}+k_{ch}} \tag{19}$$

There are two other conditions for protein dynamics to take into consideration. For a bimolecular exchange, EX2, it is assumed that the rate of protein refolding is much faster than the exchange can occur ($k_{cl} >> k_{ch}$).

$$k_{ex} = \frac{k_{op}k_{ch}}{k_{cl}} \tag{20}$$

Under the above scheme, it is assumed that isotopic exchange with backbone amide would be a rare event, likely occurring after multiple cycles of fluctuations between open and closed formations[72]. For a monomolecular reaction, EX1, conditions that promote exchange ($k_{ch} >> k_{cl}$, high pH, high temperature) simplify the steady state exchange equation even further:

$$k_{ex} = k_{op} \tag{21}$$

Although both conditions are possible, the EX2 scheme is more common amongst stable proteins[72] while EX1 is more common with denaturation conditions[73].

1.3.2. Pulsed vs. Continuous Labelling Conditions for HDX

The field of proteomics in mass spectrometry has expanded rapidly in the new millennium, with the study of proteins ranging from discovery, to function determination, to molecular medicine[74]. HDX experiments are traditionally carried out with a continuous labelling method, first employed in the study of protein unfolding kinetics by measuring changes in charge state through acid denaturation[75]. In brief, protein is exposed to deuterium and the rate of deuteration is measured over time as an increase in protein mass[72]. This increase in mass over time is an averaging of all

the protein dynamics in solution at a specific time, and as such does not identify where deuteration is occurring in the global structure[68].

Pulse labelling experiments are typically carried out with quenching steps (by acid or a different solvent) and have a known observation time to determine transient intermediate species, with minimum reaction times of a few seconds being achievable[52,76–78]. The time points selected for quenching are longer than the exchange time, allowing for the deuteration to be monitored at various parts of the reaction[68]. The reaction is carried out inside an observation cell, where data acquisition begins once the liquid flow is detected and the protein species is no longer at equilibrium[76]. Limitations of this pulsing workflow initially included the inability to observe reaction occurring without absorption or fluorescence spectroscopy, which would reduce the number of species that could be studied.

1.3.3. Time-Resolved Hydrogen Deuterium Exchange

Millisecond-second scale HDX was a fortunate byproduct of using a microfluidics workflow to interface ESI-MS with an on-line analytical technique. Work by Kern et al with NMR relaxation techniques has demonstrated that the dynamics observed on the ps-ns timescale of amide bond fluctuation have direct influence on the µs-ms timescale global fluctuations[79]. Time-resolved ESI enables an accurate examination of protein dynamics in solution or gas phase[56,80]; the ms-s timescale is especially useful for monitoring transient intermediate species in pre-steady state conditions[81], ligand binding[82,83], protein unfolding and catalysis[75,84]. As data is acquired using this kinetic workflow, it is possible to calculate rate constants, turnover number and the dissociation constant for a variety of proteins to uncover reaction mechanisms[5,85]. Coupled with

a proteolytic digestion step, many groups have reported complete protein digestion with a variety of samples within a few seconds of incubation[86].

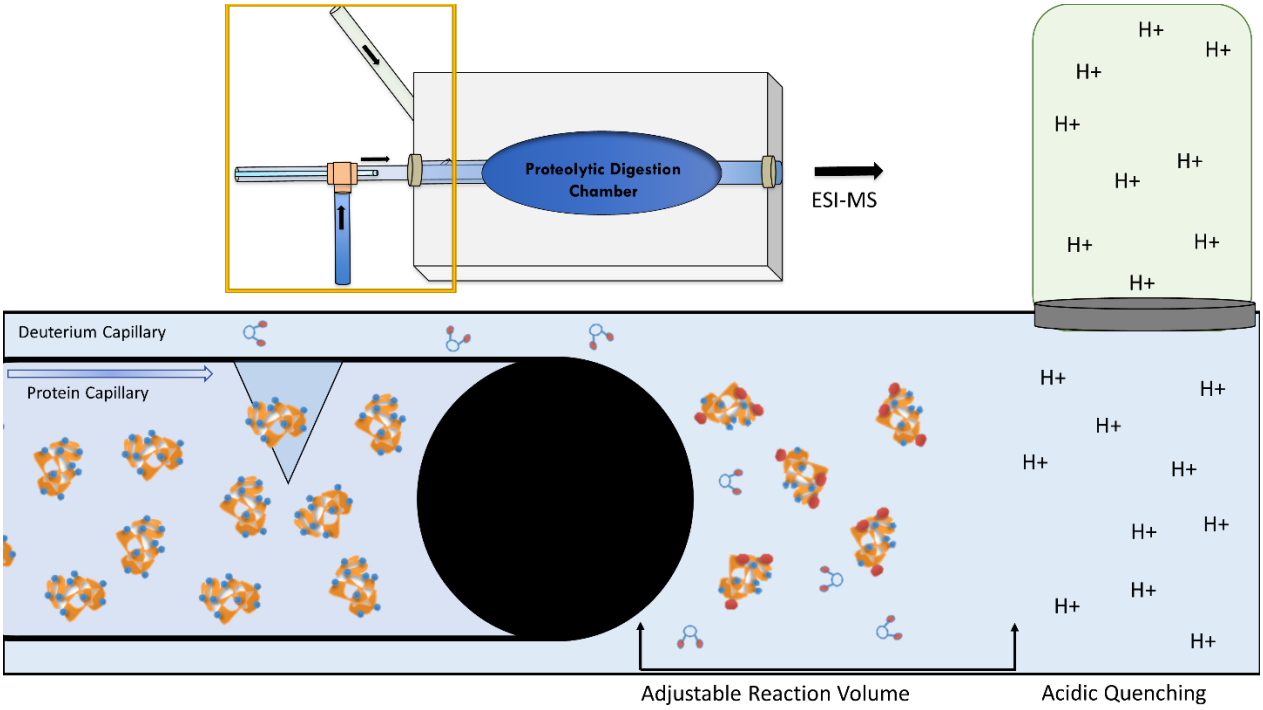

Figure 1.9 Schematic of the Wilson Group Time-Resolved HDX Capillary Workflow Top) Overview of the microfluidics workflow and PMMA chip used for bottom-up HDX analysis. The yellow box highlights the magnification shown below. Bottom) An inner glass capillary containing the protein sample has a soldered end with a small notch engraved 2 mm away from the edge. For continuous labelling HDX, the microfluidics device must have efficient mixing to ensure non-laminar flow within the microcapillaries. With this notch, the protein sample is able to flow out of the inner capillary into the larger metal capillary, which contains deuterium and mix efficiently. With known flow rates, capillary dimensions and fixed reaction volume before quenching, the time of deuteration can be easily calculated. After deuteration, the reaction is quenched at a T-mixer by an acidic solution (right). For experiments involving substrate/ligand binding, traditionally the substrate is introduced concurrently with the deuteration event to map conformational dynamics specifically to protein: substrate interactions.

1.3.4. Microfluidic Devices for Hydrogen Deuterium Exchange

A reduction in size of any analytical system involving fluid dynamics will have a dramatic increase in sensitivity, transportation time to the detector and better resolution[87,88]. It is with these principles in mind that microfluidics devices have been devised for use with an electrospray source on a mass spectrometer. ESI-MS carried out on a microfluidics device requires a nL-µL/min flow rate, which is ideal for using a nanoelectrospray source. Microfluidics devices could have an ESI interface either constructed into the device or protruding outwards, like a metal capillary[89], or they may have a nanocapillary interface for efficient chromatography simultaneously through electrophoresis[90–92]. In the past decade, advances have been made to embed proteolytic digest within polymeric cells[93], reduce the dead volume during analytical separation[92,94] and enable a nanoLC-chip-MS workflow[94]. Additionally within the past year, the Rand group have commercialized a microfluidics device for rapid HDX incubation times with quenching and deuteration channels built on-line[95].

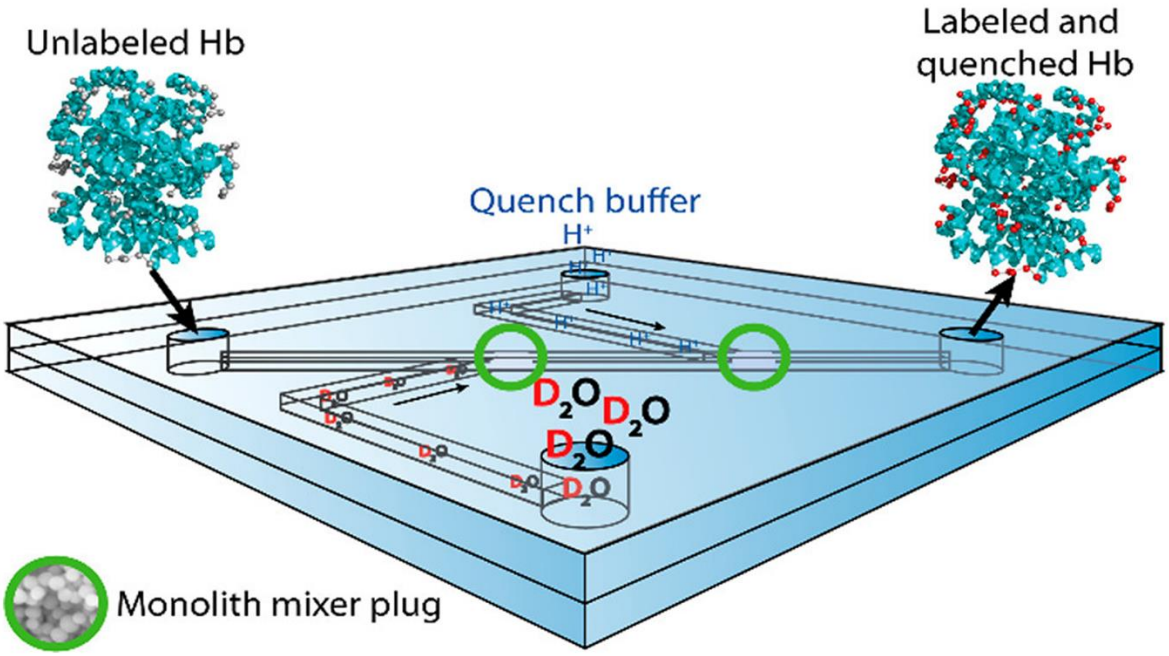

Figure 1.10 Schematic of a new generation microfluidics chip. In this recent advancement to the field of microfluidics and sub-second HDX, on-chip deuteration and quenching allows for rapid mixing. In addition, thiolene plugs reduce dead volume within the microfluidics channels, further reducing the timescale limit for rapid HDX. Adapted from Svejdal et al[95].

1.4. Enzymes Producing Antimicrobial Resistance- An Overview

1.4.1. Antibiotic Drug Development

Antibiotics have been used commonly since the discovery of penicillin in the 1929 and have ballooned in the pharmaceutical industry[96]. Antibiotic resistance primarily due to overuse in the general population has plagued our advancement in the drug development process due to the high mutational rate and adaptability of bacteria along with the emergence of multidrug resistant pathogens[97–100]. Current medical practices typically combine doses of an inhibitory drug in conjunction with an older family of penicillins or cephalosporins to provide effective medical

treatment[101,102]. Resistance is now common among the newest Class 3 antibiotics, signaling the end of the ability to effectively eliminate bacteria with current medical practices[98,103,104].

1.4.2. Role of Penicillin Binding Proteins in Bacterial Cells

The cell wall in prokaryotes is responsible for maintaining the internal osmotic pressure necessary for bacterial life and to facilitate cellular growth[105–107]. Penicillin binding proteins (PBPs) are transpeptidases responsible for cross-linking peptidoglycan strands in the bacterial cell wall. The glycan chains targeted by PBPs are alternating β-1,4-glycosidic linkages between N-acetylglucosamine (NAG) and N-acetylmuranic acid (NAM). In the final step of cell wall synthesis, the D-ala terminal reside of the NAM sugar is removed[108]. The acyl-NAM chain then forms amide linkage with the terminal L-alanine residue of the peptide L-alanyl-γ-D-glutamyl-L-diaminoacyl-D-alanine, generating a peptidoglycan strand[107,109]. PBPs were first implicated in resistance mechanisms in the early 1970s[106], and this theory gained traction with the isolation of an evolved PBP (PBP-2a) that had low affinity for penicillins[110,111].

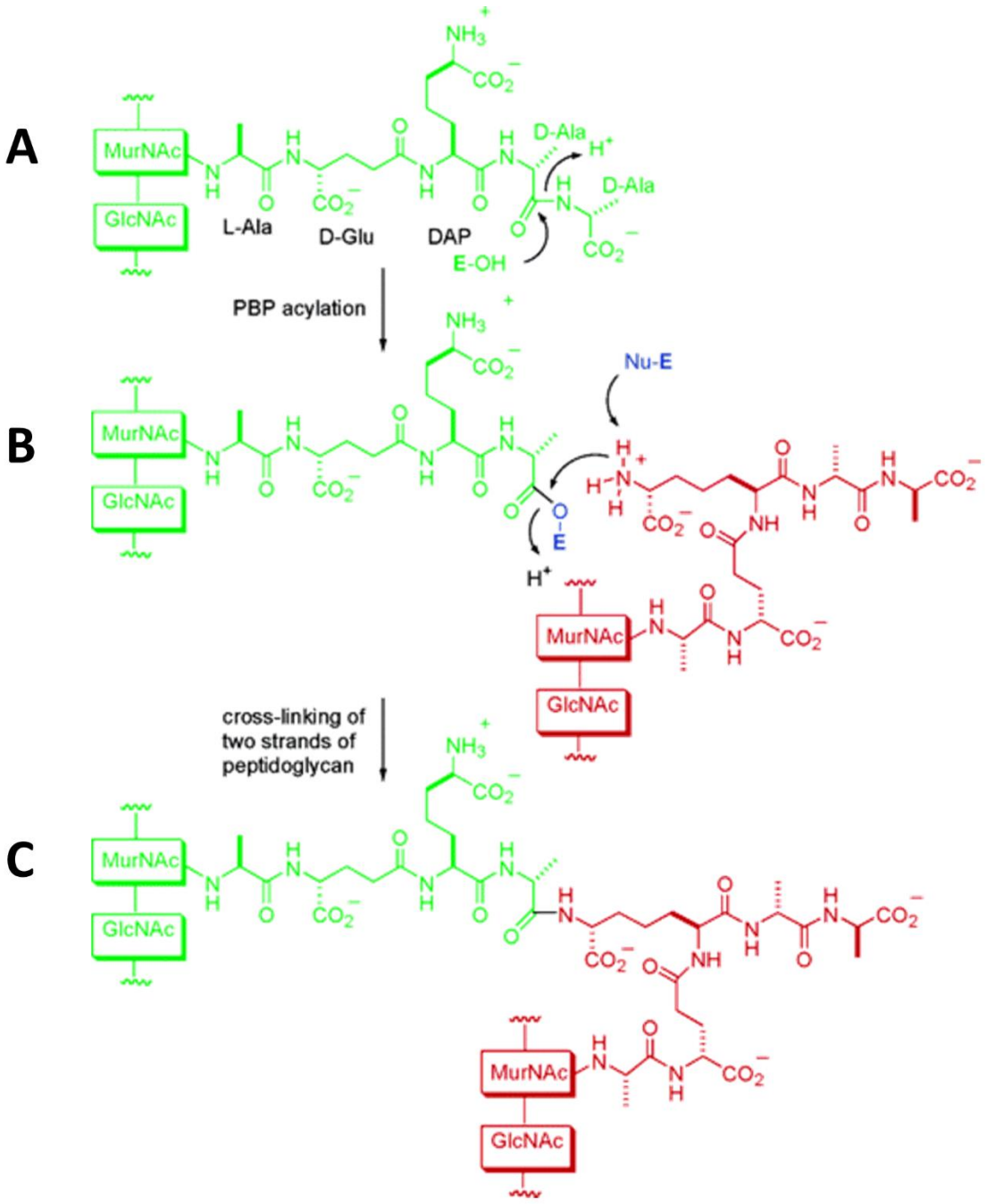

Figure 1.11 Mechanism of Peptidoglycan Formation by Penicillin Binding Proteins in the Cell. A) Acylation of the terminal D-alanine residue of the NAM sugar. B) Nucleophilic attack (likely by a conserved Lysine residue) generated a protonation event between the glycans. C) The β-1,4-glycosidic linkage is formed, generating a peptidoglycan strand. Adapted from Fisher et al[108].

1.4.3. Generation of β-lactam Antibiotics

β-lactam antibiotics target the cell wall synthesis of gram-negative bacteria by inhibiting PBPs at the Ser403 residue; the structure of the most common antibiotics contains a β-lactam core that mimics the D-Ala-D-Ala terminus of peptidoglycan chains [103,108,112,113], resulting in a cell that goes through structural degradation of the cell wall without the PBPs generating new peptidoglycan. β-lactam antibiotics are the main form of medication in mass production to treat bacterial infections for several reasons: they can be produced in high yield, are stable with several variations in functional groups and can be derived at low cost[108,114,115]. This structural uniformity across a medical class has made mutational adaptability to β-lactam drugs straightforward. Complete resistance to β-lactam antibiotics and inhibitors has been observed in an increasing number of organisms, suggesting that without new approaches, the effectiveness of β-lactam drugs may be limited in the long-term[116–119]. The newest antibiotic, Avibactam[120], is a diazabicyclooctane inhibitor that has been produced without a β-lactam core. However, its effectiveness is still not enough to be ingested alone; it must still be introduced in conjunction with an additional β-lactam antibiotic for full treatment.

1.4.3.1. Differences in Antibiotic Families

Several families of antibiotics have been studied in experiments with TEM-1 to determine their efficacy (measured as a kinetic value of the deacylation reaction), but no experiments have yet been able to distinguish the specific amino acid residues involved in the digestion of these substrates. To overcome β-lactamase mediated antibiotic resistance, a number of β-lactam drugs, notably the cephalosporins, have been developed that generate inefficiently hydrolyzed

acyl-enzyme intermediates and have increased binding affinity within the active site[121–124]. Also in clinical use are β-lactamase inhibitors that are not antibiotics in themselves (because they do not efficiently bind PBPs) but can irreversibly acylate β-lactamases though a series of off-pathway intermediates. The current practice with 'challenging' pathogens is often to prescribe a β-lactamase inhibitor in conjunction with older-generation β-lactam antibiotics, but this approach is becoming less and less efficient[101,125,126]. Ampicillin, cephalexin and potassium clavulanate were tested as substrates for mapping conformational dynamics with TEM-1. The penicillin family of drugs (which includes ampicillin) has been extensively studied kinetically and have comparative data to cephalosporins, but there has been no reporting on global changes in TEM-1 conformational dynamics with these drug substrates. Potassium clavulanate, an irreversible covalent inhibitor, was used as a negative control to determine the most inactive/closed confirmation possible for TEM-1 as it binds in the active site.

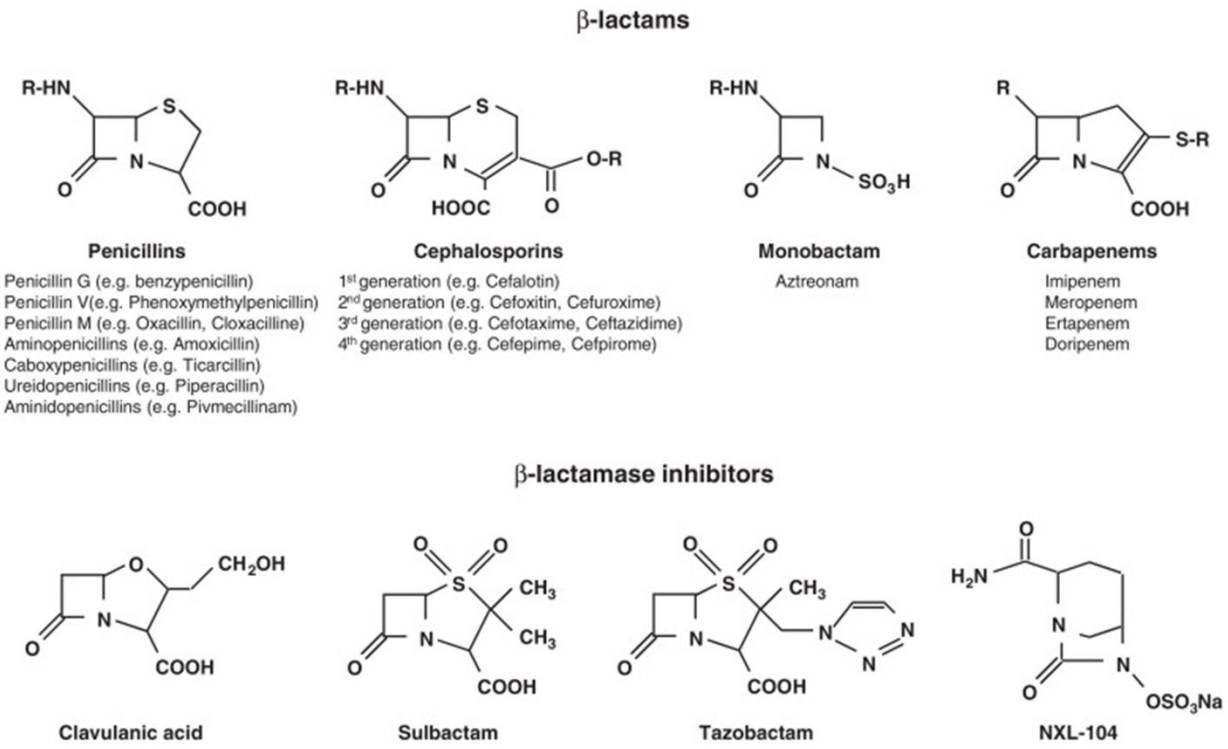

Figure 1.12 Chemical structures of β-lactam antibiotics currently on the market. β-lactam drugs can be split up into 4 families: penicillins, cephalosporins, monobactams and carbapenems. Inhibitors also contain the β-lactam core but possess weaker antimicrobial activity. Adapted from Nordmann et al[103].

1.4.4. Evolution of β-lactamases

In an evolutionary response to the appearance of β-lactam drugs in the bacterial cellular environment, bacteria have evolved proteins known as β-lactamases, that hydrolyze β-lactams before they can inhibit PBPs[127–130]. Most classes (A, C and D) of β-lactamases contain an active site serine that is responsible for the hydrolysis of the lactam ring contained within the β-lactam antibiotics[120,131,132]. This SXXK motif (residues 70-73) is conserved in all Class A β-lactamases and

is the primary site of interest in drug development[133]. Class B β-lactamases are metallo-enzymes that coordinate with Zinc ions to effectively hydrolyze the drug substrate[125,134,135].

1.4.4.1. TEM-1 β-lactamase Introduction

Our research is focused on TEM-1, a Class A β-lactamase, the most common form found in *E. coli*[136]. Hundreds of variants have been discovered and present in resistant forms to all drugs of the penicillin family and several of the cephalosporins[130,137]. Due to it's singular binding site and the residues involved in the acylation at the active site there has been rigorous study into the residues crucial to impart drug resistance[138–141]. The reigning consensus is that the omega loop (residues 161-179), a structurally conserved SXXK motif (residues 70-73), a general base (Glu166) and a series of nucleophiles (Ser70 and Ser130) are the principal regions involved drug binding and acylation[100,142–147], along with salt bridges to regions outside the active site[148]. Early research on TEM-1 successfully crystallized the acyl-enzyme intermediate[149] and inhibitor-bound[150] states which are used throughout as a reference for enzymatic activity. Unfortunately, there is still no crystallographic structure of the pre-acylation substrate-bound complex, due to the rapid kinetics[151]. The search for allosteric regions in TEM-1 have yielded some results[42–44], but has yet to lead to new drug design.

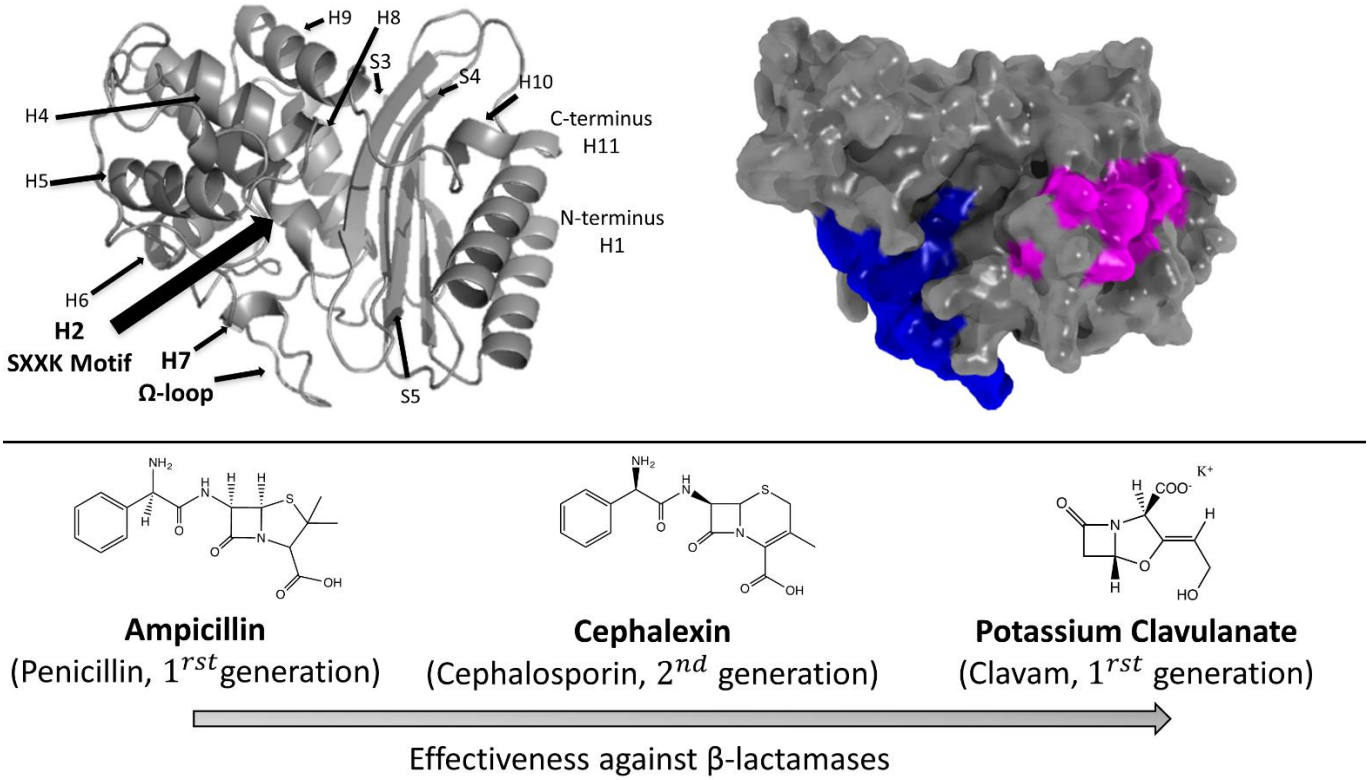

Figure 1.13 TEM-1 crystal structure with 3 drug families used in TRESI -HDX experiments. A) TEM-1 crystal structure (PBD: 1BTL) with secondary structure noted. In bold are H2 and H7, the regions associated with binding. On the right is the globular structure with H2 and H7 highlighted in blue, with the known allosteric binding region (H11) highlighted in purple. B) Chemical structure of the 3 drug substrates studied for binding activity, in order of effectiveness against TEM-1 activity (left to right).

1.5. Enzymes Involved in Energy Metabolism

1.5.1. Energy Formation in Prokaryotes and Lower Eukaryotes

The electron transport chain is a vital route for aerobic energy production in many organisms. The most common pathway for energy production occurs in the mitochondria with the

establishment of a proton gradient to generate ATP via ATP synthase. The proton gradient is facilitated primarily through two complexes, labelled as 1 and 2. Both complexes 1 and 2 are responsible for the transport of electrons to ubiquinone with proton translocation across mitochondrial membrane; complex 1 accepts electrons from NADH, while complex 2 accepts electrons from $FADH_2$[155]. Under anaerobic conditions, the oxidation of NADH occurs via the reduction of acetyl-CoA by an alcohol dehydrogenase[156]. Deficiencies in the electron transport chain (such as the reduction of NAD^+) can lead to a variety of disorders in humans and other organisms[157], underscoring the importance of studying binding interactions of these coenzymes with their enzymatic partners.

1.5.2. NAD^+ and NADH Background

Nicotinamide adenine dinucleotide (NAD) has multiple functions, most importantly as a coenzyme for the hydride transfer in alcohol dehydrogenases. NAD is also a substrate for energy consumption in a variety of other enzymatic pathways, including ribosyl transferases and glycohydrolases[158]. NAD was discovered as a potential cofactor for yeast alcohol dehydrogenase (YADH) in 1906 by Harden and Young, who were examining the fermentation pathway of yeast and postulated that some cofactors were required for yeast to generate carbon dioxide through this pathway[159]. The first examination of the redox potential of NAD was investigated by Otto Warburg in 1936 as part of his well-known work elucidating the role of oxidation in cells and cancer growth[160,161]. The oxidative properties of NAD^+ in the cytoplasm and mitochondrial matrix demonstrated that several prokaryotes and eukaryotes operate with similar NAD^+/NADH ratios, sustainable for efficient redox reactions[162]. NAD binding domains within dehydrogenases (such

as yeast) contain a conserved double β-α-β-α-β motif[163]. It is believed that having a long loop that encompasses this expanded sheet creates an ideal cavity for the insertion and binding of the adenine ring in NAD^+. YADH requires NAD^+ as a cofactor for substrate binding to initiate catalysis; binding of NAD^+ at the C-terminal end forces the enzyme into a more closed configuration to force ethanol and NAD^+ to react via a zinc ion and a narrowing of the interdomain space[164].

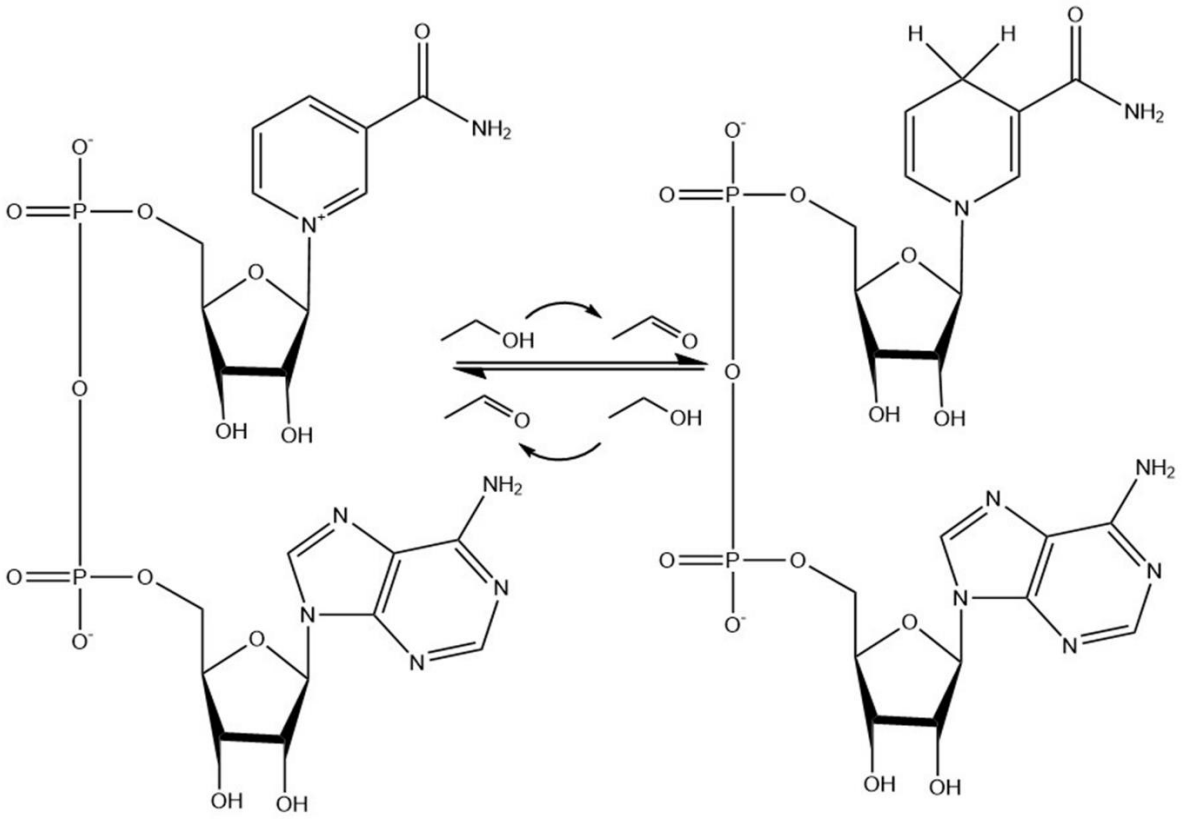

Figure 1.14 NAD^+-facilitated Ethanol Oxidation. The ability of NAD^+/NADH to participate in a reversible redox reaction makes the cofactor vital to many different enzymatic pathways in lower eukaryotes and prokaryotes.

1.5.3. Yeast Alcohol Dehydrogenase

Yeast Alcohol Dehydrogenase (YADH) is the primary enzyme responsible for the reduction of acetaldehyde to ethanol during the glucose fermentation process in prokaryotes and some lower eukaryotes[165]. There are multiple isoforms and isozymes present in a variety of prokaryotes and eukaryotes (YADH contains 3 forms[166]), the principal form being ADH1. Composed of 347 amino acid residues, ADH1 YADH has a dynamic quaternary structure and require two cofactors for catalysis. Each monomer of YADH contains 2 zinc ions, 1 involved in catalysis (either through a tetra- or penta-coordination with a water molecule[167]) and 1 that maintains structural stability away from the active site[165]. In yeast, the tetrameric form is favoured. Although the tetramer is composed of 4 identical subunits, their configuration in quaternary form is different: subunits A and C maintain a closed configuration with bound NAD^+, while subunits B and D remain open with no bound NAD^+.

1.5.3.1. Hydride Transfer and Tunneling

Enzymes accelerate the rate of reaction by stabilizing the transition state complex[168]. Typically in catalysis, reactions follow the transition state theory developed by Pauling[169], where a minimum activation energy must be obtained before a chemical reaction occurs to produce products with a lower, more stable ground state energy[170]. Tunneling thwarts this assumption, by producing a chemical reaction (the hydride transfer) without attaining the minimal energy of the activation barrier. This is achievable due to the small mass of hydrogen, a short distance between reacting species and a minimal energy barrier[171]. Given the small size of hydrogen and the short distance between the hydride donor and acceptor, quantum mechanical behaviour is predicted on the

angstrom scale[171–173]. Yeast alcohol dehydrogenase provided the first example of hydride tunnelling being observed in a macromolecule, first observed by Cha et al[174]. Hydride transfer is occurring between the alpha carbon of the alcohol present (typically ethanol) and the C4 atom of the nicotinamide ring in NAD^+. The NAD^+ molecule may undergo a conformational shift into boat conformation to help increase the molecular orbital overlap and decrease the potential energy barrier observed in this reaction[175].

1.5.4. Kinetic Isotope Effect on Catalysis of Yeast Alcohol Dehydrogenase

The Kinetic Isotope Effect (KIE) is used to identify the highest energy transition state in catalysis, and can help distinguish between concerted and stepwise mechanisms[176]. To help understand the hydride transfer mechanism, several researchers have mapped the KIE of protium and deuterium in this catalysis to quantify the remarkable isotopic dependence observed[177–179]. The primary KIE relates to the hydride transfer, while the secondary KIE is due to the aldehyde product remaining in the active site. The KIE of YADH was first reported by Cho and Northrop, who demonstrated the effect of pressure on catalytic efficiency[180].

1.5.5. Mechanism of Catalysis

The bi-bi mechanism of this redox reaction was originally proposed by Dickinson and Monger[181]. They proposed two steps to the YADH catalytic cycle: binding of the ethanol and the reduction of NAD^+ to NADH, followed by the release of NADH from the binding site. The reduction step that is dependent on the hydride transfer is traditionally considered the “burst” phase of catalysis, while the “lag” phase of catalysis is dependent on the turnover and release of NADH from the

enzyme[171]. HDX experiments have attempted to isolate the local dynamics of this burst phase with limited results, as the reactions have not been conclusively proven to give observable conformational changes on the catalytic timescale[171].

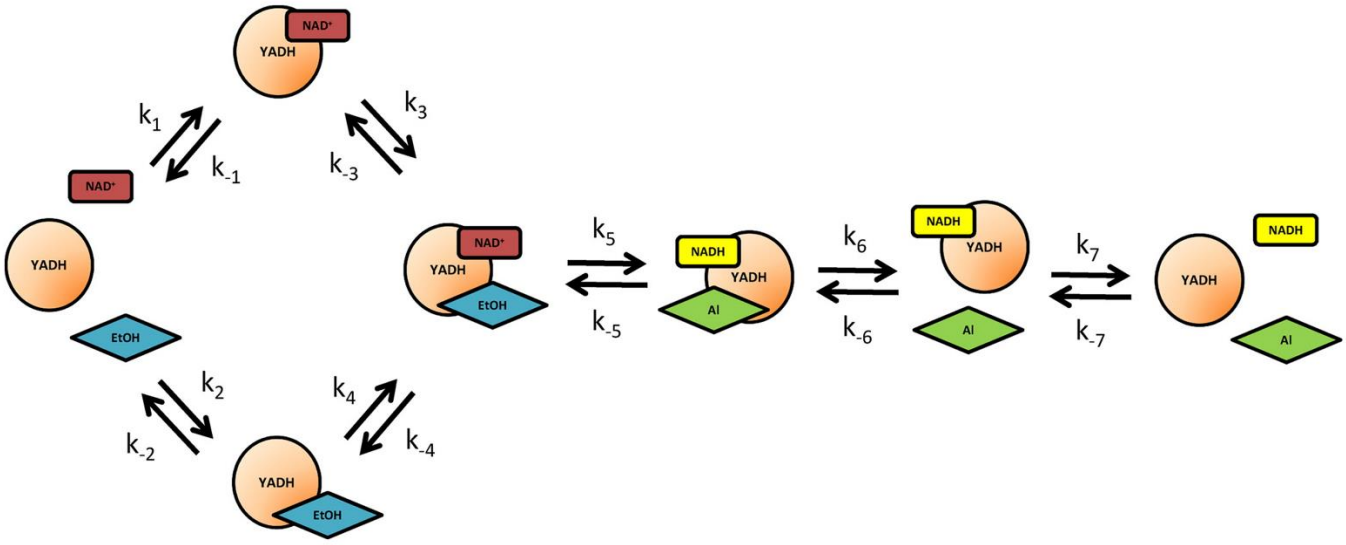

Figure 1.15 Yeast Alcohol Dehydrogenase Bi-bi Mechanism of the Catalytic Cycle In order for the redox reaction to occur, the enzyme must have NAD^+ bound as a cofactor prior to ethanol binding. Adapted from Liuni et al[178].

1.6. Research Objectives

Medicinal chemistry is constantly adapting to a changing microbial environment that presents increasing challenges as new resistance mechanisms develop and drug candidates have limited experimentation done on a catalytic time scale to deduce residue-localized binding effects. Using time-resolved microfluidic devices, herein we demonstrate the impactful utility of millisecond-scale HDX on determining conformational dynamics of enzymes as they participate in substrate

hydrolysis or redox reactions. Chapters 2-4 all employ millisecond-timescale HDX, with Chapter 3 also uses the CIU technique and Chapter 4 examines global HDX rates of catalysis to determine the effect of deuteration on hydride transfer.

Chapter 2 examines the contribution of binding modes to catalytic steps in TEM-1 β-lactamase and how time-resolved millisecond HDX can be enabled to identify these specific residues during the hydrolysis of three different classes of antibiotics.

Subsequently, in Chapter 3 we further investigate the inhibitory mechanism that is induced during the rigidification process of TEM-1 to help understand the potency of each inhibitory drug and present a more comprehensive binding affinity scale based on CIU-MS and local HDX results.

Chapter 4 examines the residue-specific impact of deuterium incorporation into the reduction of NAD^+ to NADH via YADH and ethanol, and how this allosterically impacts the quaternary structure of the YADH complex.

In conclusion, Chapter 5 discusses the impact of new microfluidic devices for use with more complex enzymatic cycles and how this will further influence drug development and structural biology.

Chapter 2

Mapping Conformational Dynamics to Individual Steps in the TEM-1 β-Lactamase Catalytic Mechanism

A version of this chapter was published in the Journal of Molecular Biology:

Knox, R.; Lento, C.; Wilson, D. J. Mapping Conformational Dynamics to Individual Steps in the TEM-1 β-Lactamase Catalytic Mechanism. *J. Mol. Biol.* **2018,** *430*, 18, 3311-3322.

2.1 Summary

Although the link between conformational dynamics and catalytic activity is commonly discussed, very few experiments have been able to conclusively isolate which regions of protein are necessary for binding modes. By studying TEM-1, a well-known protein involved in antibiotic resistance, we can identify dynamics linked to specific components of catalysis: binding, acylation and deacylation. We postulate that using ampicillin (first generation and easily hydrolyzed), cephalexin (second generation, with slower deacylation from the binding pocket) and clavulanate (third generation, complete inhibition) will demonstrate how each drug class interacts in this enzymatic process. Our research aims to discover novel binding sites in TEM-1 that may be targeted for drug development and lead to new synthetic pathways for drug synthesis that do not employ traditional lactam bond formation, such as isolating residues involved in binding (Glu166, Ser70, Ser130) and identifying regions of rigidification necessary for enzymatic inactivation (residues 273-284).

2.2 Introduction

The most commonly prescribed antibiotics, β-lactams, target cell wall synthesis in bacteria by inhibiting Penicillin Binding Proteins (PBPs) from cross-linking peptidoglycan strands in the bacterial cell wall[112,113]. TEM-1 β-lactamase is known to degrade β-lactam drugs near the diffusion limit across a wide range of penicillins and cephalosporins[182]. The rates of acylation and deacylation for different drug products and β-lactamase classes have produced indeterminate results. Cephalosporins are known to be acylated quickly but have a much slower deacylation rate than ampicillin in class A β-lactamases along with differing activity[137,183,184]. This may be in part due to the different interactions at the binding site; during acylation, the penicillin carboxylate is bonding to the C3 carbon in the

thiazolidine ring (stereogenic) while the cephalosporin carboxylate interacts with the C4 carbon (sp2, in a planar orientation)[183,185]. Class A β-lactamases in general are known to have a very fast deacylation process; the rate limiting portion of the reaction is due to the acylation mechanism[186]. From this information we expected regions with lower deuterium uptake exclusive to the cephalexin experiments to be related to the deacylation mechanism. Using our microfluidics device workflow, in conjunction with Time Resolved Hydrogen/Deuterium eXchange (TRESI-HDX) (figure 2.1), we can monitor the conformational dynamics of each catalytic process within a suitable biological environment. By plotting the differences in deuterium uptake with TEM-1 in holoenzyme and apoenzyme form, we can monitor changes associated with drug interactions and not based on native conformational fluctuations. Of particular interest are regions that demonstrate changes in dynamics with ampicillin and cephalexin but not clavulanate, as this would elucidate which regions of the protein are not involved in deacylation, along with potential regions of allostery. Based on statistically significant differences in the conformational dynamics of TEM-1 as turnover is occurring, we are able to demonstrate how TRESI-HDX can be used to guide drug development for of β-lactams and further employ this technique for binding mode analysis in other antimicrobials.

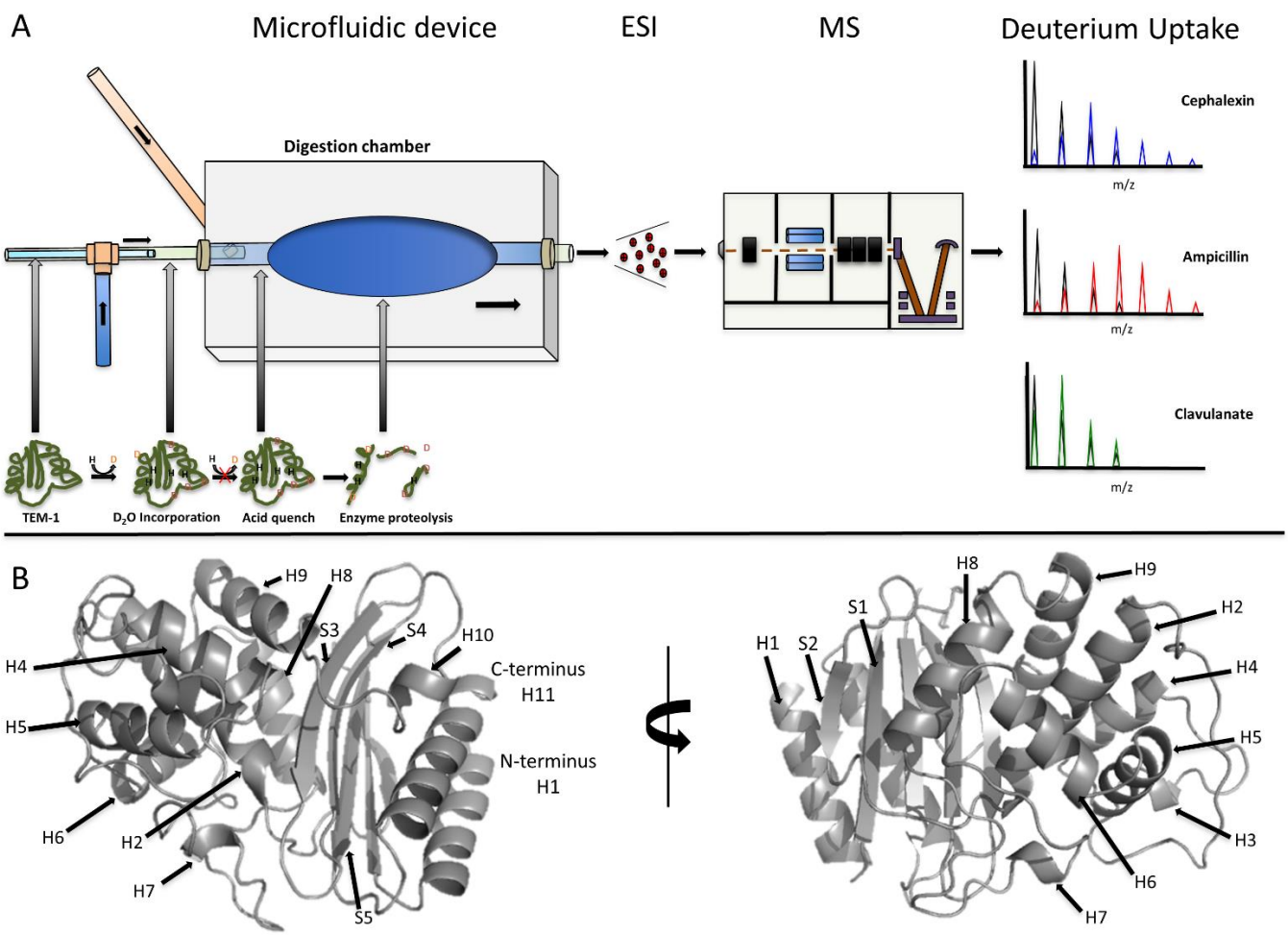

Figure 2.1 Schematic depiction of the TRESI-HDX experimental setup. A) The enclosed proteolytic chamber (PMMA) digests the deuterated protein sample prior to ESI-MS. For each substrate/inhibitor, the holoenzyme deuterium uptake is compared to the apoenzyme baseline uptake recorded on the same day. These experiments differ slightly from conventional HDX in that the substrate/inhibitor is introduced to the enzyme concurrently with the onset of HDX labeling on the millisecond timescale. This is to ensure that the enzyme is in the steady state, acylated state and/or undergoing slow turnover when the uptake measurements are made. B) The crystal structure for TEM-1 with secondary structural elements (H1-11 corresponding to helices and S1-5 corresponding to β-sheets) highlighted (PBD ID: 1BTL).

2.3 Results and Discussion

2.3.1 Native MS of TEM-1 and Formation of Acyl-enzyme Intermediates

Previous reports on TEM-1 inhibition by clavulanic acid used a 1000:1 inhibitor: enzyme ratio incubated for 1 hour at room temperature to ensure complete inactivation[187]. Neither this inhibitor: enzyme ratio nor lengthy incubation was possible in our experiment due to ESI compatibility of high substrate concentrations and our use of the "kinetic" TRESI workflow for optimal mixing[188,189]. We therefore used native mass spectrometry to characterize the global conformation of the purified protein and to determine the minimum concentration of substrate requirements for complete inhibition of the protein. These experiments were enhanced by the SpyTag system for optimal stability[190]. Ultimately, these experiments demonstrated that a 10:1 clavulanate: TEM-1 ratio was sufficient to generate fully bound protein, observed as a mass shift of 200 Da (fig 2.2). The observation of the intact bound inhibitor as a complete molecule is at odds with our current understanding of the clavulanate inhibitory mechanism, which is thought to inactivate via off-pathway processes resulting in the covalent attachment of clavulanate or fragments thereof over multiple catalytic cycles[138,183,191–194]. One possible explanation is that the inhibition process for clavulanate is sensitive to reaction conditions, and that under MS-appropriate conditions (200 mM NH4Ac, pH 6.7), initial hydrolysis of the intact molecule, corresponding to an expected mass shift of 198 Da, is highly unfavored[195].

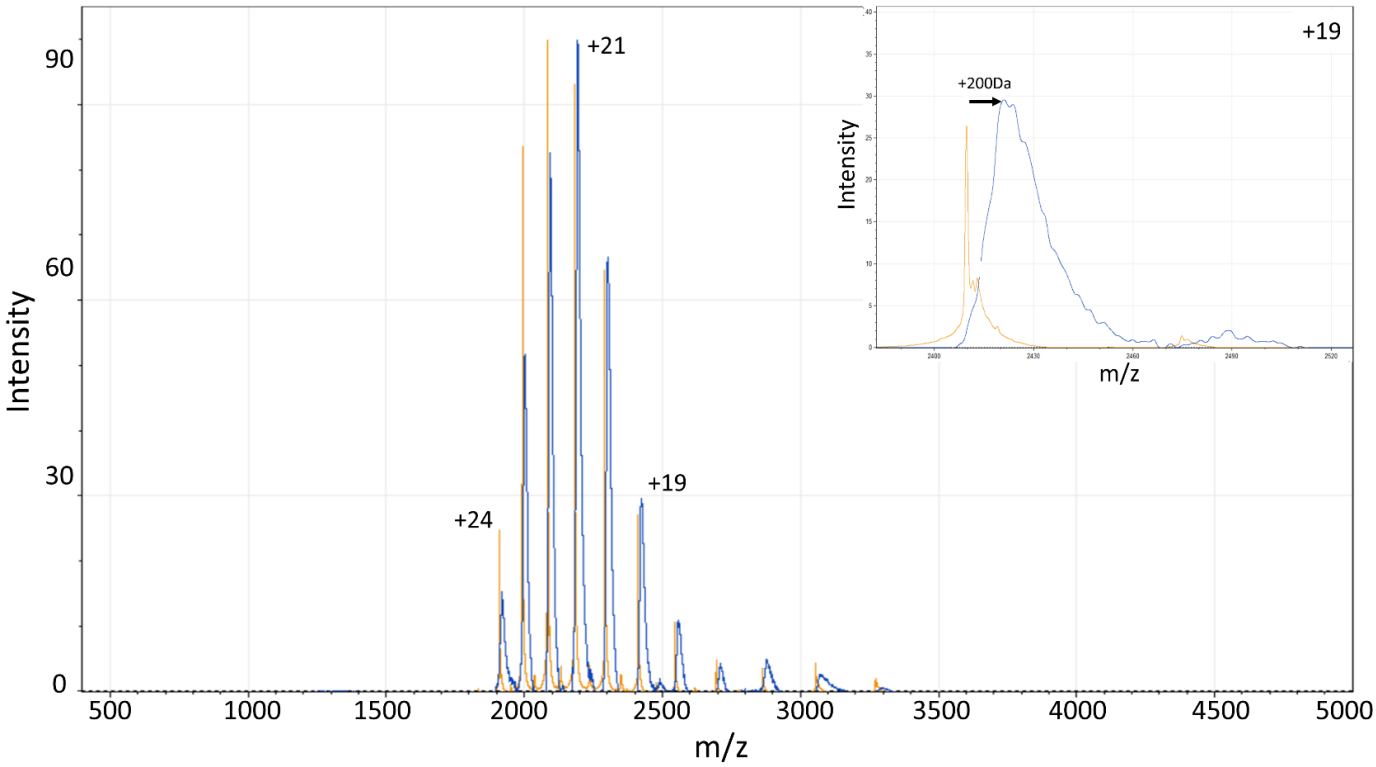

Figure 2.2 Native Mass Spectra of TEM-1 Binding Clavulanate. Native mass spectrum of TEM-1 (orange) with clavulanate-incubation after 1 hour (blue) at a ratio of 10:1 inhibitor: enzyme. Inset (top right) is the observed mass increase of +200Da at the +19-charge state, approximately corresponding to the mass of an intact clavulanate molecule (198 Da).

2.3.2 TEM-1 Conformational Dynamics in the Presence of Substrate, Partial Inhibitor and Covalent Inhibitor

We used TRESI-HDX to exclusively monitor the dynamics influenced by the protein: substrate interactions of TEM-1 in the presence of ampicillin, cephalexin and clavulanate. TRESI-HDX is a valuable tool in studying amide backbone exchange and hydrogen bonding in a protein complex, which is especially important when studying the conformational landscape of an enzyme as they interact with substrates or inhibitors[58,196]. By using a kinetic TRESI workflow, we are able to monitor conformational dynamics of enzyme catalysis on a millisecond-to-second timescale[188,189] and

observe the substrates in steady state rapid turnover (ampicillin), slow turnover (cephalexin) or covalent inhibition (clavulanate) as the hydrogen/deuterium exchange is occurring. Figure 2.3 depicts the relative conformational changes between the substrates and apo-enzyme at 1.54s, with each colored bar depicting residues that show significant changes in dynamics. Although the amount of residue coverage for each substrate is not identical (ampicillin, 85%; cephalexin, 66%; clavulanate, 80%), the binding region and known areas of high mutational activity are covered with an 80% overall shared coverage. For figure 2.3, regions in red are those with statistically significant increase in dynamics relative to the apo-enzyme, while blue regions denote a significant decrease, shown as a dotted line (>2σ, n=9). Figure 2.3 gives a broad snapshot of the conformational dynamics sequentially, with inference made about the spatial dynamics through large regions of uptake or decrease. Appendix A displays results for each kinetic and equilibrated local HDX experiment.

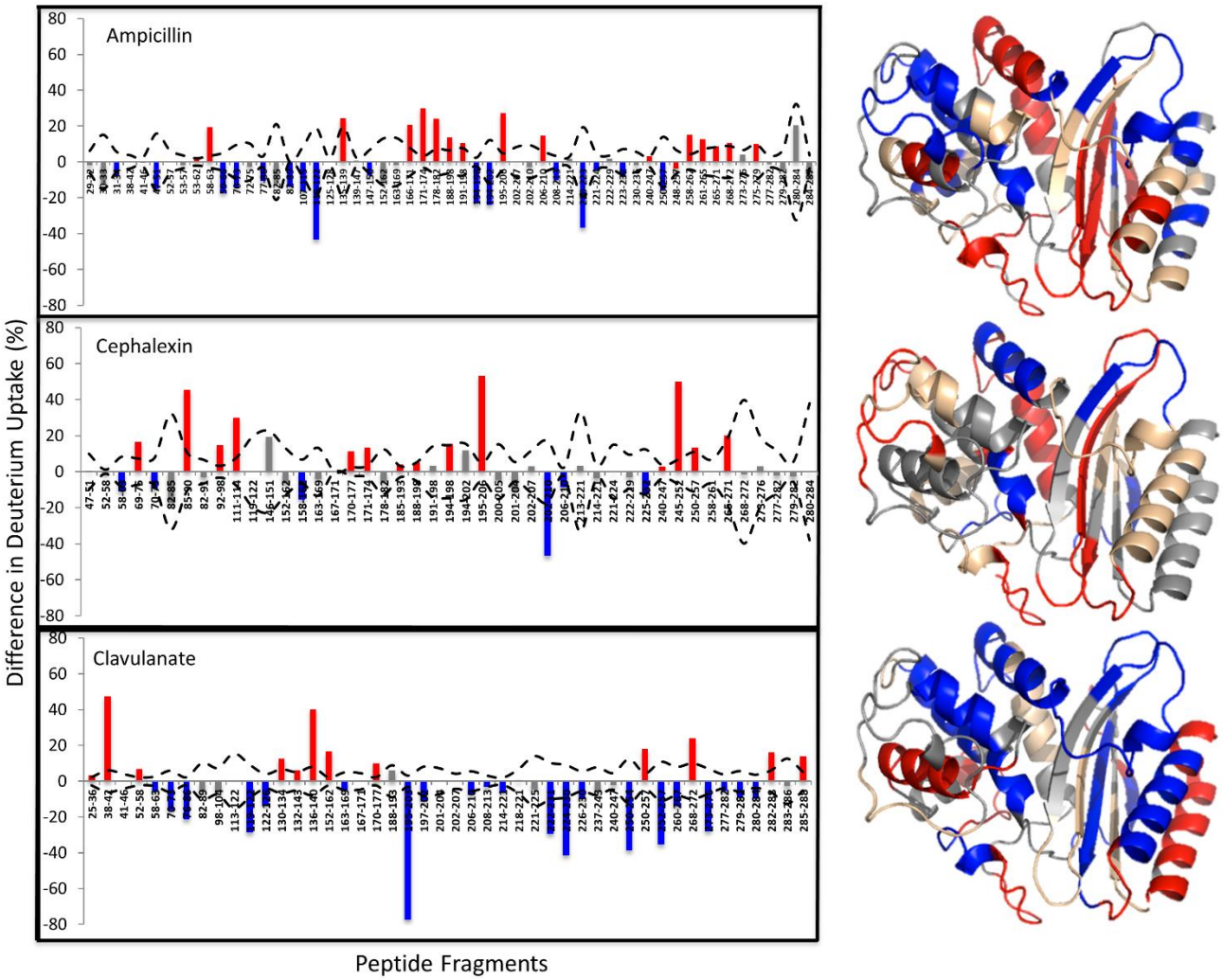

Figure 2.3 Time-Resolved Deuterium Uptake for TEM-1 with 3 Substrates. Single time-point TRESI-HDX difference measurements at 1.54s comparing holoenzyme TEM-1 to TEM-1 exposed to saturating concentrations of ampicillin, cephalexin and clavulanate (from top to bottom). Positive (red) bars indicate increased uptake relative to the free protein and negative (blue) bars denote decreased uptake relative to the free protein. Right: Peptides with significant changes (> 2σ, n=9) are displayed on the crystal structure, PBD ID: 1BTL using the same colour scheme (with the addition of gold = no change, grey = unobserved).

With ampicillin-incubated TEM-1 there are regions of both increased and decreased deuterium uptake with catalytic turnover, with exclusive dynamics within the S3-S5 β-sheets and rigidification

of H3 and S1. As ampicillin is the only substrate under study with rapid hydrolysis by TEM-1, we can isolate changes in dynamics that are exclusive to the ampicillin profile as being linked to efficient deacylation. The same logic is applied to the other two substrates and their interaction with TEM-1. For the profile with cephalexin (fig 2.3, middle), we correlate the known behaviour of inefficient hydrolysis to the unique changes in deuterium uptake, such as increased dynamics in the H3/H4 loop, S4 and the S4/S5 loop. These key regions are known to contain mutational sites and salt bridges of importance for protein stability, inferring that inefficient deacylation is associated with increased flexibility. If comparing ampicillin and cephalexin HDX profiles, it is possible to distinguish further regions that participate in deacylation, but with differing intensities, such as H3/H4 loop where ampicillin has an increase in uptake and cephalexin decreases. For clavulanate, changes in uptake that correspond to a unique dynamic profile (relative to cephalexin and ampicillin) can be linked to deacylation failure. Additionally, regions of increased dynamics that are exclusive to cephalexin and ampicillin can also be inferred as being involved in the hydrolysis of the acyl-enzyme (such as H8 and S3/S4 increases in uptake). Finally, for regions that behave similarly with all 3 substrates, we can infer that they must be involved in the binding process of substrate hydrolysis.

Although conventional HDX may be able to offer a global overview of perturbations to the hydrogen backbone of a protein, the dynamics associated with capturing transient intermediates or relative rates of each mechanistic process are best observed on the ms timescale. By using TRESI-HDX, we have been able to identify different regions of interest in the TEM-1 hydrolysis of ampicillin, cephalexin or clavulanate, and correlate these regions to specific functional roles in the hydrolysis of the substrate.

2.3.3 Backbone Dynamics of TEM-1 during Binding

As binding is the only mechanistic process in which all 3 substrates are known to behave similarly (due to kinetic studies and structural similarities), regions with dynamic modes associated with binding should exhibit similar (within 2σ) uptake profiles. The first region that matched these criteria was residues 70-73 (N-terminus of H2), well-known as the conserved SXXK motif responsible for the Ser70 binding site in all Class A β-lactamases. All substrate-bound TEM-1 complexes exhibit a decrease in dynamics relative to the apo-enzyme (figure 2.4, top), with approximately 25% less uptake than unbound TEM-1. This suggest a single amide bond suppression of dynamics or inaccessibility of exchange, either due to binding of the substrate or a conformational change that generated new hydrogen bonding within the active site. Although there is no crystallographic evidence for the direct binding of clavulanate within the active site, it is possible that rearrangement of the backbone amides with incubation generated a hydrogen-bond link between Ser70 and Lys73[144].

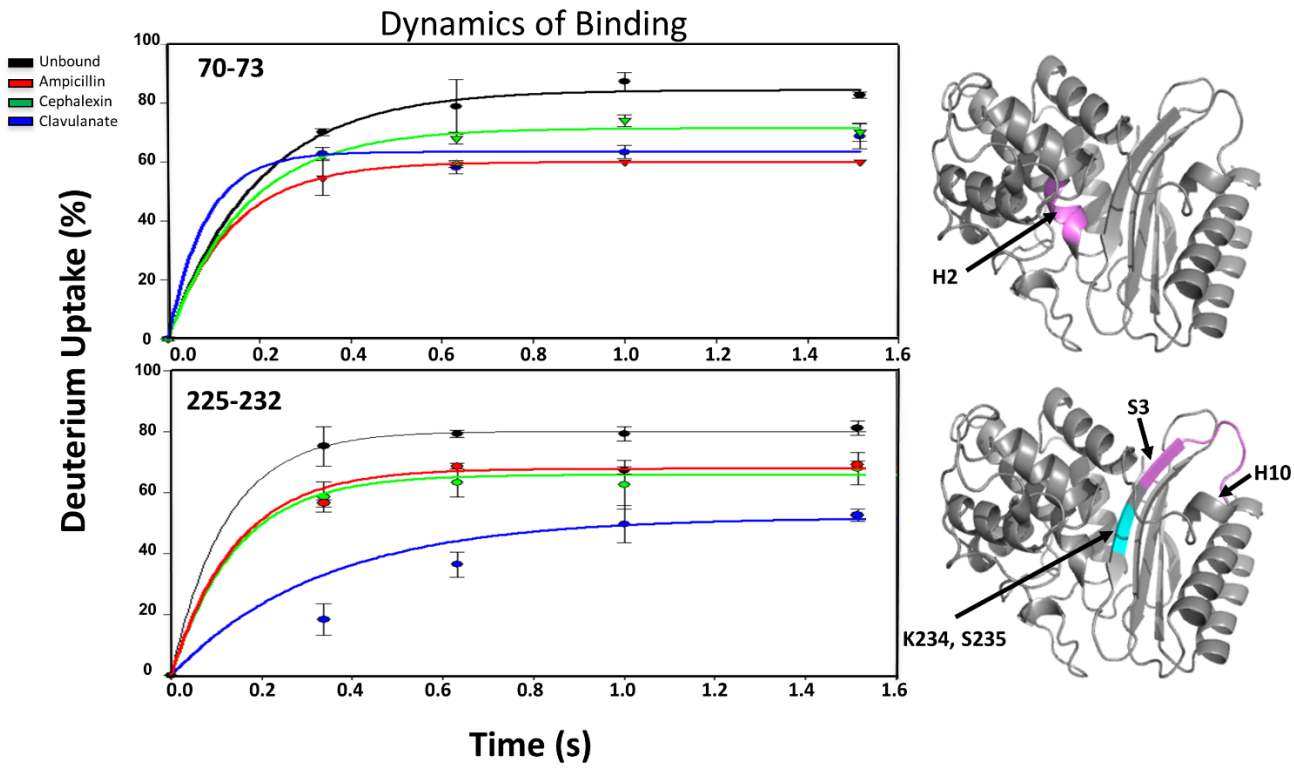

Figure 2.4 Kinetic Deuterium Uptake for Binding Dynamics of TEM-1.TRESI-HDX kinetics plots for dynamics of binding (top, residues 70-73; and bottom, residues 225-232) are displayed for each drug product (ampicillin, red; cephalexin, green; clavulanate, blue) for comparison to the unbound TEM-1 profile (black line) (1σ, n=9). Crystal structures to the right display the relevant peptide fragment in pink, with nearby residues of importance highlighted in teal.

Another region, residues 225-232, also exhibits a decrease in deuterium uptake with all three substrates (fig 2.4, bottom). Corresponding to the H10/S3 loop, this region is part of a larger section of the protein recently discovered as an allosteric binding site[197]. Interestingly, inhibitors that have been known to bind within this region are productive because they are able to physically separate H11 and H10, suggesting that decreased dynamics between these helices is necessary for catalysis to occur. Known residues of high mutational activity are sequentially very close to this region: Ser235 is of importance for cephalosporin resistance, and Lys234 is necessary for hydrogen bonding of

incoming substrate into the active site[183]. With known evidence of surrounding residue involvement in binding and stability of the protein, our observations agree well with the idea that decreased dynamics in residues 225-232 are linked to substrate binding.

2.3.4 Backbone Dynamics of TEM-1 during Productive Acylation

Productive acylation refers to the successful process of acylation of the β-lactam core followed by hydrolysis of the complete small molecule, which is carried out efficiently with ampicillin-bound TEM-1, and slowly with cephalexin-bound TEM-1. Since both ampicillin and cephalexin are hydrolyzed by TEM-1, they should exhibit similar dynamics profiles for deuterium uptake and be significantly different than the clavulanate profile, allowing us to isolate regions that are exclusive to clavulanate activity. Residues 240-247 (fig 2.5, top) demonstrates a minor increase in deuterium uptake with acylation occurring, and a significant decrease in uptake when acylation does not. Within this region is the critically important Arg244, known for forming salt bridges and ionic bonds responsible for stabilizing protein structure through tethering of substrate carboxylate group during acylation[198]. This region gives direct evidence of the difference in turnover rates of each substrate, as the ampicillin profile shows a rapid and high amplitude of deuterium uptake, which can be linked to more intense dynamics and a greater number of exchangeable sites on the timescale as observed with rapid turnover[85]. In contrast, cephalexin has a slower increase in deuterium uptake, but eventually demonstrates the same overall rate for uptake as ampicillin. This is likely due to the slower and complete turnover of cephalexin ($k_{cat} = 13 \pm 1\ s^{-1}$)[199], which requires multiple turnover events to achieve maximum deuteration.

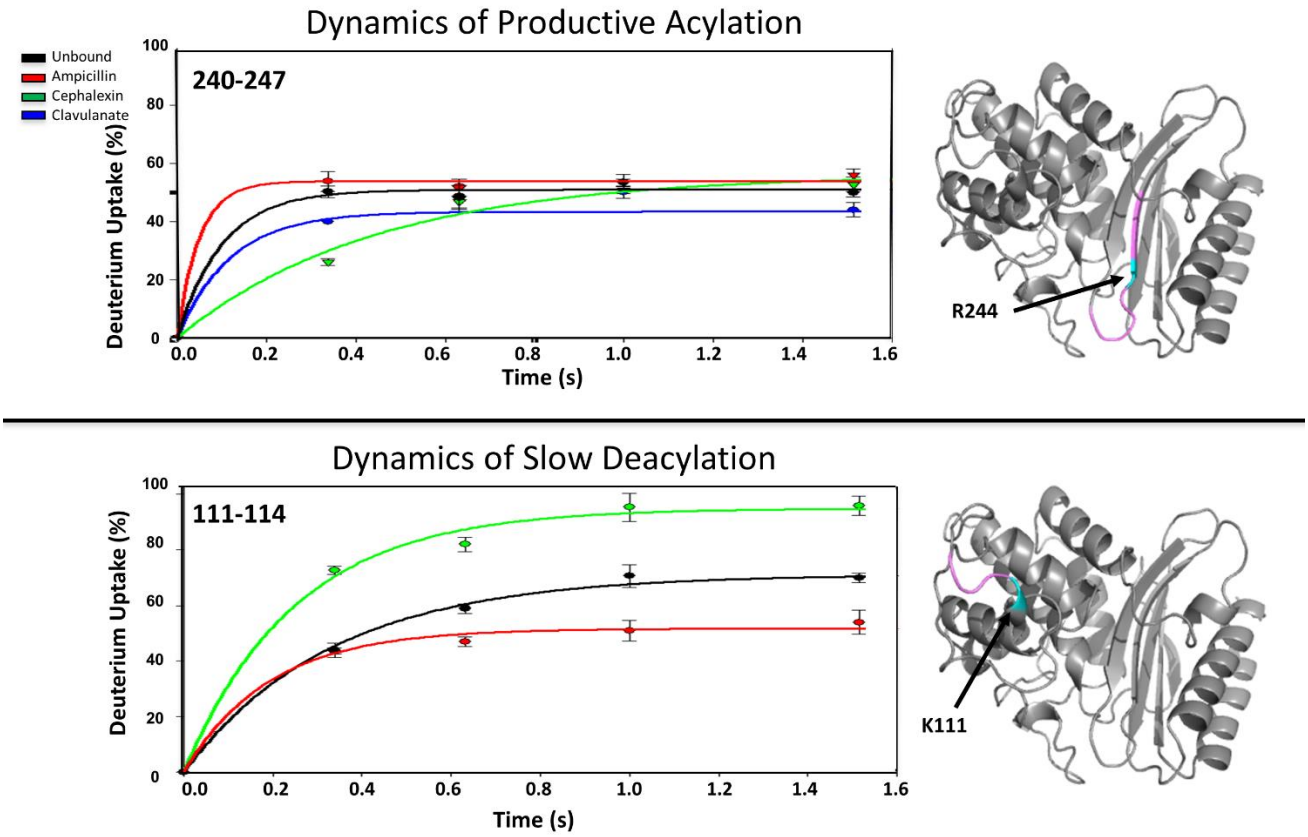

Figure 2.5 Kinetic Deuterium Uptake for Acylation and Deacylation Dynamics of TEM-1. TRESI-HDX kinetics plots for dynamics of productive acylation (top, residues 240-247) and slow deacylation (bottom, residues 111-114) are displayed for each drug product (ampicillin, red; cephalexin, green; clavulanate, blue) for comparison to the unbound TEM-1 profile (black line) (1σ, n=9). Crystal structures to the right displays the relevant fragment in pink, with nearby residues of importance highlighted in teal. The exact uptake at 111-114 in Clavulanate-bound TEM-1 was not recovered during experimentation, however the region is depicted in overlapping fragments showing minimal change relative to the unbound TEM-1 (shown in figure 2.3).

For clavulanate, we observe a noticeable decrease in deuterium uptake on this timescale, with at least one residue becoming inaccessible for exchange. Since Arg244 is known to have complexation with the carboxylate group of the incoming clavulanate during binding[200], reduced deuterium uptake in this region is associated with deacylation failure.

2.3.5 Backbone Dynamics of TEM-1 during Slow Deacylation

Slow deacylation dynamics are exclusive to cephalexin and cephalosporin-family drugs for these experiments. Cephalosporins are known to have increased potency over first-generation penicillins due to their slower turnover and decreased deacylation from the binding site[183]. Therefore, changes in dynamics observed by TRESI-HDX that are exclusive to cephalexin are associated with the inefficient hydrolysis of the acyl-enzyme. In figure 2.5 (bottom), residues 111-114 of the H3/H4 loop are depicted. Within this region is the highly mutational residue Lys111, which has increased mutational frequency and resistance in the presence of cephalosporins (specifically cefotaxime)[201]. This link between cephalosporin resistance at K111 and our kinetic workflow must be taken with a grain of salt, as we cannot measure deuterium exchange at the N-terminal residue of peptides[72]. Another region that corresponds to the above criteria for slow deacylation is residues 245-257, corresponding to the S4/S5 loop. This region is depicted in figure 2.3 as having unique dynamics to cephalexin, but unfortunately was not recorded in triplicate for all substrate runs in order to generate kinetic plots. However, partially overlapping regions such as 240-247 and 250-257 suggest that increased deuterium uptake is unique to the cephalexin trials. As mentioned earlier, regions known to evolve mutations as part of cephalosporin resistance such as Arg 244 are identified within this region (Ile247, Ala249, Asp254, Lys256)[201], potentially demonstrating that additional flexibility within this region for substrate hydrolysis is necessary. This region should be further targeted for development of co-inhibitors to limit cephalosporin resistance by rigidifying the 245-257 region.

2.3.6 Backbone Dynamics of TEM-1 during Deacylation Failure

Only the clavulanate substrate has an inhibitory effect on TEM-1 for this study, as such, changes in dynamics that are exclusive to clavulanate binding can be linked to a failure to deacylate from the binding site. One region identified as showing a unique and significant decrease in deuterium uptake is residues 250-257 (fig 2.6, top), which corresponds to the S4/S5 loop of TEM-1. These results agree with our previous discussion of the S4/S5 loop involvement in cephalosporin activity (for residues 245-257). We suggest that dynamics within 250-257 are linked to deacylation, with variation depending on the family of drug used: high flexibility/dynamics for hydrolysis of bulkier substrates (cephalexin), moderate flexibility for smaller substrates (ampicillin) and lowered flexibility/rigidification for deacylation failure (clavulanate).

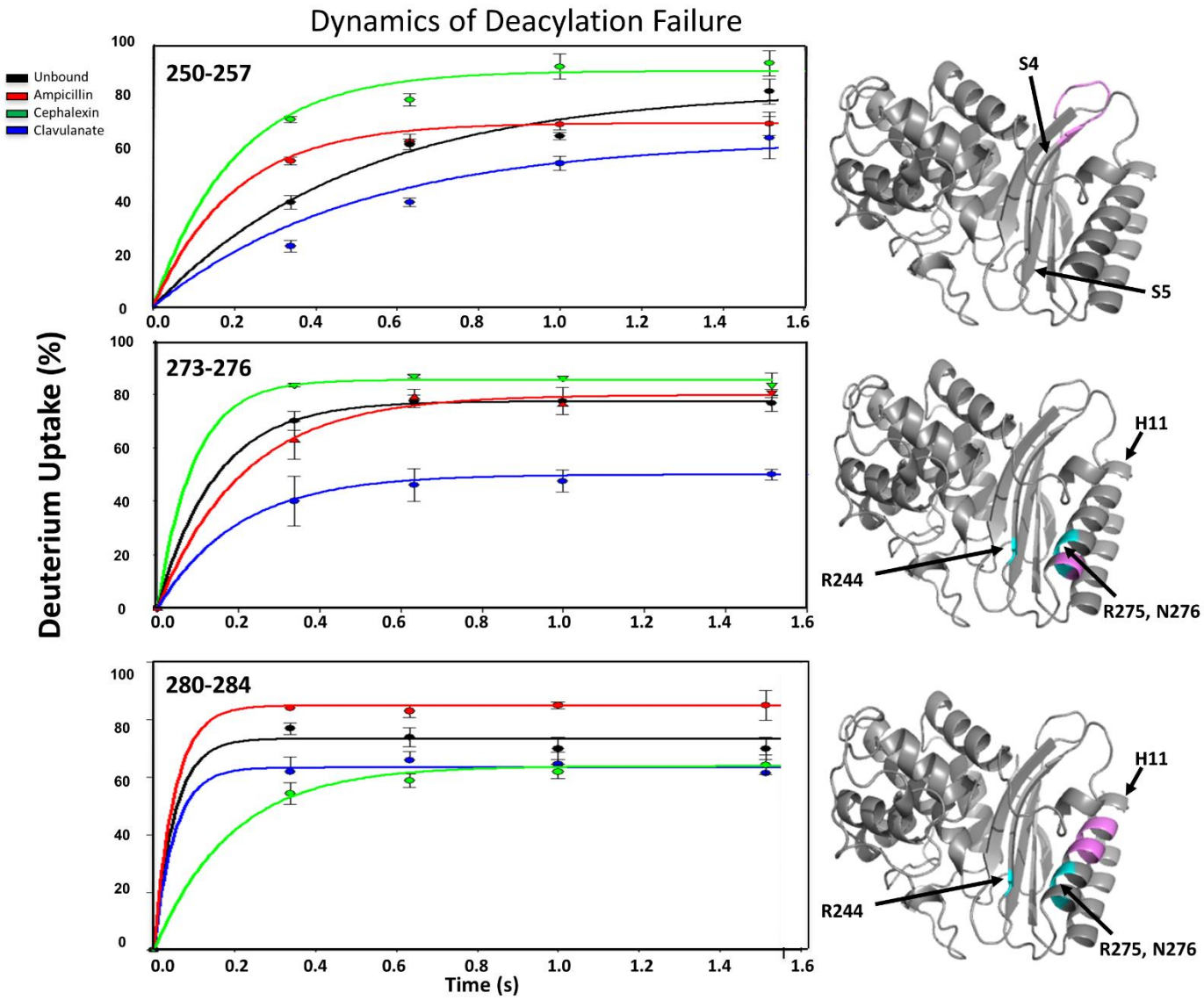

Figure 2.6 Kinetic Deuterium Uptake for Inhibition Dynamics of TEM-1. TRESI-HDX kinetics plots for dynamics of deacylation failure (top, residues 250-257; middle, 274-276; bottom, 280-284) are displayed for each drug product (ampicillin, red; cephalexin, green; clavulanate, blue) for comparison to the unbound TEM-1 profile (black line) (1σ, n=9). In residues 280-284, cephalexin does not have a statistically significant decrease (> 2σ) relative to the unbound TEM-1. Crystal structures to the right displays the relevant fragment in pink, with nearby residues of importance highlighted in teal.

Residues 273-284 (fig 2.6, middle and bottom) all correspond to the C-terminal helix (H11), substantially distant from the active site. However, there are a number of high mutational frequency site contained within this region, such as Arg275 and Asn276, highly associated with resistance to inactivation by clavulanate via displacement of the water molecule involved in the inactivation pathway, or through interactions with Arg244[202]. Asn276 mutational studies have also provided a demonstration of decreased catalytic efficiency with mutations at this residue, and higher K_i for clavulanate, demonstrating further evidence of the importance of H11 interactions and the active site[202]. Residues 280-284 (fig 2.6, bottom) correspond to the allosteric inhibitor site discussed previously at the interface of H10/S3. Residues 280-284 have a decreased and similar uptakes for cephalexin and clavulanate, with much slower uptake kinetics exhibited by cephalexin.

2.4 Conclusion

TEM-1 has been the principal β-lactamase under study for decades, providing a wide variety of mutational residue analysis and kinetic characterization of a variety of drug substrates and inhibitors[203,204]. Along with sequence-specific analysis, there are a large amount of NMR and X-ray structures that can help provide structure/function relationships. With all of this in-depth structural knowledge, TEM-1 is an ideal system for implementing TRESI-HDX to provide insight into the mechanistic implications of each drug family as studied under fast reaction conditions. Although HDX does require a basic crystal structure to guide the mapping of dynamics, it is a highly sensitive tool for determining changes in conformational dynamics due to the presence of a substrate or inhibitor. Herein we demonstrate how TRESI-HDX can be used to compare apo and holo-enzyme forms of TEM-1 β-lactamase in terms of changes in dynamics, not structure. From this, we have identified regions

with dynamics linked to specific mechanistic processes as a means of isolating catalytically important residues for drug development. Based on the results discussed above, two regions have been mentioned more than once as important in substrate resistance and catalysis: residues 250-257 (S4/S5 loop) and residues 273-284 (H11). Residues 250-257 are linked to cephalosporin-family resistance, with varying levels of dynamics responsible for differing substrate binding. Results herein demonstrate that moderate rigidification of this region by a co-inhibitor would sensitize TEM-1 to cephalosporins (instead of penicillins), renewing their potency and providing a longer shelf life for current on-the-market cephalosporins, such as cephalexin. Residues 273-284 have been discussed above as potentially being involved in the docking of allosteric inhibitors through rigidification of this region[205–207]; work by Horn[197] has demonstrated that this region contains a small molecule binding site that operates independently of the SXXK motif. Our results have shown that turnover can be related to the degree of flexibility in H11, and rigidification with an inhibitor bound may be key to inhibiting catalysis[98,197]. This approach of millisecond-scale HDX is well-suited for studying various catalytic systems that have turnover events within the observable timescale, especially for studying protein systems where there is limited structural or biochemical information known to provide a link between enzyme catalysis and conformational dynamics[208–211].

2.5 Methods

Reagents

All chemicals were purchased from Sigma Aldrich. Buffer solutions and water used was generated in lab using a Millipore Milli-Q Advantage A10 system.

2.5.1 Expression and Purification of TEM-1 β-lactamase

TEM-1 β-lactamase with a SpyTag/SpyCatcher tag was purchased from AddGene (plasmid #52656, pET28a vector). Plasmids were extracted from the DH5α cell line into competent BL21 (DE3) cells. Cells were expressed in LB broth with 50mg/mL Kanamycin and 1M glucose. 1M IPTG was added once log phase absorption was reached (A_{600}=0.5-0.7). The culture was incubated at 18^{o}C for 16 hours at 200 rpm before centrifugation (6000g, 15 minutes, rotor JA 25.1). The pellet was resuspended with 1mM PMSF (120 µL) and 1mM protease inhibitor (120 µL) with Ni-NTA binding buffer (12 mL, 50mM Tris and 300 mM NaCl, pH 7.8). The cell solution was lysed using a Fisher Scientific Sonic Demembrator Model 500 and then centrifuged. Protein was eluted on a Ni(2^{+}) sepharose resin column with 75mM Imidazole and buffer exchanged in 250mM ammonium acetate (pH 6.7) for at minimum 36 hrs prior to evaluating protein concentration. BCA assays and SDS-PAGE analysis were performed to determine protein concentration.

2.5.2 Digest Preparation

Protease XIII or Pepsin protein with NHS activated agarose (2:5 *w/w*) was suspended in coupling buffer (0.1M sodium phosphate and 0.15M NaCl, pH 5.5) and rotated overnight at 4^{0}C. The aspirated protease was then suspended in 1M Tris-HCl blocking buffer (pH 5) and rotated at room temperature for 1 hour. The beads were washed three times with acetic acid (pH 2.4) and stored at 4^{0}C to be used in subsequent runs.

2.5.3 Chip Design

Previous chip designs by our lab have been discussed[212,213] that formed a digestion well by using a plastic seal over PMMA plates and were clamped using a customized holder. The chip was designed

in lab using a VersaLaser™ to etch a well into a PMMA plate measuring 5.1cmx2.0cmx1.2cm. A newer chip design was generated using the CorelDrawx3 program. The well was cleaned with methanol and etching was repeated. The procedure is then repeated with an identically sized PMMA plate. The paper backing on each plate was removed, with plates then being lined up together to generate a well between the chips. Capillaries were left at opposite ends to provide channels into the well while the two plates were clamped together. A needled bottle containing acrylic weld was inserted into the middle of the well and acrylic was dispensed until edges were sealed. The solution set for 1 minute before removing the capillaries. A needle was inserted into the well for aeration of the chip. The chip was dried for 48 hours, then bored into by a drill press using the 10-32 NF bit. The depth was set to 9 mm. The chip was drilled from both ends, using a methanol rinse throughout. Excess plastic caught inside the well was removed with a needle. A 10-32 NF bottoming tap was manually inserted into both ends of the chip to add the threads. The inside of the chip was washed with water to ensure all debris was removed. Acrylic weld was flowed through the well and excess was tapped out immediately. The chip was dried for another 48 hours. A 33-gauge stainless steel metal capillary was cut into two pieces with a rotary tool (with each piece being approximately 10 cm long) and sanded to smooth the ends. The metal capillaries were added as input and output channels on the chip by screwing into the ends via double-winged nuts.

2.5.4 Microfluidics Workflow

The 28-gauge metal capillary of the TRESI mixer had an inner diametre of 178.8 µm, while the glass capillary inserted within had an outer diameter of 151 µm. The protein flowed into the device at 3 µL/min, as did the deuterium and substrate capillary. The acid was introduced at a rate of 12 µL/min.

The protein and deuterium mixtures join in the intercapillary space before reaching the tri-union, where acid quenches the hydrogen exchange and limits it to backbone amide hydrogens. The volume of intercapillary space for deuterium incubation can be altered to give time-dependent incubating results by adjusting the inner glass capillary position in relation to the outer metal capillary. The quenched protein is then digested in the PMMA well (containing the proteolytic digest described above) before being sprayed into the Synapt G1 Time-of-Flight (ToF) instrument with a source voltage of 2700 V in positive ion mode.

2.5.5 Data Analysis

ESI-MS data was obtained in the 350-1500 *m/z* range. A 250mM ammonium acetate solution (pH 6.7) was used to buffer exchange TEM-1 prior to experimentation. A 10:1 TEM-1: substrate ratio was used to ensure the reaction could still be monitored by ESI after the time taken for solutions to incubate in the capillaries. Experiments were run in triplicate each day for every enzyme/substrate combination, with deuterium uptake per peptide being averaged over matching peptides from a biological replicate (n=9). Multiple purifications of TEM-1 were performed and similar results for matching peptides were obtained, with significant differences referring to a confidence interval of 95% (2σ). Peptides were identified using ExPASY Proteomics. MS/MS analysis was performed in V-mode to confirm the peptide identity (using mMass) before complete uptake analysis by manually ramping the trap collision energy from 30 to 50 V, having a 1 second scan time and recording in the 100-2000 Da range. Deuterium uptake per peptide was calculated using in-house FORTRAN software that matches the experimental uptake to the predicted isotopic distribution for the native peptides.

Chapter 3

Collision-Induced Unfolding and Hydrogen/Deuterium Exchange Mass Spectrometry as Tools for Comparing Binding Affinity of TEM-1 β-lactamase Inhibitors

A version of this chapter has been prepared in manuscript format.

3.1 Summary

Inhibition pathways in β-lactamases are of increasing interest in the medicinal community with antibiotic resistance on the rise. By examining the binding affinity of all current class A β-lactamase inhibitors through a variety of techniques, including local HDX and CIU-MS, we were able to identify the inhibited residues for the enzyme: substrate complexes, depending on concentration of substrate during incubation. With a substantial inhibitor: enzyme ratio of 1000:1, binding is observed after 10 minutes of incubation, with tazobactam-incubated TEM-1 demonstrating complete inactivation and formation of a +52Da byproduct after 60 minutes at the Ser70 residue. With a lower ratio of 10:1, sulbactam and tazobactam samples demonstrate late-onset binding and eventual inhibition of the Ser130 residue, in contrast to the 1000:1 inhibitor concentration. Specific residue regions (70-73, 161-179, 220-251, 270-284) have been identified as the most crucial for substrate inhibition for clavulanate, sulbactam and tazobactam.

3.2 Introduction

TEM-1 β-lactamase is an enzyme generated in predominantly gram-negative bacteria as an evolutionary step to hydrolyze antibiotics, most of which contain a β-lactam core[97,98,124,203]. In response to the increasing futility of employing β-lactam core drugs, inhibitory drugs were developed in the early 1970s as a supplement to β-lactam drugs in the hopes they would reduce resistance to the original drug substance. Through covalent binding to the active site of TEM-1, inhibition byproducts are produced that are cleaved fragments of the original substrate (originating from the leaving group on C-5 of the 5-membered rings)[112,195]. The inhibitory drugs on the market (used in conjunction with β-lactam drugs) are clavulanate, tazobactam and

sulbactam, each with unique reactivities[120,187]. Clavulanate (produced in the 1970s) is the most common and most potent β-lactamase inhibitor[214] in Class A β-lactamases when taken with penicillins (as determined by IC_{50} results and K_i values)[215], but is much weaker than the sulfonated products sulbactam and tazobactam when paired with cephalosporins[195,216,217](such as cephalexin, a drug studied in previous publication[55]). Along with a limited amount of inhibitory β-lactam drugs on the market, little is mentioned about the byproducts of enzyme inactivation produced by each inhibitor and how this affects the rate of inhibition of different β-lactamases[218,219]. The inhibitors inactivate through a series of off-pathway intermediates, thought to covalently cross-link a serine residue (Ser130) to the active site (Ser70) after a series of imine-enamine conversions (figure 3.1)[194,202,215,220–222]. The resulting fragmented alkyl chain would be permanently bound to a residue within the active site, inhibiting substrate hydrolysis of incoming drug substrate. Peptide-level Hydrogen/Deuterium Exchange mass spectrometry (HDX-MS) is an ideal technique to confirm the specific residues involved in permanent deactivation of the active site and determine if these residues are unique to the inhibiting substrate. By using a novel microfluidics apparatus, it is possible to observe the enzyme inactivation in a time-resolved fashion[223]. These results at a local level can be paired with more global protein structure determination by mass spectrometry, such as collision-induced unfolding (CIU). CIU is a relatively new technique used in analytical and medicinal mass spectrometry to provide evidence of comparative binding affinity between protein substrates[45–48]. The protein sample is bombarded with neutral gas at increasing voltages to encourage intermolecular collisions, with weakly-bound proteins unfolding at a lower voltage than strongly bound substrate. Protein unfolding is captured using ion-mobility mass spectrometry (IMS-MS)[32,33] which measures the collisional cross-section

and drift time of all ions passing through the IMS cell, and can distinguish them by size, shape and stability[39,40]. This practice is paired with protein-ligand binding to provide a comparison of binding affinity between ligands or drug substrates and the tertiary structure[45,224,225]. Given the stability and prevalence of TEM-1 in the global microbial population, it is an ideal target for a combinatorial study using these techniques. We postulate that using HDX in conjunction with time-resolved HDX-MS[226] and CIU will provide a more comprehensive analysis of the three inhibitory drugs currently on the market and provide further evidence for the differences in mechanistic pathways and binding affinity. This is turn will help direct synthetic chemists to more optimal structures that will provide greater binding affinity and inhibition against TEM-1 and related Class A β-lactamases.

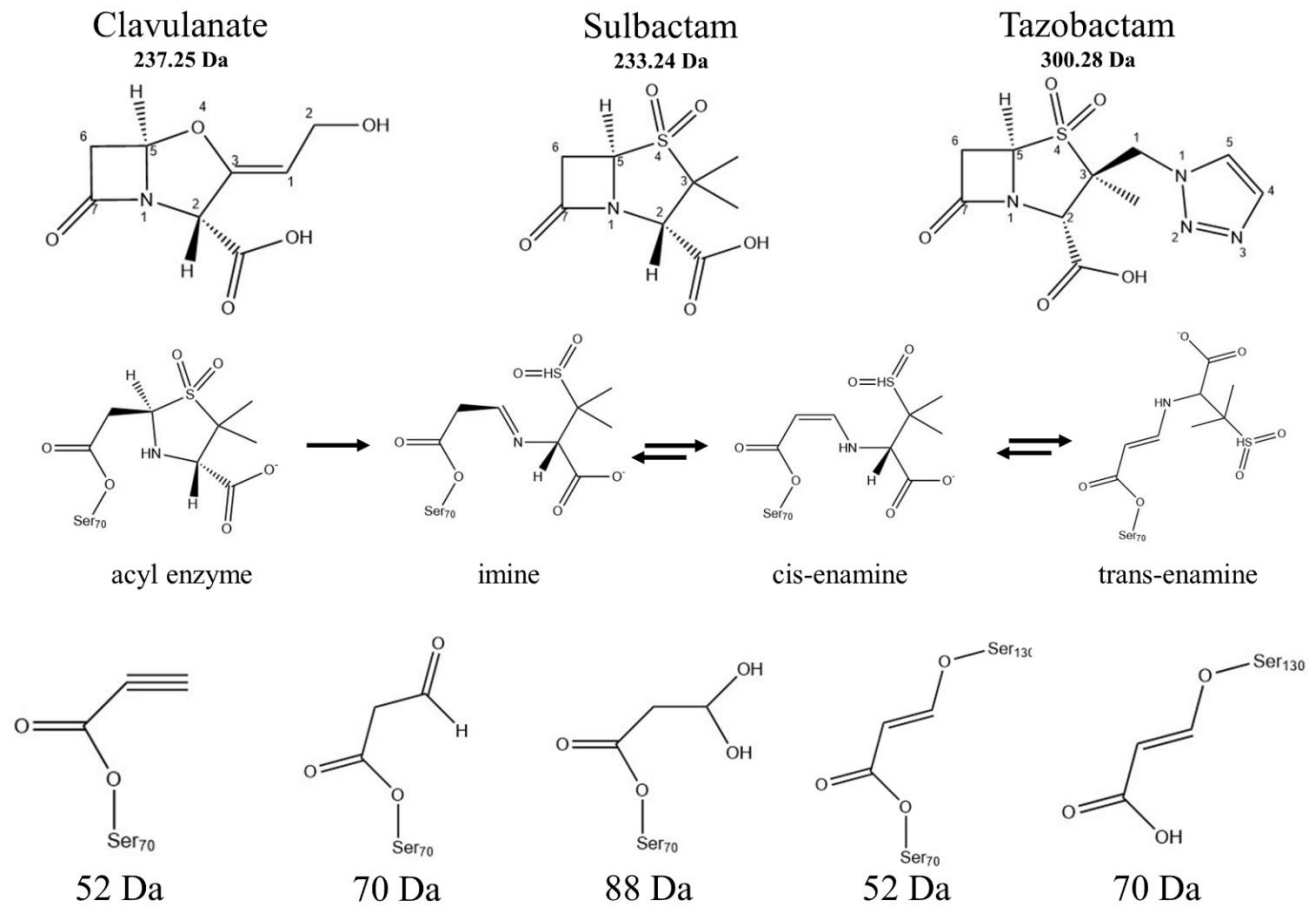

Figure 3.1 TEM-1 Inhibitors and Potential Fragmentation Products. Chemical structures of TEM-1 inhibitors, along with potential inhibition fragments generated and isomerization of the sulbactam hydrolysis pathway. From the most common fragmentations shown above, it is clear that hydrolysis of substrate generates a limited amount of mass variation. Peptide-level mass spectrometry using HDX allows us to observe local binding and distinguish which serine residues are ultimately responsible for inactivation.

3.3 Results

On the market inhibitors irreversibly inactivate TEM-1 (and various other β-lactamases) through covalent bonding at varying concentrations, with tazobactam and clavulanate having similar potency compared to a much weaker sulbactam in *in vivo* studies[215]. Surprisingly, having an excessive ratio of

inhibitor to protein involved in the inactivation of TEM-1 has be known to produce lower rates of inactivation than expected[120,220,227] and having drastically different ratios in inhibitor to enzyme incubation has previously resulted in changes in intermediates formed for many β-lactamases[228]. We sought to correlate assay binding affinity results (for a fixed inhibitor concentration) to byproduct generation (and the favoured mechanistic pathway) of each irreversible inhibitor by multiple types of experiments. By incubating the samples with molar concentrations of 10:1 and 1000:1 inhibitor: enzyme, we seek to compare mass spectrometry results to *in vivo* studies (Sulbactam, K_i=0.9 μM; Clavulanate and Tazobactam, K_i=0.1 μM)[215] and determine if different inhibitory products are apparent with greater enzyme saturation.

3.3.1 Measuring Inhibitor Byproduct Formation by Mass Spectrometry

Before looking at the binding affinity results by collision induced unfolding (CIU) of the protein: substrate complex, the native mass spectrometry must show effective binding at both concentrations of inhibitor: enzyme. Products formed during the inhibitory pathway must then be identified to determine how the CIU relative binding affinity data can compare. Several scans of native mass spectrometry were used to determine the onset of substrate binding and degradation products (and potentially a complete reversal to unbound TEM-1); every 10, 30, 60, 120 and 240-minutes mass spectra were recorded at both concentrations, taking the centroid mass. Below in figure 3.2, our results with the 10:1 inhibitor to enzyme ratio (magnified at the +21 charge state) are shown to demonstrate the sensitivity to binding that can be observed before 60 minutes have passed, unlike a single time point trial under pharmaceutical study[220].

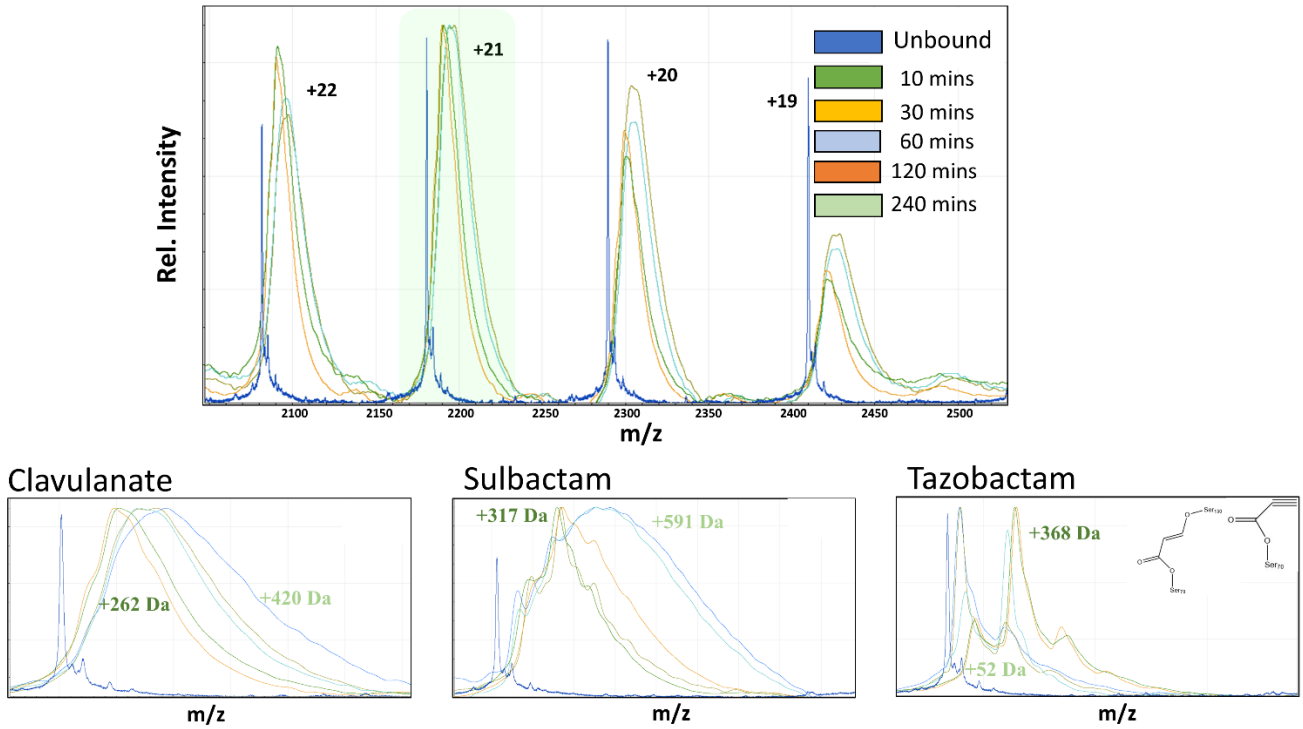

Figure 3.2 Native Mass Spectrometry Inhibitor Binding Study With 1000:1 Ratio Above) Native mass spectrometry of TEM-1 incubated with substrates over 5 time points. +21 charge state is highlighted in green for magnification below. TEM-1 incubation at 5 time points is displayed with the following colours: 10 mins (green), 30 mins (light orange), 60 mins (pale blue), 120 mins (dark orange) and 240 mins (light green). All experiments were run in triplicate and all drug substrates were incubated and mass spectra taken on the same day. Protein concentration was confirmed by BCA Assay prior to experimentation. In blue, the unbound +21 peak (at 2180 *m/z*) is highlighted. Bottom) Inset into the native spectra for each incubation are potential cross-linking inhibitor fragments associated with the mass increases listed.

To confirm byproducts intermediates were not overlooked prior to 10 minutes of incubation, scans were also recorded at 1,3,5,7 and 9 minutes with no additional binding observed (see Appendix B). It is apparent that with the larger inhibitor concentration of 1000:1 (figure 3.2), we see a large mass increase occurring by the time the first spectra (green line) is recorded at 10 minutes (clavulanate, +261 Da; sulbactam, +317 Da; tazobactam, +368 Da), of greater mass than the substrate alone. Both

clavulanate and tazobactam samples have a mass increase corresponding to a sodium or acetate adduct, respectively. The sulbactam spectra was consistently less resolved than the other two drugs- this is likely due to the weaker binding affinity and inability to form permanent acyl-enzyme products[202,215]. For the clavulanate and sulbactam samples this mass increases with time, likely due to multiple adduct formation. In contrast with sulbactam, the chemically similar tazobactam experiment records a mass shift associated with drug binding and an acetate adduct at 10 minutes, then changes to a lower mass product at 60 minutes which becomes the dominant product by 120 minutes. This byproduct seen after 60 mins of incubation (+52Da) has been postulated before as a propynyl chain, seen in figure 3.1, far left, bound to Ser70[220]. This lower mass byproduct is what we would expect from the inhibitor binding- as the drug is partially hydrolyzed, a fragment of the substrate remains in the drug pocket to inhibit further hydrolysis via the serine 70 residue[194,195,216]. To confirm the propynyl (Ser70) or cross-linked product (Ser70 and Ser130) associated with the +52Da increase, local HDX results will provide more insight.

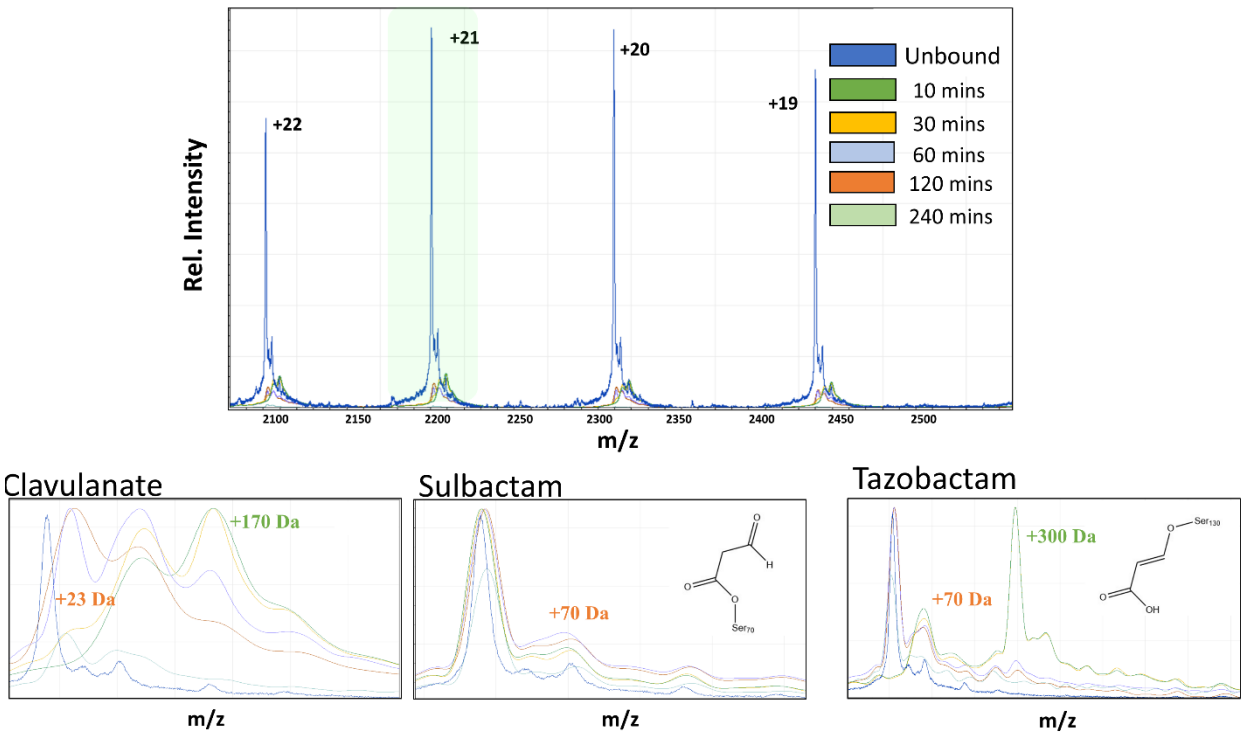

Figure 3.3 Native Mass Spectrometry Inhibitor Binding Study With 10:1 Ratio Above) Native mass spectrometry of TEM-1 incubated with substrates over 5 time points. +21 charge state is highlighted in green for magnification below. TEM-1 incubation at 5 time points is displayed with the following colours: 10 mins (green), 30 mins (light orange), 60 mins (pale blue), 120 mins (dark orange) and 240 mins (light green). All experiments were run in triplicate and all drug substrates were incubated and mass spectra taken on the same day. Protein concentration was confirmed by BCA Assay prior to experimentation. In blue, the unbound +21 peak (at 2180 *m/z*) is highlighted. Bottom) Inset into the native spectra for each incubation are potential cross-linking inhibitor fragments associated with the mass increases listed.

Results at the lower 10:1 ratio (figure 3.3) prove more interesting. At this much smaller ratio, clavulanate is not present to inhibit the complete population binding (+170Da), and instead has the addition of a sodium molecule within the binding pocket after 60 minutes (+22Da). Sulbactam and tazobactam behave more similarly on the hours timescale, which could be due to their similarly

sulfonated structures that has increased stabilization within the binding pocket. Sulbactam shows no evidence of binding until 120 minutes (+70Da), with tazobactam showing complete binding at 10 minutes and reversion to the same byproduct (+70Da) as sulbactam after 120 minutes. Others have previously reported on an adduct of +40Da forming with both sulbactam and tazobactam in a class C β-lactamase[228], suggesting very similar mechanistic pathways in all serine-catalyzed β-lactamases inhibited by sulfones. The similar binding product mass at 120 minutes discovered in both sulfonated substrate experiments suggests the same mass byproduct formation, likely being the +70Da product of an aldehyde byproduct covalently linked to Ser70 discovered in previous work[220,229]. Although the byproducts are the same mass, they may operate through two different mechanistic pathways because of their residues involved: the substrate product forming slowly after two hours (with sulbactam incubation) is most likely permanent inactivation, binding to Ser70. The tazobactam product of +70Da may also be part of an irreversible inactivation pathway, but potentially binding to the other important serine residue, Ser130[138,227]. Further analysis at the peptide level for binding will provide conclusive binding results.

3.3.2 Local HDX Coverage of TEM-1 β-lactamase

To help visualize the regions of the protein involved in long-term inhibition, local HDX was carried out in biological replicate at several time points. Based on the binding affinity results described above, we continued the study with a 10-minute incubation time for the 1000:1 ratio which should give complete residue information after TEM-1 has become inhibited with all substrates.

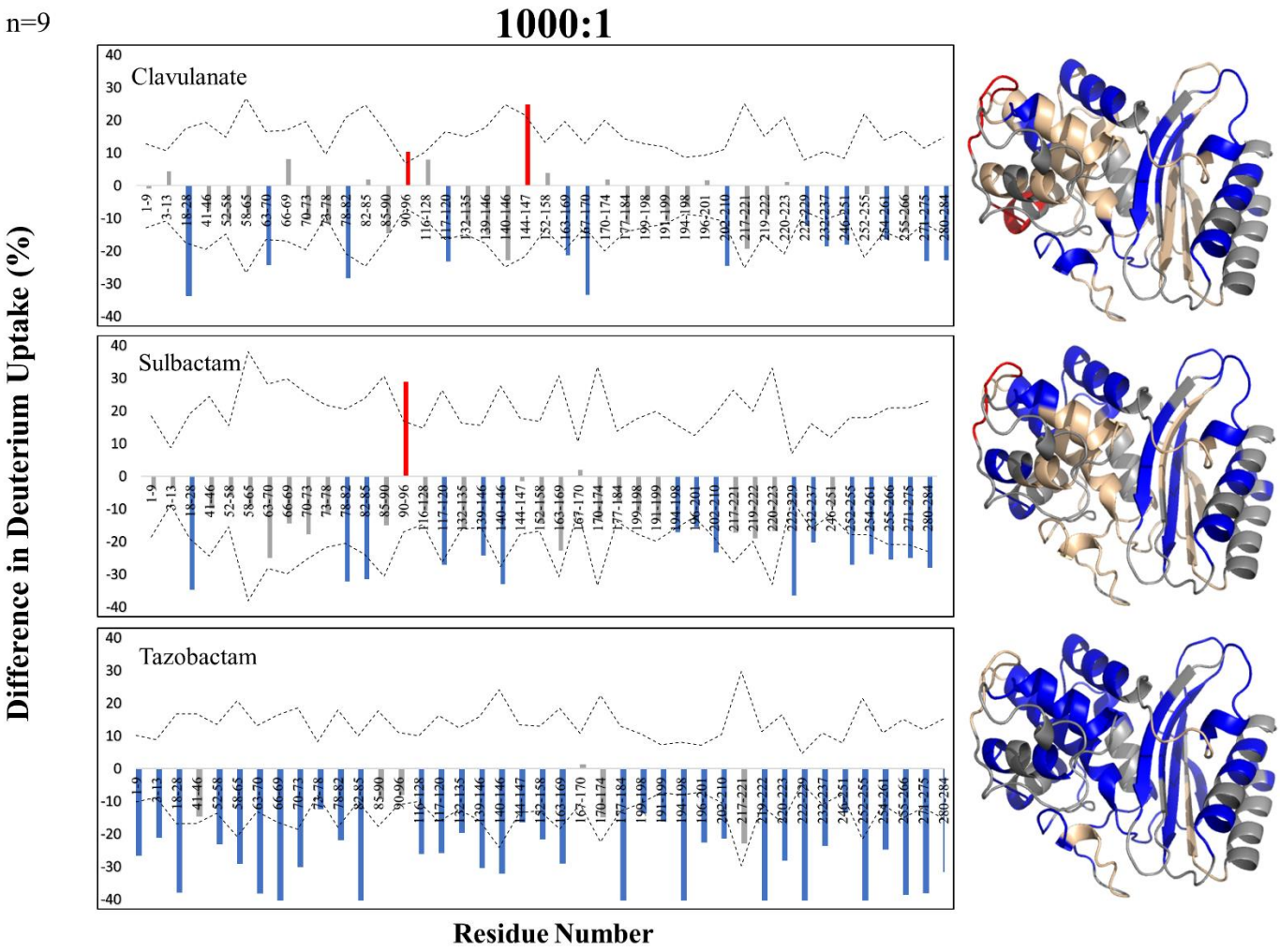

Figure 3.4 Local Deuterium Uptake Results for Equilibrated HDX-MS with Inhibitors in 1000:1 Inhibitor: Enzyme Ratio. Left: Difference in deuterium uptake between TEM-1 and incubated TEM-1 with substrate is displayed for the 1000:1 inhibitor: enzyme ratio. Peptide fragments in colour (blue, decreasing; red, increasing; grey, no change) signify differences in deuterium uptake between the holo and apo enzyme forms (>2σ, dotted black line). Right: Pymol image (PBD ID: 1BTL) displays the significant changes in dynamics for all substrates (top, clavulanate; middle, sulbactam; bottom, tazobactam). Regions on the structure with no significant change are displayed in gold, increasing in red, decreasing in blue and unrecorded regions are in grey.

Unsurprisingly with the 1000:1 inhibitor incubation, the deuterium uptake was reduced upon mixing with the inhibitors relative to the unbound protein sample (figure 3.4), suggesting a rigidification of

the overall structure that is common with inhibiting products. The tazobactam-incubated sample provided the most consistent decrease in conformational dynamics both sequentially and spatially, with the inner β-sheets (responsible for stability through salt bridges and covalent bonding within the binding site[113,124,203]) and binding region (residues 70-73) showing uniform rigidification. The sulbactam-incubated sample had a high degree of flexibility, providing a limited amount of significant changes in deuterium uptake. However, there is a consistent pattern of rigidification in H11 (residues 270-284) across all samples that we postulated before is necessary for complete enzyme inactivation[55]. The clavulanate sample has one unique region with increased dynamics (residues 144-147) that has not been previously described as important for catalytic binding or as a potential for mutagenesis[201], but otherwise has similar rigidification patterns to sulbactam and clavulanate.

In stark contrast with the consistent rigidification and inhibition results displayed in figure 3.4, the lower ratio of 10:1 inhibitor: enzyme was too little substrate to completely initiate the inactivation pathway in TEM-1 (on average) within this time frame. With a longer timescale of 120 mins incubation of the 10:1 inhibitor: enzyme samples, protein was not soluble enough to carry out local HDX workflow without extensive aggregation (likely due to the inactivated protein).

3.3.3 Comparison of Inhibitor Binding Affinity by Collision Induced Unfolding -Mass Spectrometry

Collision-induced unfolding (CIU) with intact protein/substrate complexes can supplement local HDX analysis of peptides that has difficulties with a large error range based on artificial deflation of deuterium uptake generated by peptide bombardment in the collision cell[230]. We can also observe changes in stability upon inhibitor binding based on the unfolding map provided[40,45]. To utilize CIU in

conjunction with HDX, we analyze TEM-1 as an intact protein (for binding and unfolding studies) and through bottom-up proteomics (for HDX of peptides). A detailed representation of the workflow is displayed in figure 3.5.

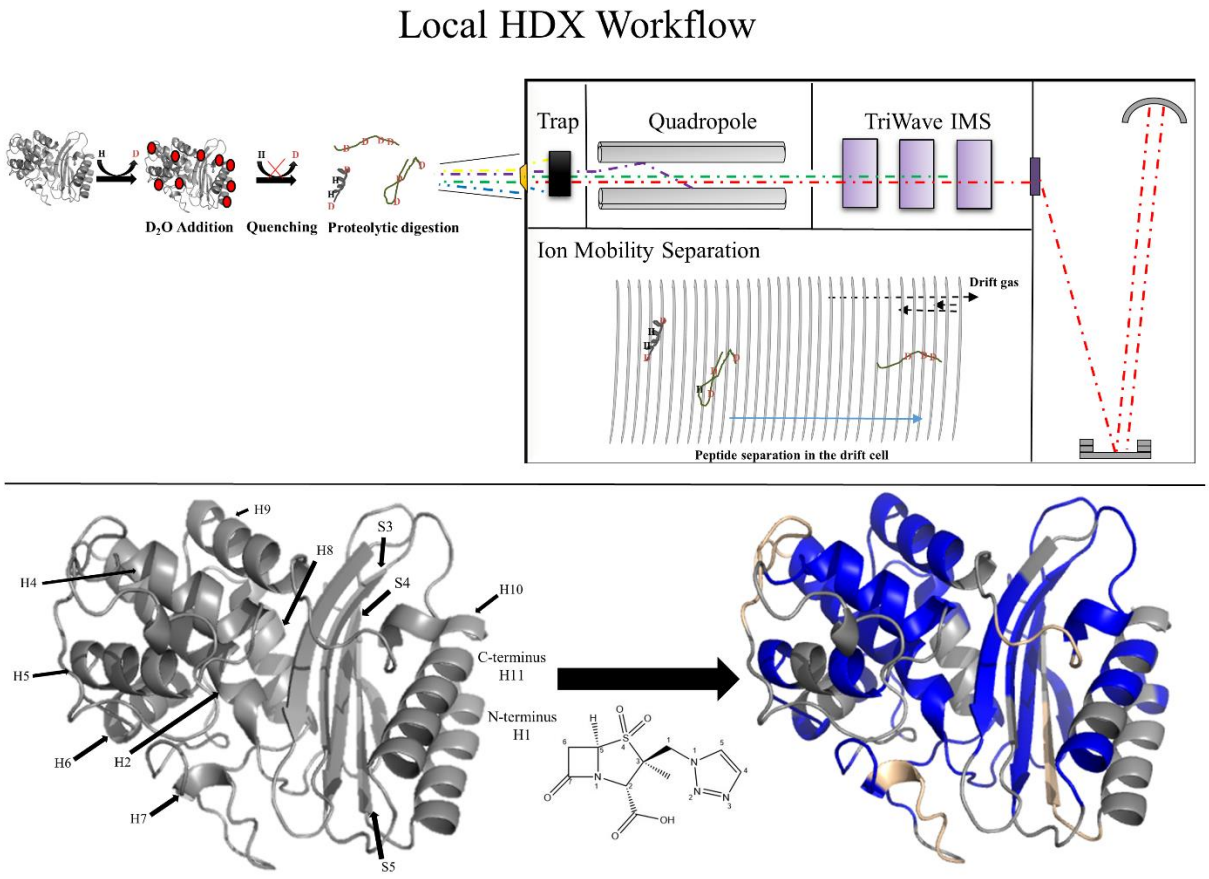

Figure 3.5 Local HDX Workflow for TRESI-HDX and IMS-MS Experiments. Top) For our bottom-up proteomics (TRESI HDX-MS), protein and deuterium capillaries react at a fixed distance (measured by pulling out the inner capillary) before the reaction is quenched by acetic acid (pH 2.4). The deuterated sample is then digested within a PMMA chip by protease XVIII and pepsin. With IMS-enabled experiments, the TriWave component of the Synapt separates the sample (whole proteins for CIU studies, peptides for HDX) by collisional cross section (CCS) based on drift time. Bottom) The crystal structure of TEM-1 (PBD ID: 1BTL) is shown on the left with secondary structure noted. On the right, the HDX results for TEM-1 reacted with Tazobactam are displayed. Blue regions indicate a decrease in dynamics, grey is no coverage and gold indicated no change (with respect to the unbound protein sample).

To determine the initial ramping and binding conditions, several rounds of optimization were performed. Complete binding and formation of the acyl-enzyme was uniformly observed after 10 minutes of incubation with the 1000:1 ratio, but all substrates demonstrated differing binding activities after 30 minutes, so all results for binding affinity were recorded within this timeframe. The 10:1 ratio experiment were also recorded after 10 minutes to determine if there was binding activity observed that was not observed by native mass spectrometry. A travelling-wave velocity of 400 m/s produced the best resolution of bound protein without causing pre-fragmentation of the samples.

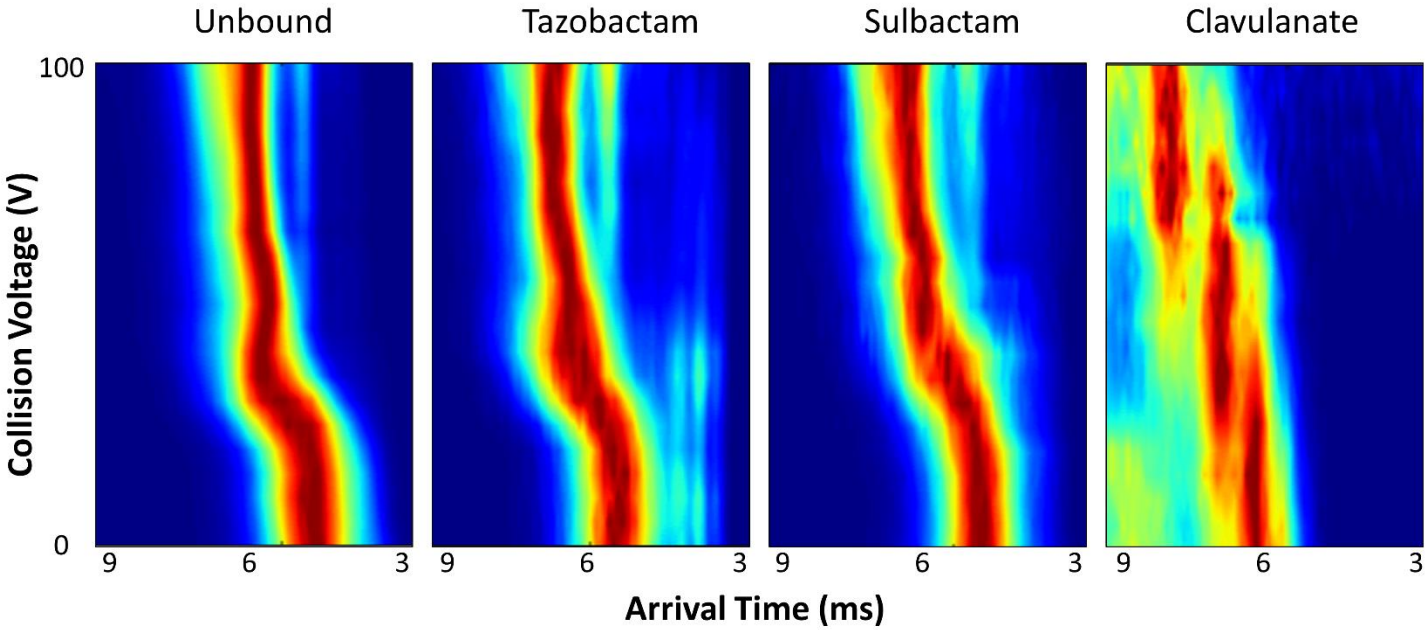

Figure 3.6 CIU Heat Maps of Binding Affinity for TEM-1 and Inhibitors with a 1000:1 Ratio of Inhibitor to TEM-1. CIU spectra of inhibitor-bound TEM-1 for the 1000:1 experiment at collisional voltages from 0-100 V, taken in 5V increments. All spectra were recorded for the +16-charge state.

Upon initial inspection of the results in figure 3.6, it is apparent that the clavulanate sample at the 1000:1 ratio produces the most distinct transitions between folding states and completes the final

(third) transition to a more unfolded conformation at the highest collisional energy (~70 V). Tazobactam and sulbactam samples both unfold at nearly identical rates to each other and to the unbound TEM-1, with two transitions occurring below 50 V. Having the clavam inhibitor produce unique results with higher binding affinity can be explained structurally; the lack of a sulfone leaving group on the five-membered ring means the compound is not easily protonated for the ring opening, leading to the subsequent β-elimination occurring at a higher binding energy[195,215]. Surprisingly, the clavulanate-bound sample is also much more destabilizing, as noted by the higher arrival times. This suggests that the sulfonated byproducts force the protein into a more compact form, regardless of the additional molecular weight associated with the sulfone group and the presence of the triazole component of tazobactam.

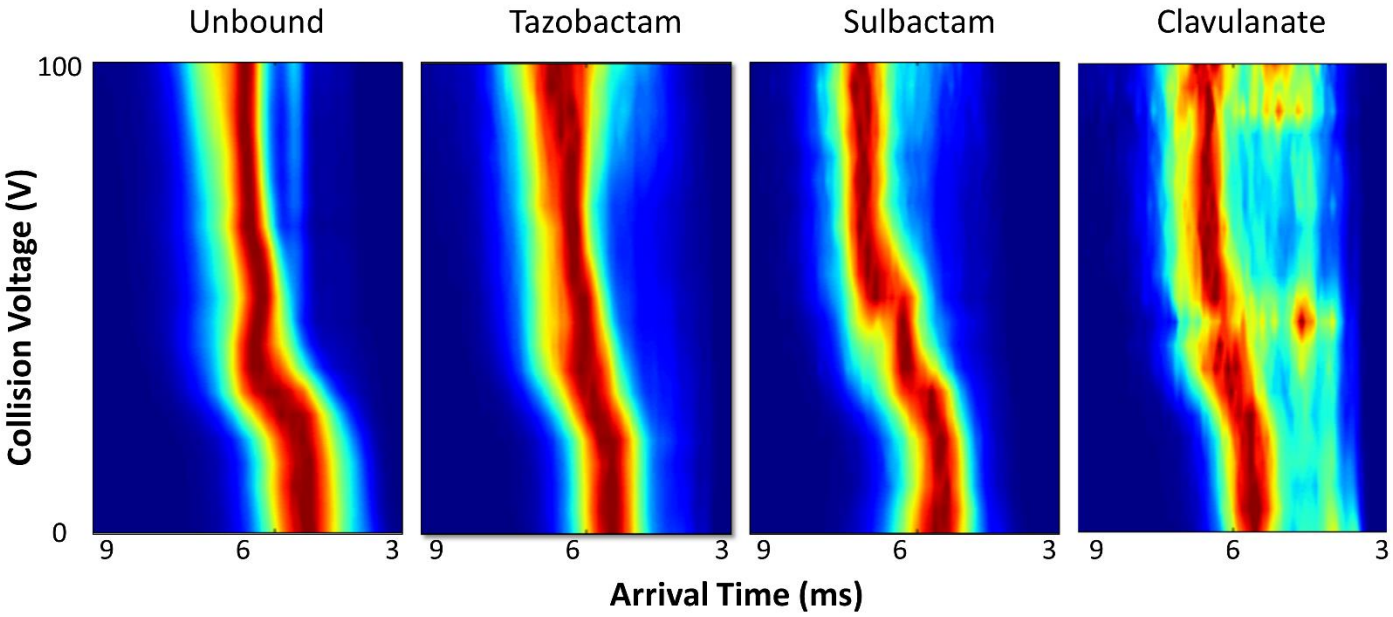

Figure 3.7 CIU Heat Maps of Binding Affinity for TEM-1 and Inhibitors with a 10:1 Ratio of Inhibitor to TEM-1. CIU spectra of inhibitor-bound TEM-1 for the 10:1 experiment at collisional voltages from 0-100 V, taken in 5V increments. All spectra were recorded for the +16-charge state.

For the 10:1 CIU spectra shown in figure 3.7, the similarity between incubated samples and unbound TEM-1 suggest a lack of binding. For all 3 inhibitor spectra, there is a similar unfolding pattern, with 2 conformational changes occurring before 50 V. What is most interesting about these results are the lack of a third unfolding state in the first 50 V as observed with the unbound protein, suggesting that the presence of a minute amount of inhibitor in solution may slightly stabilize the encompassing protein sample.

3.4 Discussion

It is difficult to draw conclusive statements regarding the potency of each inhibitor under study without a degree of caution. Although the CIU results would suggest that clavulanate provides the tightest binding affinity with a ratio of 1000:1, there are fewer regions of increased rigidity in TEM-1 upon binding in our HDX results when compared to tazobactam. Tazobactam-bound TEM-1 provides the most "locked in" conformation, but mass shift results from native binding studies have conclusively demonstrated binding of all substrates at the higher molar ratio, so this binding behavior is not unique to tazobactam. Perhaps having fewer regions of rigidification with clavulanate-HDX instead brings to light the regions that are in fact the most important for binding; the conserved binding site (residues 70-73), two inner β-sheets (residues 220-251), the Ω-loop (residues 161-179) and α-helix H11 (residues 270-284) are the only regions that are significantly rigidified upon clavulanate binding, in agreement with the current understanding of substrate binding to Class A β -lactmases[203,231–233]. The additional rigidification noted in the tazobactam sample could be allosteric effects induced post binding, as they are not present in the uptake on the ms-timescale. Although sulbactam and tazobactam display near-identical collisional unfolding results at the 1000:1 and 10:1

ratios, the HDX results show limited changes in dynamics relative to unbound protein at the binding site and Ω-loop for the sulbactam sample on the short timescale, likely due to sulbactam's weak binding affinity.

Questions pertaining to binding affinity may be better answered by discussing the observed mass shifts. In both binding studies, the final +52Da (1000:1) and +70Da (10:1) products produced by the tazobactam incubation are likely bound to a serine residue. However, for the tazobactam experiments, Ser70 was bound in the 1000:1 experiment while Ser130 was bound in the 10:1 study. This +52Da sample was likely the final inhibitory byproduct formed by tazobactam in high saturating conditions, while +70Da connection to Ser130 is more prevalent at low dosage. With the larger inhibitory ratio, clavulanate and sulbactam exist in an acyl-enzyme form without generating an inhibiting fragment to permanently block the active site. Sulbactam has never been noted to exhibit slow-onset inhibition[229], and this is especially unexpected at a low inhibitory ratio. Yet in the 10:1 study, there is the formation of an intermediate that is postulated to bind at the Ser130 residue responsible for drug deacylation, causing a permanent inactivation of TEM-1 in the binding pocket. By recording native scans at such large time intervals, we did not believe it would be possible to observe mechanistic differences in the permanent vs transient inactivation pathways.

3.5 Conclusions

Using different inhibitory ratios provided an opportunity to observe changes in the mechanistic pathway of the inactivation of TEM-1 by several inhibitors, such as the production of two different inactivation byproducts with tazobactam incubation at different concentrations, and the production

of an inhibited enzyme by low concentration of sulbactam incubation. Using CIU in conjunction with HDX-MS provides a comprehensive toolset for analysis of drug substrates to determine optimal binding concentrations ideal substrates for a multitude of drug targets. Further work on drug binding needs to be done with native MS, as most clinical work employs much lower ratios of drug substrates and incubates for shorter time periods before testing occurs, losing critical information about the catalytic pathway.

3.6 Methods

3.6.1 Collision Induced Unfolding Mass Spectrometry of TEM-1 with Inhibitor Substrates

Trap cone voltage was ramped from 0-100V in 5 V increments on a Waters Synapt G2S with a travelling-wave IMS-enabled cell. Scans were recorded in 3-minute increments. TriWave voltage remained constant at 400 m/s. Unbound and substrate-incubated samples were scanned on the same day after 10 minutes of incubation. Pulsar software was used to analyze and integrate each unfolding plot as a function of arrival time vs. collision energy. The same charge state (+16) was selected for each sample and results were recorded in biological replicate.

3.6.2 Native Mass Spectrometry of Inhibitor Binding

Protein was prepared and buffer exchanged as previously described in print[55] and in section 2.5.1. Protein concentration was determined by Bradford assay and diluted to a range of 30µM-150µM prior to incubation with substrate in either a 10:1 or 1000:1 molar ratio based on ratios previously used in pharmaceutical trials that exhibited complete inhibition[220,227]. Substrates were dissolved in 200mM ammonium acetate (to match buffer conditions of the protein). Experiments were repeated in

technical and biological triplicate to verify results. Images were prepared using mMass[234] and Sigma Plot.

3.6.3 Data Analysis of Global and Local HDX

All HDX work was carried out in biological replicate with a source condition of 2700V capillary voltage and 100V sampling cone in positive ion mode. Experiments were performed using the nanoESI source on a Synapt G2 Q-Tof instrument with IMS-enabled workflow throughout. Mass spectrometry deuterium analysis was performed by Mass Spec Studio[235]. Peptide fragments were confirmed by MS/MS. mMass and MassLynx were used to visualize the native protein spectrum and mass shifts with substrate incubation.

Chapter 4

Monitoring Catalysis and Associated Conformational Effects in Yeast Alcohol Dehydrogenase by Millisecond-Scale HDX Mass Spectrometry

A version of this chapter has been prepared in manuscript format.

4.1 Summary

Hydrogen/deuterium exchange is one of the few analytical techniques that can capture transient intermediates for enzymatic systems. By combining global and local HDX workflows, we aim to discover regions essential for catalysis that are traditionally inaccessible by techniques such as NMR or X-ray crystallography. Having previously established the presence of a kinetic isotope effect in the yeast alcohol dehydrogenase (YADH) oxidation of ethanol by substitution with 1,1-D_2 ethanol [85], we aimed to identify the dynamics of intermediates on the slower timescale provided by the deuterated substrate. Using a time-resolved microfluidics device to capture deuterium uptake on the millisecond timescale allowed us to observe the rigidifying effect of NAD^+ binding within the binding pocket and the catalytic zinc to facilitate the required hydride transfer between NAD^+ and ethanol. Within the same timeframe, we isolated a region (residues 259-268) that was found to have a significant decrease in dynamics due to the deuterated substrate, suggesting a link between the rigidification near the core and a requirement for increased flexibility in the outer regions to relieve the steric strain caused by catalysis.

4.2 Introduction

Decades of research has been geared towards the challenging task of observing protein dynamics while they facilitate enzymatic reactions with incredible speed and efficiency. Making structural arguments about protein function during a catalytic timescale has proven immensely difficult. It is postulated that amide bond fluctuations (on the ps-ns timescale) influence global dynamics[236], and many kinetic studies have proven the turnover rate of enzymes on the ms-s timescale, making techniques such as NMR and conventional HDX unable to provide definitive arguments

to the behaviour of enzymes during catalysis. For identifying structural regions of importance, CPMG relaxation and X-ray crystallography can help with the identification of binding regions, but not necessarily with the transient intermediates or isotopic effects that occur during turnover. Alcohol dehydrogenases (ADHs), responsible for the redox reaction between alcohols and aldehydes to energy transport molecules (NADH and $FADH_2$)[155] are found in a variety of forms in nature, most commonly in dimeric form (higher eukaryotes) and tetrameric (prokaryotes and lower eukaryotes)[165]. Although there are a wide variety of ADHs, many published studies have examined horse liver ADH (HLADH) due to the early publication of its crystal structure[171]. Horse liver is an ADH sequentially similar to yeast ADH, except for a deletion of 21 residues within the catalytic region (residues 1-175, 319-374) and a dimeric form[165,167,237]. Characterization of yeast alcohol dehydrogenase (YADH) provides a greater challenge when attempting to observe the dynamic nature of the protein during catalysis: it is twice as large as HLADH, has higher substrate specificity for alcohols[237] and is 100x more active[238].

Yeast produces 3 isozymes of ADH; ADH1 and ADH2 are produced in the cytoplasm (and repressed by high glucose levels), while ADH3 is found in the mitochondria and expressed in much smaller quantities[239–241]. It was originally thought that ADH1 and ADH2 were separately involved in the oxidation pathway, with ADH1 carrying out the reduction of NAD^+ and ADH2 performing the opposing oxidation of NADH[166]. This theory has been disproven and now it is widely understood that the catalysis occurs through a bi-bi sequential mechanism[175,181], with both ADH1 and ADH2 capable of carrying out the reversible redox reaction. Herein we experiment with the ADH1 isozyme to distinguish the role that a reduction in conformational

dynamics (due to the kinetic isotope effect of D_2-EtOH) will have in isolating specific regions in YADH that are necessary for hydride transfer during catalysis.

4.3 Results

Catalysis by YADH has multiple components which makes its characterization difficult in isolation: zinc atoms are necessary for catalysis and structural support, NAD^+/NADH as a coenzyme, and alcohol/aldehyde for the hydride transfer to occur. Each monomer of YADH contains 2 zinc atoms, with different functions: 1 zinc atom is necessary for catalysis (facilitating the alcohol docking)[242], while the other zinc atom is responsible for maintaining structural integrity[243]. The distal (structural) zinc is coordinated to 4 cysteine residues (Cys97, Cys100, Cys103 and Cys111, figure 4.1)[168,242,244,245]. The catalytic zinc binds Cys46, His67 and Cys174 to maintain a strained conformation within the active site of the open dimer, along with polarizing the carbonyl of the incoming alcohol substrate to assist the hydride transfer[246–251].

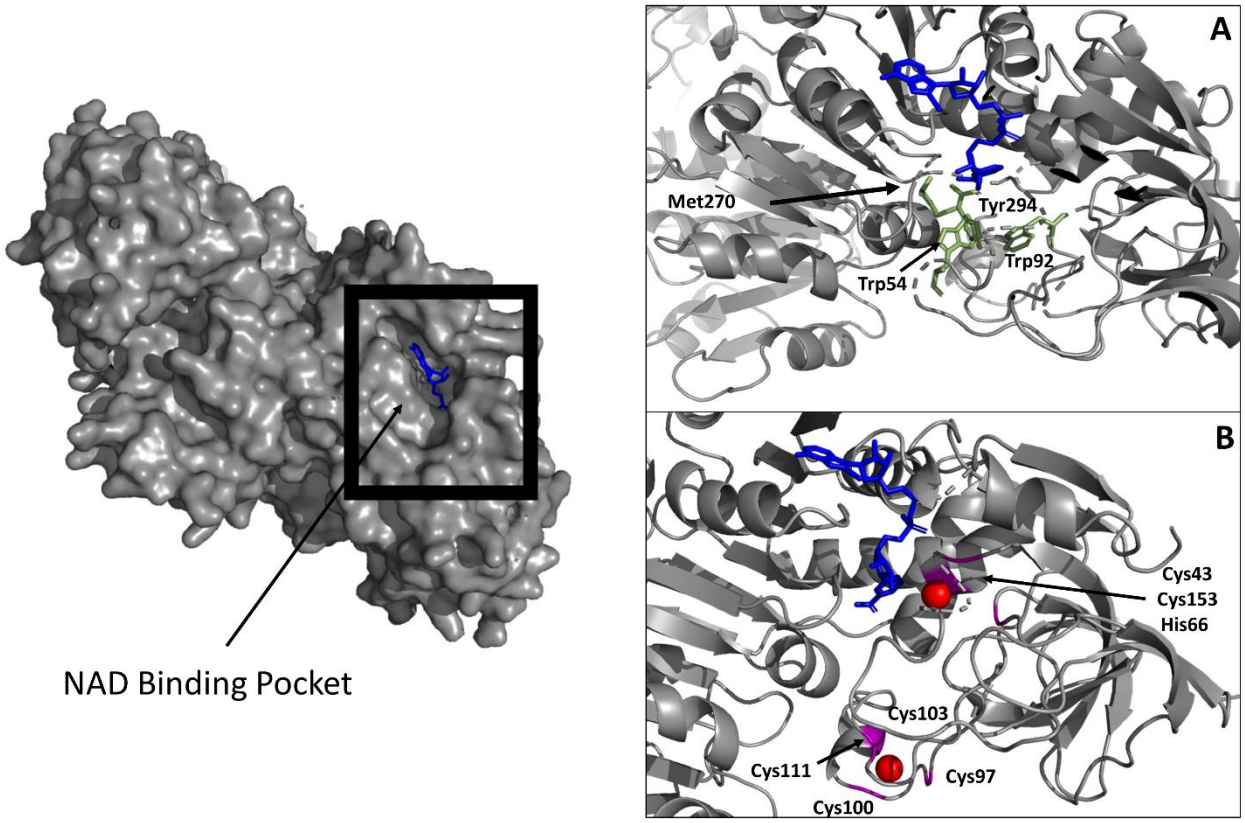

Figure 4.1 Schematic of Residues of Interest in Reduction of NAD^+ to NADH Although YADH operates as a homotetramer, within each dimer there are both open and closed forms. This schematic is showing the open conformation of the binding pocket observed in the dimer, with NAD^+ (blue) bound. Catalytic zinc for the open conformation is in an inverted position, with binding to different cysteine residues (Cys43, Cys153)[247]. A) NAD^+ bound with the hydrophobic regions (green) highlighted. B) NAD^+ bound with zinc atoms (red) coordinated and cysteine residues (purple) highlighted.

NAD^+ binds within the βαβ-fold of the interdomain cleft[163,252], nearby to the hydrophobic binding site pocket (containing Trp54, Trp92, Met270, Tyr294, figure 4.1). The face of the NAD^+ ring is positioned towards the active site, very close to the Cys46 and Cys174 that coordinate with the catalytic zinc in the closed conformation of the homotetramer[239]. In addition to the

hydrophobicity, an accumulation of negative charges (residues Cys46, Lys174, Glu68, Asp49) helps generating a dipole moment to help with the hydride transfer to NAD^{+}[253]. Another important residue for this catalytic mechanism is Val203, well-documented as being important for facilitating the hydride transfer between NAD^{+} and ethanol; the large size and hydrophobicity of this residue is opposing NAD^{+} and aids in the narrowing of the interdomain cleft[164] that promotes tunneling behaviour[173,179,245,254].

Kinetically, the oxidation of NADH (and correspondingly the reduction of acetaldehyde to ethanol) is the favoured reaction in this reversible redox pathway[255,256]. By introducing the substrate after the NAD^{+} cofactor is bound, we force the reaction to occur in the NADH-favoured direction. By using ethanol as the catalytic substrate, we aim to develop a baseline for the highest potential difference in dynamics observable by HDX, as ethanol is the most active substrate with YADH and most dehydrogenases[246,257].

4.3.1 Optimization of the Oligomeric YADH

Although the catalytically competent form of YADH is the homotetramer[43,243], it is difficult to observe this macromolecular assembly by mass spectrometry. Even employing ESI-MS as a soft ionization technique for generating spectra of the native protein, separation of dimers and tetramers is possible in the gaseous phase with minimal energy applied. Without extensive optimization of ionization conditions, YADH is observed primarily in monomeric form (figure 4.2, top), with some smaller populations of dimer and tetramer.

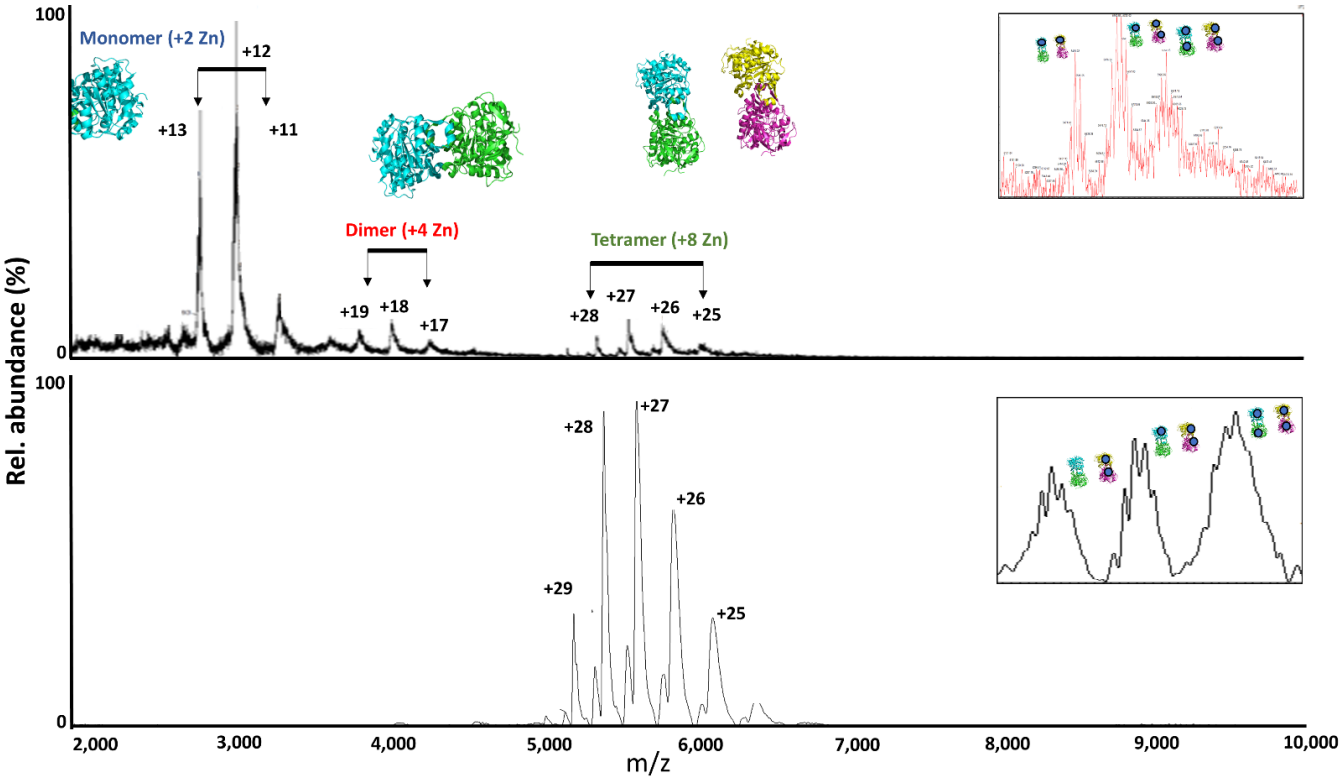

Figure 4.2 Optimization of Oligomeric Forms of Yeast Alcohol Dehydrogenase Top) Raw native mass spectra for YADH, with monomeric, dimeric and tetrameric forms labelled. Inset (top right) is the native spectra of the same sample with NAD^+ incubation, with number of NAD^+ molecules bound to YADH highlights as blue dots on the crystal structure (PDB ID: 5ENV in dimeric form, 4W6Z in tetrameric form). Bottom) Same YADH sample with optimization of the ionization parameters to obtain only tetrameric form. Inset (top right) is the NAD^+ bound complex, with the tetrameric NAD^+ occupancy being favoured.

It is apparent in figure 4.2 that the complete NAD^+ occupancy is not favoured under the initial conditions shown in the top of figure 4.2. Backing pressure was increased on the Synapt G1 to reduce the speed at which the high mass homotetramer was travelling through the ToF, slowing down the free path enough to allow the detector within the instrument to detect the oligomeric form that is observed in the biological environment- the homotetramer, composed of 4 units of

identical monomer[42,258]. After optimization, tetrameric YADH appears in the charge state region of 20-27 as reported previously, with 2 zinc ions bound per monomer[43,259]. We also observe an increase in apo-enzyme bound-NAD^+ (figure 4.2, bottom inset), showing a favouring of complete NAD^+ occupancy with the homotetramer. The experiment was optimized to determine the minimum timeframe necessary to have complete (or near complete) NAD^+ binding. In brief, an effective concentration of 400 µM of NAD^+ was added to the YADH solution (10 µM starting concentration) and incubated for 15 minutes prior to acquiring the mass spectra. These instruments conditions were maintained throughout subsequent experiments with HDX, with native mass spectra of the homotetramer recorded prior to beginning any HDX experiments.

4.3.2 Global HDX of YADH Catalysis

Hydrogen/deuterium exchange experiments studying dynamics of ADHs have been performed in the traditional fashion of a s-hrs timescale, but never local and global HDX experiments combined for this type of enzyme[172]. Experiments studying the KIE of ADHs have been of particular interest due to the quantum mechanical nature of ADHs; with deuterated substrate and increased temperatures, enhanced tunneling to carry out the hydride transfer has been noted, especially with yeast ADH[164,171,180,260,261]. Using an excess of coenzyme (40:1 molar ratio of NAD^+ to YADH) we were able to demonstrate NAD^+ occupancy (described fully in section 4.6.1) prior to the deuteration event without the NADH signal overpowering the protein ionization at 666 *m/z*. Given the concentration of NAD^+ used and our experimental TRESI workflow a k_{cat} of 380 s^{-1} was established for HDX experiments using YADH[85]. We recorded deuterium uptake with several time points before and after turnover and hydride transfer is expected to occur.

As observed in figure 4.2, there are a couple of different occupancy possibilities for the tetrameric form of YADH, $(NAD^+)_2$ and $(NAD^+)_4$ being the two major forms. Although previous research has described the full $(NAD^+)_4$ occupancy as being the most common distribution when catalytically active[85], we wanted to determine if ethanol would be able to be oxidized as efficiently regardless of NAD^+ occupancy using our millisecond-scale ESI workflow.

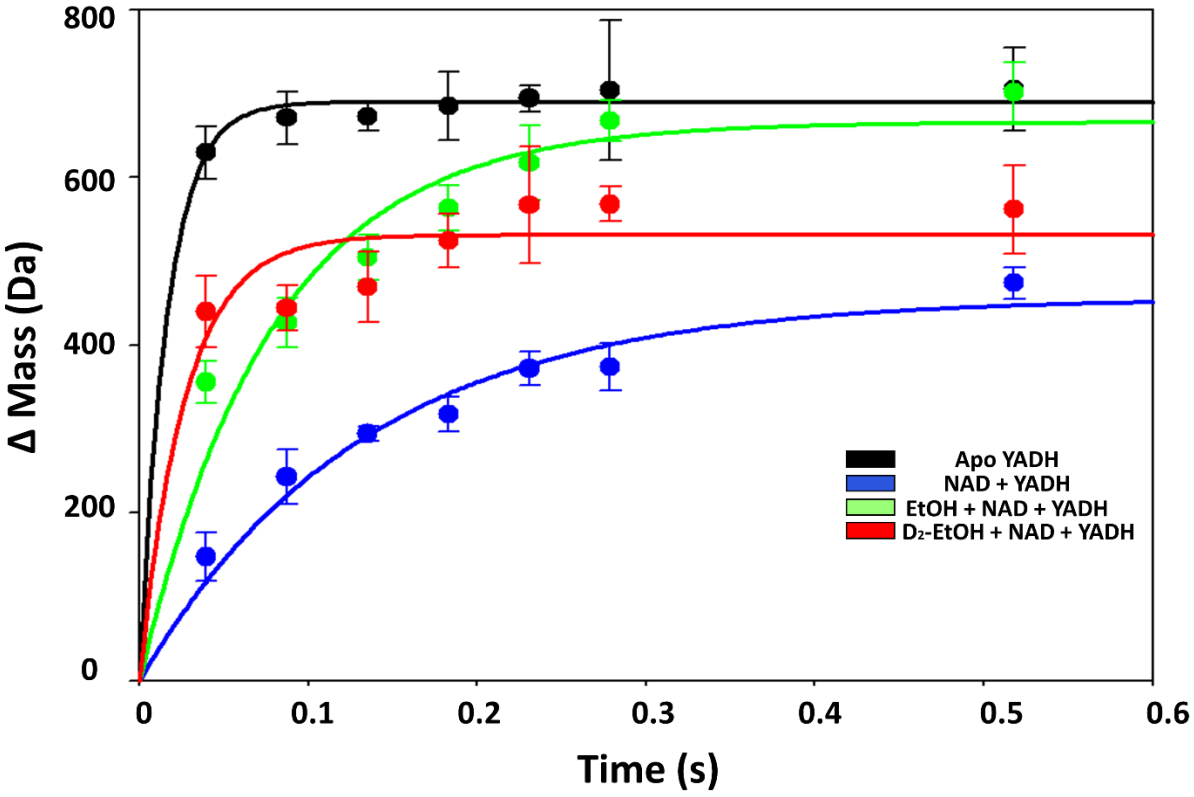

Figure 4.3 Global HDX results for $(NAD^+)_2$ occupied YADH. Global HDX mass increases were captured on the same timescale as local HDX results in triplicate. Apo enzyme (black) has both the largest increase in dynamics and most rapid onset, while holoenzyme (blue) displays the opposite. In between, D_2-EtOH catalysis (red) has a slightly larger amplitude of dynamic increase than EtOH catalysis (green) during catalysis, with lower dynamics as the reaction goes to completion.

With partially occupied tetramer, all 4 experimental runs displayed significantly different uptake and dynamics during the catalysis timeframe, with the D_2-EtOH sample having the largest catalytic amplitude of dynamics. However, the D_2-EtOH sample reaches a plateau of approx. 500 Da after 200 ms, a much smaller increase in deuterium uptake when compared to the non-deuterated sample at the same time point. In comparison, the EtOH-catalysis sample had slower dynamics during catalysis than the D_2-EtOH sample, however it behaved similarly to the apo-enzyme in the timeframe after the turnover event had occurred. The holo-enzyme form has a maximum mass increase of 474±18.4 Da, much lower than the apo-enzyme with 705±49.6 Da.

From the same experiments, the mass increases corresponding to the deuteration of the $(NAD^+)_4$ tetramer were also recorded and provided somewhat different results.

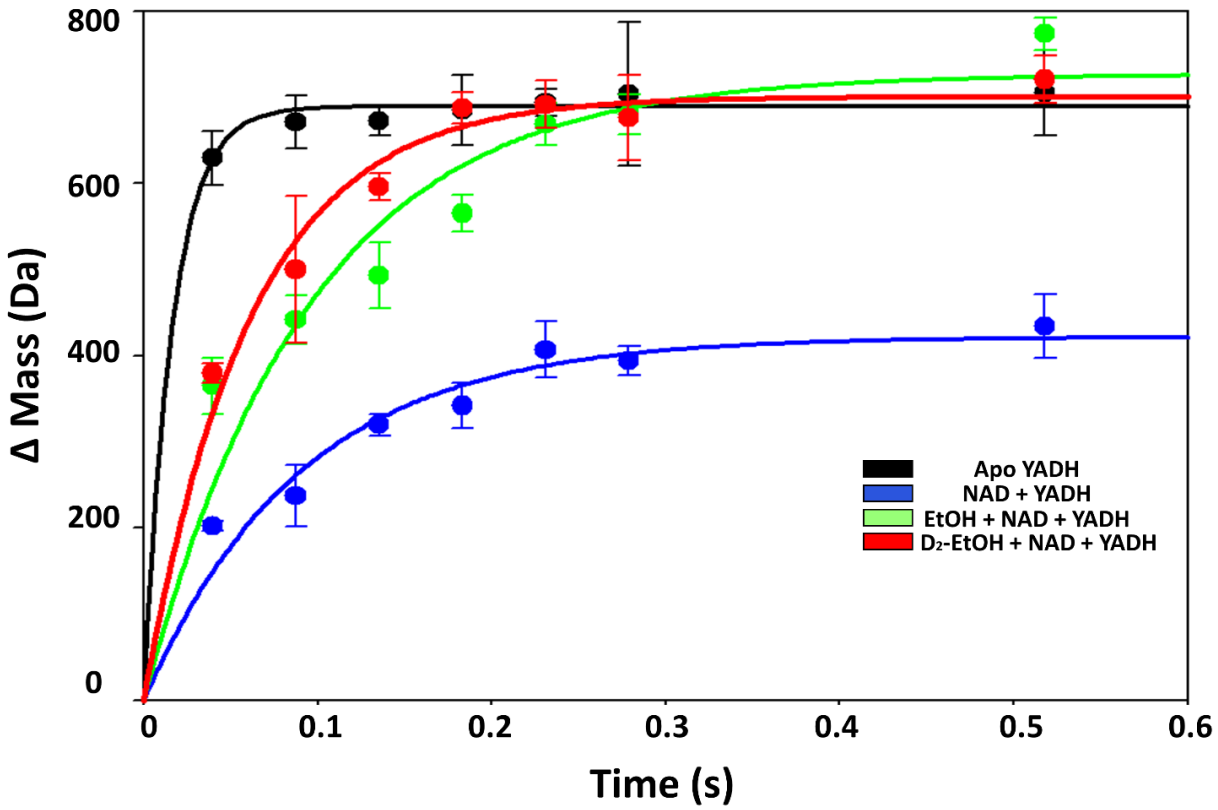

Figure 4.4 Global HDX Results for YADH with $(NAD^+)_4$ occupancy during catalysis. Global HDX mass increases were captured on the same timescale as local HDX results in triplicate. Apo enzyme (black) has both the largest increase in dynamics and most rapid onset, while holoenzyme (blue) displays the opposite. In between, D_2-EtOH catalysis (red) has a much larger amplitude of increase in dynamics than EtOH catalysis (green), while having similar dynamics in the lag phase of catalysis.

Once again in figure 4.4, we see a rigidification of the holo-enzyme with NAD^+ occupying the hydrophobic binding pocket, plateauing with a mass increase of 433±36.8 Da, a similar value compared to the $(NAD^+)_2$ sample. The catalytic samples behave much more similarly with complete $(NAD^+)_4$ occupancy, with limited significant results demonstrated between the EtOH and D_2-EtOH samples in this timeframe. These results are in line with previous research carried out by our group[178] and lead us to a further exploration of the local HDX dynamics to determine

if more localized information on the conformational dynamics would lead to residue-specific identification of regions involved in the formation of transient intermediates.

By comparing the difference in local deuterium uptake relative to the holo-enzyme form, it allows us to negate the effect of the rigidification due to the docking of the molecule NAD^+ and focus on changes in protein dynamics relevant to the addition of deuterated and non-deuterated ethanol for catalysis. Experimental conditions were kept identical to the global HDX experiments, with the addition of an acidic quenching step and proteolytic digestion chamber (see section 4.6.2).

4.3.3 Local HDX of YADH Catalysis

Using our microfluidics workflow that enables hydrogen/deuterium exchange on the millisecond timescale allows us to monitor protein dynamics as catalysis is occurring[85,199,223]. As we have already determined the kinetic isotope effect of D_2-EtOH in YADH catalysis, we now seek to demonstrate on a localized level how this influences the dynamic nature of the protein.

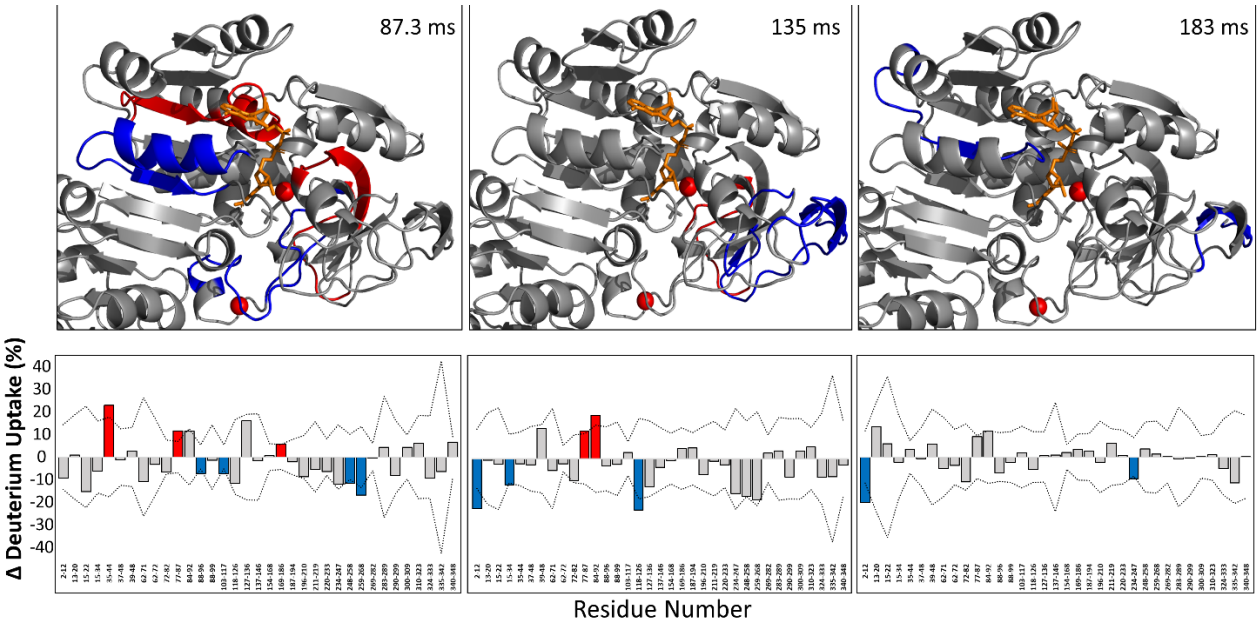

Figure 4.5 Single Time Point Local HDX Results for EtOH Catalysis Top) Mapped results of the local HDX deuterium uptake for 3 time points (87, 135 and 183 ms) during catalysis in one monomer, with dynamics > 2σ mapped to the crystal structure (red is increasing dynamics, blue is decreasing dynamics). Bottom) Local HDX results prior to NAD^+ turnover with peptide-level changes in deuterium uptake. Regions of colour indicate statistically significant results (> 2σ). The black line outlines the 2σ confidence interval, n=9.

The 3 timepoints examined in figure 4.5 above fall within the timescale of hydride transfer occurring. Of note are the regions that are displayed in colour (red is an increase in deuterium uptake relative to the holo-enzyme, blue is a decrease in uptake) that have been discovered as statistically significant in biological replicate. Regions around the catalytic zinc atom (red sphere, centre) have increased dynamics in the first 2 images, with the structural zin (red sphere, bottom) having opposing dynamics. Figure 4.5 gives a good example of the difficulties with using millisecond-scale HDX for identifying regions of catalysis- often the residues that are isolated as being statistically significant relative to the holo-enzyme results (>2σ) are not dynamics seen

consistently throughout the catalysis process. For example, there has been much debate over the properties of the zinc coordination for catalysis: it is well-established that is necessary for catalysis[242], but it may either be involved in facilitating deprotonation of ethanol for oxidation[246,247] (which would cause an increase in dynamics as coordination to cysteine residues is disrupted with the incoming ethanol) or in generating a fixed strained conformation necessary through coordination to several residues for stability during catalysis (which would cause a rigidification and decrease in dynamics)[248].

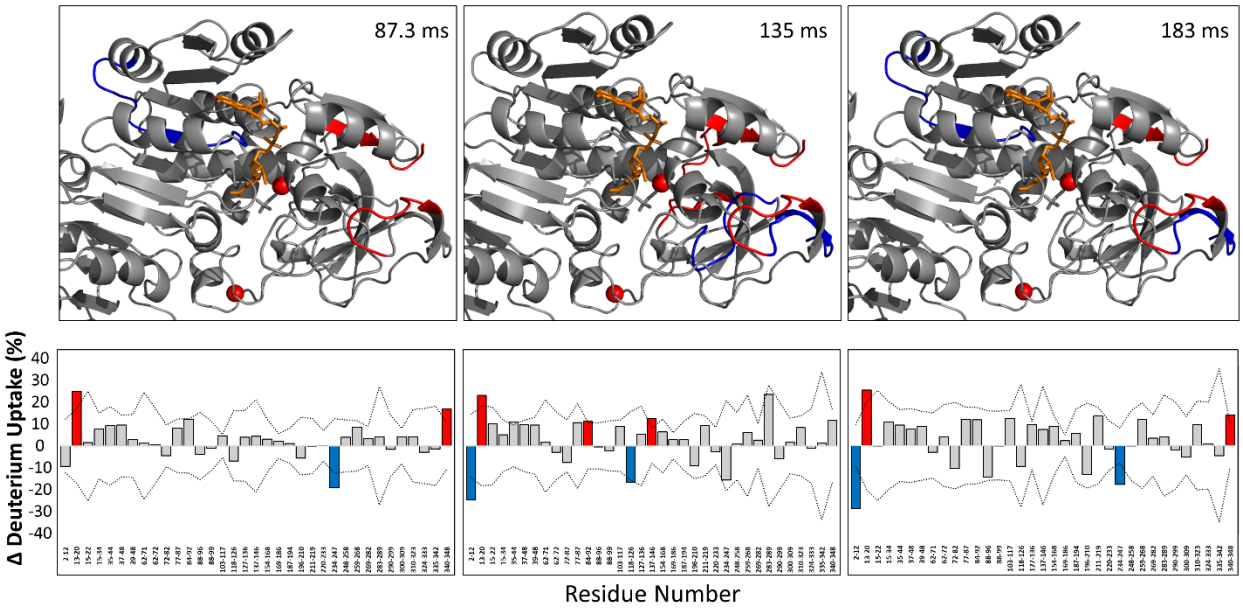

Figure 4.6 Single Time Point Local HDX Results for D_2-EtOH Catalysis Top) Mapped results of the local HDX deuterium uptake for 3 time points (87, 135 and 183 ms) during catalysis in one monomer, with dynamics > 2σ mapped to the crystal structure (red is increasing dynamics, blue is decreasing dynamics). Bottom) Local HDX results for D_2-EtOH catalysis prior to NAD^+ turnover with peptide-level changes in deuterium uptake. Regions of colour indicate statistically significant results (> 2σ). The black line outlines the 2σ confidence interval, n=9.

One region (residues 2-12) becomes rigidified by 135 ms in both D_2-EtOH and EtOH experiments (figures 4.5 and 4.6, middle panel). Once again, figure 4.6 demonstrates that regions involved in temporary dynamics (corresponding to transient intermediates) may not carry over to longer timepoints of deuteration.

4.4 Discussion

4.4.1 The Structural Implications of NAD^+ Docking

There are some striking observations to be made when comparing figures 4.3 and 4.4. While the holo and apo-enzyme forms exhibit similar dynamic behaviour upon HDX incubation in the hydride transfer phase of catalysis, the holo-enzyme (with NAD^+ bound) is approximately half as dynamic as the apo-YADH, regardless of the number of NAD^+ molecules bound. It has been previously noted that the binding of NAD^+ causes a decrease in YADH dynamics[262]. This "locking in" dynamic with 2 NAD^+ molecules bound may suggest that each monomer within the tetramer is achieving binding at one site- likely the NAD^+ binding area responsible for the interdomain cleft narrowing to facilitate ethanol catalysis[164]. When examining the local HDX dynamics of NAD^+-bound YADH relative to the apo-enzyme, there are only a few residues responsible for the overall decrease in dynamics: residues 35-44, 77-87, 137-146 and 211-219.

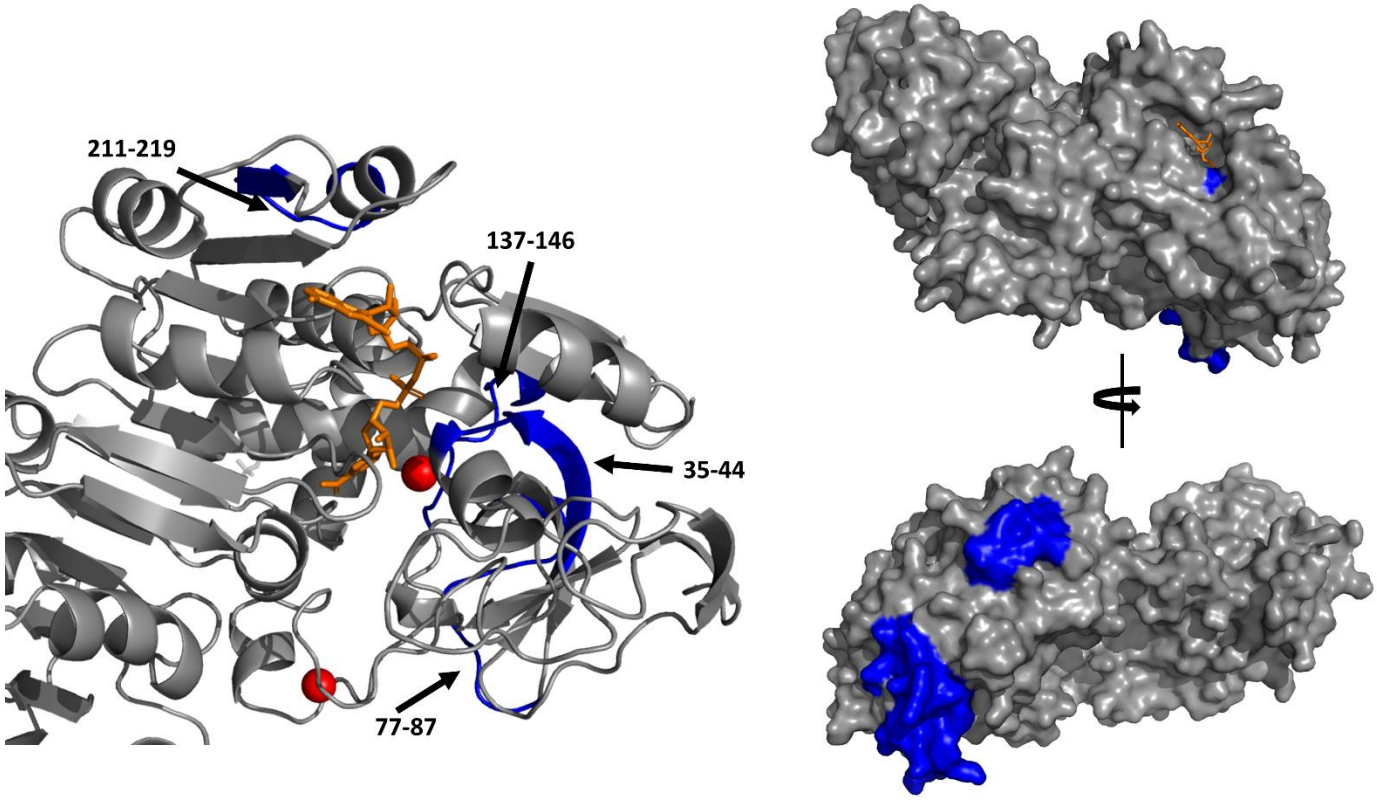

Figure 4.7 Rigidification of YADH with NAD^+ Incubation Regions of rigidification relative to apo-YADH with NAD^+ incubation are mapped in blue. Most of the rigidification with NAD^+ bound is observable in the region around the catalytic zinc (coordinated to Cys43, Cys153). A 180° rotation is displayed on the crystal structure (PBD ID: 4W6Z) to properly display the rigidification of the unstructured region on the other side of the NAD^+ binding pocket.

Another difference of note is the rapid onset dynamics of hydride transfer with $(NAD^+)_2$ compared to $(NAD^+)_4$. It is already well established that complete NAD^+ occupancy is necessary for catalysis, so observing an increase in dynamics with the deuterated ethanol catalysis with only half occupancy is opposing to the current understanding. One possible explanation would be that the lack of co-factor in half of the YADH protein (potentially in the closed form) opens the protein up to more dynamics in the region where the hydride transfer occurs in the open form, with the

inverted zinc conformation that binds Cys43, Cys153 and His66 instead of Cys46, His67 and Cys174[165,249]. This theory is further enforced by the behaviour of the D_2-EtOH experiment (red line, figure 4.3) as the experiment exceeds the timeframe for hydride transfer. After the first few timepoints, when turnover has occurred, we observe a significant drop in the amplitude of deuterium uptake for the deuterated vs. non-deuterated catalysis. This could suggest that when NAD^+ is occupying the binding pockets of the tetramer, the open form is favoured to be occupied in each dimer prior to filling the closed form of the tetramer.

4.4.2 Subtleties in Local Dynamics During Catalysis

In addition to examining global dynamics results that average the dynamic nature of the tetramer, we sought to localize results by carrying out bottom-up HDX. A kinetic isotope effect in the YADH catalysis of alcohols has been proven by numerous researchers[85,162,164,175], but the local effect of this decrease in catalysis has yet to lead to identification of residues associated with the reduction of dynamics. Deuterium uptake on the amino acid-level (seen in figures 4.5 and 4.6) produced fewer significant differences between isotopic forms of ethanol, likely due to an averaging of local results over the homo-tetrameric form (as there is no way to separately analyze the 4 monomers operating cooperatively, which may have differing catalytic activity).

One region of interest is residues 234-247, which have a decrease in dynamics with both EtOH and D_2-EtOH as substrates. This partially unstructured region that encompasses the NAD^+ binding pocket has been recorded as necessary for efficient NAD^+ reduction, and is conserved in all NAD-dependent enzymes[263]. Rigidification of this region is in line with our past discussion to the

decreased dynamics associated with maintaining NAD^+ in the binding pocket when substrate enters to ensure catalysis occurs.

The hydride transfer (time points occurring before 0.3 s) is thought to cause an increase in dynamics around the NAD^+ molecule, as the NAD^+ undergoes considerable strain during hydride transfer and potentially changes into a boat configuration in the transition state to facilitate the hydrogen transfer from the α-carbon of the alcohol and the C4 of NAD^+ (2.7 Å apart)[175]. However, as depicted in figure 4.7, we see a "locking in" of the NAD^+ molecule around the binding pocket that would infer that both NAD^+ and the catalytic zinc have limited activity without the presence of the catalytic substrate.

Since we are unable to distinguish any regions of dynamics unique to D_2-EtOH from comparing each experiment to each other under the same conditions, we sought an alternate way to examine the magnitude of the changes in dynamics. By taking a ratio of the absolute deuterium uptakes for both catalytic reactions, we can isolate which regions are exclusive to differences in the ethanol structure, instead of the NAD^+ binding alone. By taking the fraction $\frac{EtOH}{D_2-EtOH}$ and accounting for the error associated with the biological replicate, any regions that exhibit a value above 1 would demonstrate a reduction in dynamics associated exclusively with the D_2-EtOH hydride transfer.

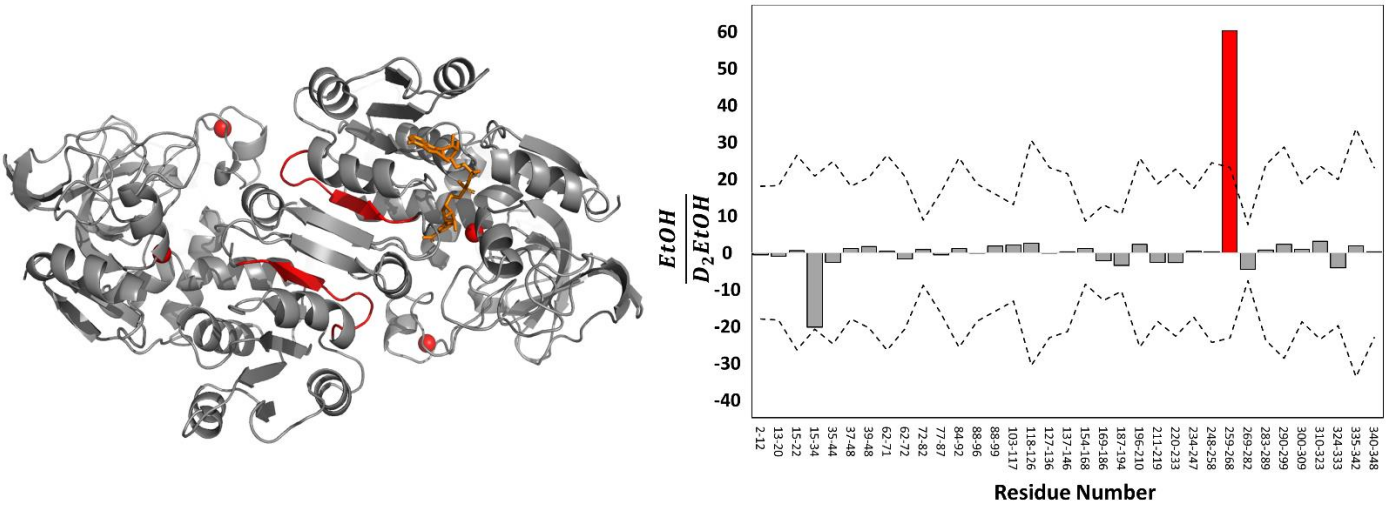

Figure 4.8 Isolation of Dynamics Associated with the Deuterated Ethanol During Catalysis Left) Crystal structure of dimeric YADH with NAD^+ bound (orange). Zinc atoms (red spheres) are shown for each monomer. The β-sheets in red correspond to residues 259-268. Right) Ratio of absolute deuterium uptake values for YADH-enabled catalysis of EtOH and D_2-EtOH.

Although residues 259-268 are not known to be involved in catalysis through interactions with the incoming substrates or coordination to zinc atoms, they are spatially close to the NAD^+ binding pocket. Figure 4.8 highlights the region in both monomers of this dimeric image. This region is mostly composed of non-polar residues (Val259, Gly263, Thr264, Thr265, Val266, Leu267, Val268), suggesting limited bonding ability with the adjacent ADH monomer by hydrogen bonding as the β-sheet in the crystal structure would suggest (although hydrogen-bonding is seen in other ADHs)[252]. Since these β-sheets are essential for linking the dimer together (and subsequently, the homo-tetramer), we postulate that using a substrate that slows down dynamics of catalysis allows us to observe the flexibility of quaternary structure farther away from the binding region; as the region around the NAD^+ molecule rigidifies to enable the hydride

transfer to occur, outer regions increase their dynamic nature to relieve conformational strain brought on by the incoming substrate into the binding region.

4.5 Conclusions

Being able to measure the conformational dynamics of yeast alcohol dehydrogenase catalysis and correlate these results with structural studies is a challenging feat. The quaternary structure is sensitive to instrument conditions and easily disassembled, while catalysis requires the addition of 2 substrates to initiate the bi-bi mechanistic sequence. By introducing ethanol into our HDX microfluidics device after the incubation of NAD^+ we were able to force the oxidation of ethanol-favoured reaction and map the dynamics of catalysis with deuterium labelling. Results herein provide evidence to the necessity of rigidification around the catalytic zinc and NAD^+ molecule before and during catalysis, along with an order of NAD^+ occupation in the quaternary structure. Although there were limited significant results on a localized level using HDX to differentiate catalysis with EtOH and D_2-EtOH, nonetheless by slowing down the dynamics of catalysis we were able to gain insights into the conformational changes that exist within each monomeric unit. We postulate that while the NAD^+ associated residues require a more structured protein for effective positioning to facilitate hydride transfer, the outer regions will have an increase in dynamics to compensate for the steric strain imposed by the substrate. Further work could be done with larger alcohol substrates that will not be catalyzed as quickly, such as a benzyl-alcohol.

4.6 Methods

Yeast alcohol dehydrogenase (A3263) and β-nicotinamide adenine dinucleotide hydrate (N7004) and HPLC-grade ethanol (99%) were purchased from Sigma Aldrich. 1,1 D_2-EtOH (98%, 1859-09-2) ampules were purchased from Cambridge Isotope Laboratories.

4.6.1 Oligomeric Optimization Through Back Pressure Manipulation

Source conditions were the following: 3.0 kV at the capillary, 200 V at the sample cone, 1.0 V at the extraction cone and a desolvation temperature of 125^o C. Several rounds of optimization were carried out and back pressure was increased on the Synapt G1 ToF to reach 5.2 mBar with a trap pressure of $7.75x10^{-3}$ bar prior to recording spectra. Trap and transfer collisional voltages were 7V and 5V, respectively. Native mass spectra was recorded with an enhanced duty cycle at 4000 *m/z* to increase resolution at this *m/z* to determine NAD^+ binding.

4.6.2 Global HDX of YADH

Experiment were primarily carried out on the Synapt G1 ToF mass spectrometer. For sample preparation, YADH (20 µM in 100 mM ammonium acetate, pH 7.0) was desalted using a 7K MWCO Zeba column. To record the apo-enzyme spectra, the stock solution was further diluted in 100mM ammonium acetate to 2 µM. For the holo-enzyme sample, YADH was incubated with NAD^+ in a molar ratio of 40:1 NAD^+ to YADH for 15 minutes, with NAD^+ having an 80 µM effective concentration upon dilution. For experiments with EtOH/D_2-EtOH, a stock solution of 250 mM EtOH was prepared daily. EtOH was mixed into the deuterium channel in order to react with YADH + NAD^+ as HDX was being recorded, having an effective concentration of 200mM upon mixing. Protein syringe was operating at a flow rate of 4 µL/min, while the deuterium syringe (with and without ethanol added) was flowing at 16 µL/min, proving an 80% deuteration rate.

Mass shifts were recorded and displayed as spectra in MassLynx. Kinetic results were displayed using SigmaPlot.

4.6.3 Local HDX Workflow

Experiments were primarily carried out on the Synapt G2 ToF mass spectrometer. Substrate concentrations and flow rates remained the same as the global HDX experiments, with the addition of a quenching and digestion step as described in Chapter 2. The deuterated sample was quenched by 5% acetic acid (pH 2.4) and a TRESI-workflow, with source conditions described elsewhere[55]. Capillaries were cleaned with solvent, acetonitrile and distilled water washes between every change in substrate to ensure no carry over of products or aggregates. The IMS cell was enabled for MS/MS identification of peptides. MS/MS results were recorded by Peter Liuni on an Orbitrap instrument from a digested protein sample of 100 *f*M/µL. Deuterium uptake was quantified using MassSpec Studio software.

Chapter 5

Conclusions and Future Work

5.1 Summary

Using a millisecond-scale analytical technique is of tremendous utility for studying protein dynamics. The work herein uses Hydrogen/Deuterium Exchange as a bioanalytical technique to further our advancement of drug design and give evidence to the conformational dynamics associated with enzymatic systems. In Chapter 1 we introduce HDX-MS as a tool for studying protein dynamics in a biologically suitable environment. We describe the pairing of this analytical technique on-line with microfluidic devices, and the impact of new device implementation on drug discovery efforts. This is followed by introductions into the enzymatic systems involved in antibiotic resistance and energy production, providing a link between their function and observable dynamics.

In Chapter 2, knowledge of the mechanistic processes surrounding substrate hydrolysis by TEM-1 was used to inform a correlation between binding modes and specific conformational dynamics with steady-state kinetics. We sequester dynamics associated with binding, productive acylation and inhibition to determine how different drug families interact with TEM-1 β-lactamase in an attempt to design new drug substances with more complex modes of inhibition. Of interest is the discovery of a requirement for rigidification of H11 for inhibition of TEM-1, the only region discovered so far as having allosteric influence on the binding site. We also examined direct evidence of a difference in turnover rate observed using our kinetic-HDX workflow to correlate an increase in cephalosporin activity associated with increased dynamics in within the protein core.

There are several complementary techniques for analyzing proteins in addition to local HDX experiments, such as studying the binding affinity of substrates and monitoring conformational

change associated with binding by IMS-MS. In Chapter 3, we further expand on the study into TEM-1 by examining quaternary structural interactions by CIU-MS, a form of IMS-MS. The impact of different inhibitors and our shortcomings in pharmaceutical studies as a community are discussed. In particular, the molar ratio of inhibitor: enzyme must be consistently monitored across pharmaceutical trials to have confidence that similar mechanistic pathways are being employed in the protein of interest. Native mass spectrometry is a straightforward technique that provides direct evidence of different binding products over time when comparing difference substrates at varying concentrations. By using CIU-MS in conjunction with local and global HDX we correlated specific inhibitory byproducts to the residues at which they inhibit, providing a definitive mechanistic byproduct formation pathway. By using a time resolved HDX method, we were also able to isolate the regions essential for complete inactivation, not just the global rigidification effect observed. These byproducts can then be ranked in order of potency, relating the CIU results to the native binding study.

Many complex enzymatic systems require a large quaternary structure and coenzymes in order to perform catalytically *in vivo*. In Chapter 4, we utilized time resolved local HDX in conjunction with global HDX to monitor the conformational dynamics associated with catalysis in a large homotetramer, yeast alcohol dehydrogenase. The dynamics associated with coenzyme binding were measured prior to making conclusive statements regarding the dynamics associated with hydride transfer. Global dynamics with complete and half occupancy of NAD^+ within the homotetramer provided differing results for the catalytic substrate, suggesting a preferred binding of NAD^+ within the open form prior to occupying the NAD^+ binding area of the closed form of the tetramer to assist the catalytic zinc. In addition, we examined the local impact of

reduced dynamics due to deuteration of the ethanol substrate on the hydride transfer between ethanol and NAD^+.

5.2 Future Work

The advent of microfluidic devices for use in bioanalytical chemistry has led to great advances in our knowledge of protein: ligand complexes and the conformational dynamics of a multitude of proteins under various reaction conditions. As discussed throughout this dissertation, microfluidic workflows enable measurements of protein dynamics that are traditionally inaccessible by other analytical techniques. Microfluidic devices and workflows enable increases in sensitivity and time before analysis prior to entering the analytical instrument[87], having the potential of being very impactful in medical research. For medical applications, microfluidic devices aid in the separation of analyte of interest from a complex biological solution[264], give rapid detection against infections[265], aid in the study of cellular death in chemotherapy[266], and in diabetes treatment[267] and gene sequencing[268]. Herein we describe an extension of this microfluidics science to complex enzymatic systems usually confirmed to tropical medicine.

5.2.1 Combatting Drug Resistance in Tropical Medicine

Tropical medicine is a crucial subset of drug development that requires additional academic research funding, primarily due to the lack of interest from pharmaceutical companies. In a world of almost 7 billion people, half lack basic sanitation and over 1 billion lack basic healthcare services and clean drinking water[269]. It is particularly difficult to measure the impact of a drug product on an individual patient in tropical illnesses, as most parasitic organisms operate through

such complex enzymatic pathways that immune responses (and subsequent affinity to medicines) vary widely, especially in patients already immunocompromised[270–272].

5.2.2 Leishmania Overview

More than 50% of deaths in the worlds poorest countries are the result of infectious diseases[269]. *Leishmania* is a protozoan parasite transmitted to humans and other mammalian hosts through the bite of phlebotomine sandflies, causing leishmaniasis (skin ulcers)[271,273]. Commonly referred to as a "poverty-related" disease, *Leishmania* affects over 150 million people worldwide, with 350 million people at risk of developing the disease and anywhere from 26,000-65,000 deaths annually[274]. In humans, there are 21 pathogenic species of *leishmania* that inhibit cytokine-inducible macrophage functions necessary for immune response to an invasive species along with an inhibition of nitric oxide prodution[275]. Several of the on the market drug treatments are exorbitantly expensive and highly toxic, relying on heavy metal dosage and the production of several byproducts that may cause additional membrane damage[272,276,277]. Due to the high toxicity and complex reactions possible on an individual basis, further research should be carried out into the initial assessment of drug product to pre-select an optimal drug product for the individual patient based on a rapid screening of immune response to a variety of potential medications.

5.2.3 Microfluidic Design Proposal for Changing Environmental Conditions

Not only are there a multitude of potential immune responses to medications, there are also changes to the parasite cellular shape and function as it travels to different hosts and is exposed

to difference acidities and temperatures[278]. In the sandfly, the parasite is exposed to a basic environment, while in a macrophage phagolysozyme the parasite has acidic surroundings.

From a pharmaceutical development platform, we propose the addition of an acidic incubation chamber subsequent to an initial chamber containing mammalian-cell conditions, to monitor conformational changes to proteins of interest in both host and pathogenic environments by a variety of techniques, such as HDX-MS or flow cytometry coupled to MS. Unfortunately, rapidly changing acidity would not be favourable to a polymer chip, so silicon and glass chips with a higher labour cost would be advised for pharmaceutical development.

5.2.4 Microfluidic Design Proposal for Simultaneous Host Environment Diagnostics

The primary challenge associated with developing microfluidics for developing countries is the point of care (POC) abilities and durability. A useful diagnostic tool must be easy to use, low-cost, stable to transport, function with a wide temperature range and be battery operated. These characteristics eliminate many current laboratory methods from becoming popular in a local community health centre.

Using our current PMMA chip design would allow for reproducible designs and generate sturdy devices that can be produced in large quantities. Original microfluidic devices were prepared using silicon, but the use of polymers has widely surpassed this technique due to the easier production and lower cost[88,279,280]. In addition to this durable polymeric structure, adding a new ablation pattern that mimics the extracellular matrix would allow for a more detailed examination of the environment surrounding the protein/cell of interest. For example, it is possible to simulate the microenvironments of multiple types of body tissue (bone, liver, kidneys)

to study the toxicity of drug products as they travel through the system to determine potential side effects[281,282]. Once optimized, it could be possible to mass produce the unique microfluidic surfaces for differing host environments and solution conditions.

REFERENCES

(1) Wien, W. Duration of the Luminescence of Atoms. *Umsch. 1897* **1924**, *28*, 441–443.

(2) Urban, P. L. Clarifying Misconceptions about Mass and Concentration Sensitivity. *J. Chem. Educ.* **2016**, *93*, 984–987.

(3) Knochenmuss, R.; Zenobi, R. MALDI Ionization: The Role of in-Plume Processes. *Chem. Rev. Wash. DC U. S.* **2003**, *103*, 441–452.

(4) Rayleigh, Lord. XX. On the Equilibrium of Liquid Conducting Masses Charged with Electricity. *Lond. Edinb. Dublin Philos. Mag. J. Sci.* **1882**, *14* (87), 184–186.

(5) Wilson, D. J.; Konermann, L. Mechanistic Studies on Enzymatic Reactions by Electrospray Ionization MS Using a Capillary Mixer with Adjustable Reaction Chamber Volume for Time-Resolved Measurements. *Anal. Chem.* **2004**, *76* (9), 2537–2543.

(6) Ahadi, E.; Konermann, Lars. Modeling the Behavior of Coarse-Grained Polymer Chains in Charged Water Droplets: Implications for the Mechanism of Electrospray Ionization. *J. Phys. Chem. B* **2012**, *116*, 104–112.

(7) Kebarle, P.; Verkerk, U. H. Electrospray: From Ions in Solution to Ions in the Gas Phase, What We Know Now. *Mass Spectrom. Rev.* **2009**, *28*, 898–917.

(8) Whitehouse, C. M.; Dreyer, R. N.; Yamashita, M.; Fenn, J. B. Electrospray Interface for Liquid Chromatographs and Mass Spectrometers. *Anal. Chem.* **1985**, *57*, 675–679.

(9) Schmelzeisen-Redeker, G.; Buetfering, L.; Roellgen, F. W. Desolvation of Ions and Molecules in Thermospray Mass Spectrometry. *Int. J. Mass Spectrom. Ion Process.* **1989**, *90*, 139–150.

(10) Smith, J. N.; Flagan, R. C.; Beauchamp, J. L. Droplet Evaporation and Discharge Dynamics in Electrospray Ionization. *J. Phys. Chem. A* **2002**, *106*, 9957–9967.

(11) Crotti, S.; Seraglia, R.; Traldi, Pietro. Some Thoughts on Electrospray Ionization Mechanisms. *Eur. J. Mass Spectrom.* **2011**, *17*, 85–100.

(12) Ikonomou, M. G.; Blades, A. T.; Kebarle, Paul. Electrospray-Ion Spray: A Comparison of Mechanisms and Performance. *Anal. Chem.* **1991**, *63*, 1989–1998.

(13) De la Mora, J. F.; Van Berkel, G. J.; Enke, C. G.; Cole, R. B.; Martinez-Sanchez, M.; Fenn, J. B. Electrochemical Processes in Electrospray Ionization Mass Spectrometry. *J. Mass Spectrom.* **2000**, *35*, 939–952.

(14) Van Berkel, G. J.; Kertesz, Vilmos. Using the Electrochemistry of the Electrospray Ion Source. *Anal. Chem. Wash. DC U. S.* **2007**, *79*, 5510–5520.

(15) Loeb, L. B.; Kip, A. F.; Hudson, G. G.; Bennett, W. H. Pulses in Negative Point-to-Plane Corona. *Phys. Rev.* **1941**, *60* (10), 714–722.

(16) Young, J. P.; Shaw, R. W.; Goeringer, D. E.; Smith, D. H.; Christie, W. H. Analytical Capabilities of Inorganic Resonance Ionization Mass Spectrometry. *Anal. Instrum. N. Y.* **1988**, *17*, 41–68.

(17) Allen, M. H.; Vestal, M. L. Design and Performance of a Novel Electrospray Interface. *J. Am. Soc. Mass Spectrom.* **1992**, *3*, 18–26.

(18) Taylor, G. I.; McEwan, A. D. The Stability of a Horizontal Fluid Interface in a Vertical Electric Field. *J. Fluid Mech.* **1965**, *22* (1), 1–15.

(19) Chernushevich, I. V.; Thomson, B. A. Collisional Cooling of Large Ions in Electrospray Mass Spectrometry. *Anal. Chem.* **2004**, *76*, 1754–1760.

(20) Wilm, M.; Mann, Matthias. Analytical Properties of the Nanoelectrospray Ion Source. *Anal. Chem.* **1996**, *68*, 1–8.

(21) Korner, R.; Wilm, M.; Morand, K.; Schubert, M.; Mann, M. Nano Electrospray Combined with a Quadrupole Ion Trap for the Analysis of Peptides and Protein Digests. *J. Am. Soc. Mass Spectrom.* **1996**, *7*, 150–156.

(22) Dole, M.; Mack, L. L.; Hines, R. L.; Mobley, R. C.; Ferguson, L. D.; Alice, M. B. Molecular Beams of Macroions. *J. Chem. Phys.* **1968**, *49*, 2240–2249.

(23) Iribarne, J. V. On the Evaporation of Small Ions from Charged Droplets. *J. Chem. Phys.* **1976**, *64* (6), 2287.

(24) Konermann, L.; Ahadi, E.; Rodriguez, A. D.; Vahidi, Siavash. Unraveling the Mechanism of Electrospray Ionization. *Anal. Chem. Wash. DC U. S.* **2013**, *85*, 2–9.

(25) Fernandez de la Mora, J. Electrospray Ionization of Large Multiply Charged Species Proceeds via Dole's Charged Residue Mechanism. *Anal. Chim. Acta* **2000**, *406* (1), 93–104.

(26) Wilm, Matthias. Principles of Electrospray Ionization. *Mol. Cell. Proteomics* **2011**, *10*, M111.009407, 8 pp.

(27) Metwally, H.; Duez, Q.; Konermann, L. Chain Ejection Model for Electrospray Ionization of Unfolded Proteins: Evidence from Atomistic Simulations and Ion Mobility Spectrometry. *Anal. Chem.* **2018**, *90* (16), 10069–10077.

(28) Sobott, F.; Hernandez, H.; McCammon, M. G.; Tito, M. A.; Robinson, C. V. A Tandem Mass Spectrometer for Improved Transmission and Analysis of Large Macromolecular Assemblies. *Anal. Chem.* **2002**, *74*, 1402–1407.

(29) McKay, A. R.; Ruotolo, B. T.; Ilag, L. L.; Robinson, C. V. Mass Measurements of Increased Accuracy Resolve Heterogeneous Populations of Intact Ribosomes. *J. Am. Chem. Soc.* **2006**, *128*, 11433–11442.

(30) Tanaka, K.; Waki, H.; Ido, Y.; Akita, S.; Yoshida, Y.; Yohida, Tamio. Protein and Polymer Analyses up to m/z 100,000 by Laser Ionization Time-of-Flight Mass Spectrometry. *Rapid Commun. Mass Spectrom.* **1988**, *2*, 151–153.

(31) Chernushevich, I. V.; Loboda, A. V.; Thomson, B. A. An Introduction to Quadrupole-Time-of-Flight Mass Spectrometry. *J. Mass Spectrom.* **2001**, *36*, 849–865.

(32) Lapthorn, C.; Pullen, F.; Chowdhry, B. Z. Ion Mobility Spectrometry-Mass Spectrometry (IMS-MS) of Small Molecules: Separating and Assigning Structures to Ions. *Mass Spectrom. Rev.* **2013**, *32*, 43–71.

(33) McDaniel, E. W.; Martin, D. W.; Barnes, W. S. Drift-Tube Mass Spectrometer for Studies of Low-Energy Ion-Molecule Reactions. *Rev. Sci. Instrum.* **1962**, *33*, 2–7.

(34) Mason, E. A.; Schamp, H. W., Jr. Mobility of Gaseous Ions in Weak Electric Fields. *Ann. Phys. San Diego CA U. S.* **1958**, *4*, 233–270.

(35) Theisen, A.; Black, R.; Corinti, D.; Brown, J. M.; Bellina, B.; Barran, P. E. Initial Protein Unfolding Events in Ubiquitin, Cytochrome c and Myoglobin Are Revealed with the Use of 213 Nm UVPD Coupled to IM-MS. *J. Am. Soc. Mass Spectrom.* **2018**, Ahead of Print.

(36) Bush, M. F.; Hall, Z.; Giles, K.; Hoyes, J.; Robinson, C. V.; Ruotolo, B. T. Collision Cross Sections of Proteins and Their Complexes: A Calibration Framework and Database for Gas-Phase Structural Biology. *Anal. Chem. Wash. DC U. S.* **2010**, *82*, 9557–9565.

(37) Valentine, S. J.; Anderson, J. G.; Ellington, A. D.; Clemmer, D. E. Disulfide-Intact and -Reduced Lysozyme in the Gas Phase: Conformations and Pathways of Folding and Unfolding. *J. Phys. Chem. B* **1997**, *101*, 3891–3900.

(38) Ruotolo, B. T.; Benesch, J. L. P.; Sandercock, A. M.; Hyung, S.-J.; Robinson, C. V. Ion Mobility–Mass Spectrometry Analysis of Large Protein Complexes. *Nat. Protoc.* **2008**, *3*, 1139.

(39) Maleki, H.; Karanji, A. K.; Majuta, S.; Maurer, M. M.; Valentine, S. J. Ion Mobility Spectrometry-Mass Spectrometry Coupled with Gas-Phase Hydrogen/Deuterium Exchange for Metabolomics Analyses. *J. Am. Soc. Mass Spectrom.* **2018**, *29*, 230–241.

(40) Dixit, S. M.; Polasky, D. A.; Ruotolo, B. T. Collision Induced Unfolding of Isolated Proteins in the Gas Phase: Past, Present, and Future. *Curr. Opin. Chem. Biol.* **2018**, *42*, 93–100.

(41) Ruotolo, B. T.; Giles, K.; Campuzano, I.; Sandercock, A. M.; Bateman, R. H.; Robinson, C. V. Evidence for Macromolecular Protein Rings in the Absence of Bulk Water. *Sci. Wash. DC U. S.* **2005**, *310*, 1658–1661.

(42) Benesch, J. L.; Robinson, C. V. Mass Spectrometry of Macromolecular Assemblies: Preservation and Dissociation. *Curr. Opin. Struct. Biol.* **2006**, *16*, 245–251.

(43) Hernandez, H.; Robinson, C. V. Determining the Stoichiometry and Interactions of Macromolecular Assemblies from Mass Spectrometry. *Nat. Protoc.* **2007**, *2*, 715–726.

(44) Scarff, C. A.; Thalassinos, K.; Hilton, G. R.; Scrivens, J. H. Travelling Wave Ion Mobility Mass Spectrometry Studies of Protein Structure: Biological Significance and Comparison with X-Ray Crystallography and Nuclear Magnetic Resonance Spectroscopy Measurements. *Rapid Commun. Mass Spectrom.* **2008**, *22*, 3297–3304.

(45) Cubrilovic, D.; Biela, A.; Sielaff, F.; Steinmetzer, T.; Klebe, G.; Zenobi, Renato. Quantifying Protein-Ligand Binding Constants Using Electrospray Ionization Mass Spectrometry: A Systematic Binding Affinity Study of a Series of Hydrophobically Modified Trypsin Inhibitors. *J. Am. Soc. Mass Spectrom.* **2012**, *23*, 1768–1777.

(46) Shi, X.; Nishimura, Y.; Akashi, S.; Takamizawa, A.; Hiraoka, K. Evaluation of Binding Affinity of Protein-Mutant Dna Complexes in Solution by Laser Spray Mass Spectrometry. *J. Am. Soc. Mass Spectrom.* **2006**, *17* (4), 611–620.

(47) Daniel, J. M.; Friess, S. D.; Rajagopalan, S.; Wendt, S.; Zenobi, Renato. Quantitative Determination of Noncovalent Binding Interactions Using Soft Ionization Mass Spectrometry. *Int. J. Mass Spectrom.* **2002**, *216*, 1–27.

(48) Wells, J. M.; McLuckey, S. A. Collision-Induced Dissociation (CID) of Peptides and Proteins. *Methods Enzymol.* **2005**, *402*, 148–185.

(49) Niu, S.; Rabuck, J. N.; Ruotolo, B. T. Ion Mobility-Mass Spectrometry of Intact Protein-Ligand Complexes for Pharmaceutical Drug Discovery and Development. *Curr. Opin. Chem. Biol.* **2013**, *17*, 809–817.

(50) Giles, K.; Pringle, S. D.; Worthington, K. R.; Little, D.; Wildgoose, J. L.; Bateman, R. H. Applications of a Travelling Wave-Based Radio-Frequency-Only Stacked Ring Ion Guide. *Rapid Commun. Mass Spectrom. RCM* **2004**, *18*, 2401–2414.

(51) Engen, J. R. Analysis of Protein Conformation and Dynamics by Hydrogen/Deuterium Exchange MS. *Anal. Chem. Wash. DC U. S.* **2009**, *81*, 7870–7875.

(52) Roder, H.; Elove, G. A.; Englander, S. W. Structural Characterization of Folding Intermediates in Cytochrome c by H-Exchange Labelling and Proton NMR. *Nature* **1988**, *335*, 700–704.

(53) Zhu, S.; Shala, A.; Audette, G.; Bezginov, A.; Sljoka, A.; Wilson, D. J. Hyperphosphorylation of Intrinsically Disordered Tau Protein Induces an Amyloidogenic Shift in Its Conformational Ensemble. *PloS One* **2015**, *10*, e0120416.

(54) Brown, K. A.; Sharifi, S.; Hussain, R.; Donaldson, L.; Bayfield, M. A.; Wilson, D. J. Distinct Dynamic Modes Enable the Engagement of Dissimilar Ligands in a Promiscuous Atypical RNA Recognition Motif. *Biochemistry* **2016**, *55* (51), 7141–7150.

(55) Knox, R.; Lento, C.; Wilson, D. J. Mapping Conformational Dynamics to Individual Steps in the TEM-1 β-Lactamase Catalytic Mechanism. *J. Mol. Biol.* **2018**, *430,* 3311-3322.

(56) Simmons, D. A.; Dunn, S. D.; Konermann, Lars. Conformational Dynamics of Partially Denatured Myoglobin Studied by Time-Resolved Electrospray Mass Spectrometry with Online Hydrogen-Deuterium Exchange. *Biochemistry* **2003**, *42*, 5896–5905.

(57) Katta, V.; Chait, B. T. Conformational Changes in Proteins Probed by Hydrogen-Exchange Electrospray-Ionization Mass Spectrometry. *Rapid Commun. Mass Spectrom.* **1991**, *5*, 214–217.

(58) Pan, J.; Han, J.; Borchers, C. H.; Konermann, Lars. Characterizing Short-Lived Protein Folding Intermediates by Top-Down Hydrogen Exchange Mass Spectrometry. *Anal. Chem. Wash. DC U. S.* **2010**, *82*, 8591–8597.

(59) Smith, D. L.; Deng, Y.; Zhang, Zhongqi. Probing the Non-Covalent Structure of Proteins by Amide Hydrogen Exchange and Mass Spectrometry. *J. Mass Spectrom.* **1997**, *32*, 135–146.

(60) Kan, Z.-Y.; Walters, B. T.; Mayne, L.; Englander, S. W. Protein Hydrogen Exchange at Residue Resolution by Proteolytic Fragmentation Mass Spectrometry Analysis. *Proc. Natl. Acad. Sci.* **2013**, *110* (41), 16438–16443.

(61) Hvidt, A.; Linderstrom-Lang, K. Exchange of Hydrogen Atoms in Insulin with Deuterium Atoms in Aqueous Solutions. *Biochim. Biophys. Acta* **1954**, *14*, 574–575.

(62) Englander, S. W.; Mayne, L.; Bai, Y.; Sosnick, T. R. Hydrogen Exchange: The Modern Legacy of Linderstrom-Lang. *Protein Sci.* **1997**, *6*, 1101–1109.

(63) Bai, Y.; Milne, J. S.; Mayne, L.; Englander, S. Walter. Primary Structure Effects on Peptide Group Hydrogen Exchange. *Proteins Struct. Funct. Genet.* **1993**, *17*, 75–86.

(64) Krishna, M. M. G.; Hoang, L.; Lin, Y.; Englander, S. Walter. Hydrogen Exchange Methods to Study Protein Folding. *Methods San Diego CA U. S.* **2004**, *34*, 51–64.

(65) Zhang, Z.; Smith, D. L. Determination of Amide Hydrogen Exchange by Mass Spectrometry: A New Tool for Protein Structure Elucidation. *Protein Sci.* **1993**, *2*, 522–531.

(66) Perrin, C. L.; Arrhenius, G. M. L. Mechanisms of Acid-Catalyzed Proton Exchange in N-Methyl Amides. *J. Am. Chem. Soc.* **1982**, *104*, 6693–6696.

(67) Perrin, C. L. Proton Exchange in Amides: Surprises from Simple Systems. *Acc. Chem. Res.* **1989**, *22*, 268–275.

(68) Weis, D. D. *Hydrogen Exchange Mass Spectrometry of Proteins : Fundamentals, Methods, and Applications*; 2016.

(69) Englander, S. W.; Poulsen, A. Hydrogen-Tritium Exchange of the Random Chain Polypeptide. *Biopolymers* **1969**, *7*, 379–393.

(70) Loo, J. A.; Edmonds, C. G.; Udseth, H. R.; Smith, R. D. Effect of Reducing Disulfide-Containing Proteins on Electrospray Ionization Mass Spectra. *Anal. Chem.* **1990**, *62*, 693–698.

(71) Skinner, J. J.; Lim, W. K.; Bédard, S.; Black, B. E.; Englander, S. W. Protein Hydrogen Exchange: Testing Current Models. *Protein Sci.* **2012**, *21* (7), 987–995.

(72) Konermann, L.; Pan, J.; Liu, Y.-Hong. Hydrogen Exchange Mass Spectrometry for Studying Protein Structure and Dynamics. *Chem. Soc. Rev.* **2011**, *40* (3), 1224–1234.

(73) Xiao, H.; Hoerner, J. K.; Eyles, S. J.; Dobo, A.; Voigtman, E.; Mel'cuk, A. I.; Kaltashov, I. A. Mapping Protein Energy Landscapes with Amide Hydrogen Exchange and Mass Spectrometry: I.

A Generalized Model for a Two-State Protein and Comparison with Experiment. *Protein Sci.* **2005**, *14*, 543–557.

(74) Pandey, A.; Mann, Matthias. Proteomics to Study Genes and Genomes. *Nat. Lond.* **2000**, *405*, 837–846.

(75) Konermann, L.; Rosell, F. I.; Mauk, A. G.; Douglas, D. J. Acid-Induced Denaturation of Myoglobin Studied by Time-Resolved Electrospray Ionization Mass Spectrometry. *Biochemistry* **1997**, *36*, 6448–6454.

(76) Kolakowski, B. M.; Simmons, D. A.; Konermann, Lars. Stopped-Flow Electrospray Ionization Mass Spectrometry: A New Method for Studying Chemical Reaction Kinetics in Solution. *Rapid Commun. Mass Spectrom.* **2000**, *14*, 772–776.

(77) Pan, J.; Wilson, D. J.; Konermann, L. Pulsed Hydrogen Exchange and Electrospray Charge-State Distribution as Complementary Probes of Protein Structure in Kinetic Experiments: Implications for Ubiquitin Folding. *Biochemistry* **2005**, *44* (24), 8627–8633.

(78) Udgaonkar, J. B.; Baldwin, R. L. NMR Evidence for an Early Framework Intermediate on the Folding Pathway of Ribonuclease A. *Nat. Lond. U. K.* **1988**, *335*, 694–699.

(79) Henzler-Wildman, K. A.; Lei, M.; Thai, V.; Kerns, S. J.; Karplus, M.; Kern, Dorothee. A Hierarchy of Timescales in Protein Dynamics Is Linked to Enzyme Catalysis. *Nat. Lond. U. K.* **2007**, *450*, 913–916.

(80) Boehr, D. D.; Dyson, H. J.; Wright, P. E. An NMR Perspective on Enzyme Dynamics. *Chem. Rev. Wash. DC U. S.* **2006**, *106*, 3055–3079.

(81) Zechel, D. L.; Konermann, L.; Withers, S. G.; Douglas, D. J. Pre-Steady State Kinetic Analysis of an Enzymic Reaction Monitored by Time-Resolved Electrospray Ionization Mass Spectrometry. *Biochemistry* **1998**, *37*, 7664–7669.

(82) Marrella, S. A.; Brown, K. A.; Mansouri-Noori, F.; Porat, J.; Wilson, D. J.; Bayfield, M. A. An Interdomain Bridge Influences RNA Binding of the Human La Protein. *J. Biol. Chem.* **2018**, *294 (5)*, 1529-1540.

(83) Puckett, L. G.; Dikici, E.; Lai, S.; Madou, M.; Bachas, L. G.; Daunert, S. Investigation into the Applicability of the Centrifugal Microfluidics Platform for the Development of Protein-Ligand Binding Assays Incorporating Enhanced Green Fluorescent Protein as a Fluorescent Reporter. *Anal. Chem.* **2004**, *76*, 7263–7268.

(84) Konermann, L.; Collings, B. A.; Douglas, D. J. Cytochrome c Folding Kinetics Studied by Time-Resolved Electrospray Ionization Mass Spectrometry. *Biochemistry* **1997**, *36*, 5554–5559.

(85) Liuni, P.; Jeganathan, A.; Wilson, D. J. Conformer Selection and Intensified Dynamics During Catalytic Turnover in Chymotrypsin. *Angew. Chem. Int. Ed.* **2012**, *51*, 9666–9669.

(86) Liuni, P.; Rob, T.; Wilson, D. J. A Microfluidic Reactor for Rapid, Low-Pressure Proteolysis with on-Chip Electrospray Ionization. *Rapid Commun. Mass Spectrom.* **2010**, *24*, 315–320.

(87) Manz, A.; Graber, N.; Widmer, H. M. Miniaturized Total Chemical Analysis Systems: A Novel Concept for Chemical Sensing. *Sens. Actuators B Chem.* **1990**, 244–248.

(88) Whitesides, G. M. The Origins and the Future of Microfluidics. *Nat. Lond. U. K.* **2006**, *442*, 368–373.

(89) Lee, J.; Soper, S. A.; Murray, K. K. Microfluidic Chips for Mass Spectrometry-Based Proteomics. *J. Mass Spectrom.* **2009**, *44*, 579–593.

(90) McEnery, M.; Tan, A.; Glennon, J. D.; Alderman, J.; Patterson, J.; O'Mathuna, S. C. Liquid Chromatography On-Chip: Progression towards a μ-Total Analysis System. *Anal. Camb. U. K.* **2000**, *125*, 25–27.

(91) Harrison, D. J.; Manz, A.; Fan, Z.; Luedi, H.; Widmer, H. Michael. Capillary Electrophoresis and Sample Injection Systems Integrated on a Planar Glass Chip. *Anal. Chem.* **1992**, *64*, 1926–1932.

(92) Bings, N. H.; Wang, C.; Skinner, C. D.; Colyer, C. L.; Thibault, P.; Harrison, D. Jed. Microfluidic Devices Connected to Fused-Silica Capillaries with Minimal Dead Volume. *Anal. Chem.* **1999**, *71*, 3292–3296.

(93) Krenkova, J.; Lacher, N. A.; Svec, F. Highly Efficient Enzyme Reactors Containing Trypsin and Endoproteinase LysC Immobilized on Porous Polymer Monolith Coupled to MS Suitable for Analysis of Antibodies. *Anal. Chem.* **2009**, *81* (5), 2004–2012.

(94) Fortier, M.-H.; Bonneil, E.; Goodley, P.; Thibault, Pierre. Integrated Microfluidic Device for Mass Spectrometry-Based Proteomics and Its Application to Biomarker Discovery Programs. *Anal. Chem.* **2005**, *77*, 1631–1640.

(95) Svejdal, R. R.; Dickinson, E. R.; Sticker, D.; Kutter, J. P.; Rand, K. D. Thiol-Ene Microfluidic Chip for Performing Hydrogen/Deuterium Exchange of Proteins at Subsecond Time Scales. *Anal. Chem. Wash. DC U. S.* **2019**, *91*, 1309–1317.

(96) Fleming, A. The Antibacterial Action of Cultures of a Penicillium, with Special Reference to Their Use in the Isolation of B. Influenzae. *Br. J. Exp. Pathol.* **1929**, *10*, 226–236.

(97) Meneksedag, D.; Dogan, A.; Kanlikilicer, P.; Ozkirimli, Elif. Communication between the Active Site and the Allosteric Site in Class A Beta-Lactamases. *Comput. Biol. Chem.* **2013**, *43*, 1–10.

(98) Avci, F. G.; Altinisik, F. E.; Vardar Ulu, D.; Ozkirimli Olmez, E.; Sariyar Akbulut, B. An Evolutionarily Conserved Allosteric Site Modulates Beta-Lactamase Activity. *J. Enzyme Inhib. Med. Chem.* **2016**, *6366* (January), 1–8.

(99) Krizova, L.; Poirel, L.; Nordmann, P.; Nemec, Alexandr. TEM-1 β-Lactamase as a Source of Resistance to Sulbactam in Clinical Strains of Acinetobacter Baumannii. *J. Antimicrob. Chemother.* **2013**, *68*, 2786–2791.

(100) Meroueh, S. O.; Fisher, J. F.; Schlegel, H. B.; Mobashery, Shahriar. Ab Initio QM/MM Study of Class A β-Lactamase Acylation: Dual Participation of Glu166 and Lys73 in a Concerted Base Promotion of Ser70. *J. Am. Chem. Soc.* **2005**, *127* (44), 15397–15407.

(101) Courtney, C. M.; Chatterjee, Anushree. Sequence-Specific Peptide Nucleic Acid-Based Antisense Inhibitors of TEM-1 β-Lactamase and Mechanism of Adaptive Resistance. *ACS Infect. Dis.* **2015**, *1* (6), 253–263.

(102) Fleming-Dutra KE; Hersh AL; Shapiro DJ; et al. Prevalence of Inappropriate Antibiotic Prescriptions among Us Ambulatory Care Visits, 2010-2011. *JAMA* **2016**, *315* (17), 1864–1873.

(103) Nordmann, P.; Dortet, L.; Poirel, Laurent. Carbapenem Resistance in Enterobacteriaceae: Here Is the Storm. *Trends Mol. Med.* **2012**, *18* (5), 263–272.

(104) Poirel, L.; Nordmann, P. Carbapenem Resistance in Acinetobacter Baumannii: Mechanisms and Epidemiology. *Clin. Microbiol. Infect.* **2006**, *12*, 826–836.

(105) Goffin, C.; Ghuysen, J.-Marie. Multimodular Penicillin-Binding Proteins: An Enigmatic Family of Orthologs and Paralogs. *Microbiol. Mol. Biol. Rev.* **1998**, *62*, 1079–1093.

(106) Spratt, B. G. Distinct Penicillin Binding Proteins Involved in the Division, Elongation, and Shape of Escherichia Coli K12. *Proc. Natl. Acad. Sci. U. S. A.* **1975**, *72*, 2999–3003.

(107) Scheffers, D.-J.; Pinho, M. G. Bacterial Cell Wall Synthesis: New Insights from Localization Studies. *Microbiol. Mol. Biol. Rev.* **2005**, *69*, 585–607.

(108) Fisher, J. F.; Meroueh, S. O.; Mobashery, Shahriar. Bacterial Resistance to β-Lactam Antibiotics: Compelling Opportunism, Compelling Opportunity. *Chem. Rev. Wash. DC U. S.* **2005**, *105*, 395–424.

(109) Waxman, D. J.; Strominger, J. L. Penicillin-Binding Proteins and the Mechanism of Action of β-Lactam Antibiotics. *Annu. Rev. Biochem.* **1983**, *52*, 825–869.

(110) Hartman, B. J.; Tomasz, Alexander. Low-Affinity Penicillin-Binding Protein Associated with β-Lactam Resistance in Staphylococcus Aureus. *J. Bacteriol.* **1984**, *158*, 513–516.

(111) Lim, D.; Strynadka, N. C. J. Structural Basis for the β Lactam Resistance of PBP2a from Methicillin-Resistant Staphylococcus Aureus. *Nat. Struct. Biol.* **2002**, *9*, 870–876.

(112) Courtney, C. M.; Chatterjee, Anushree. Sequence-Specific Peptide Nucleic Acid-Based Antisense Inhibitors of TEM-1 β-Lactamase and Mechanism of Adaptive Resistance. *ACS Infect. Dis.* **2015**, *1* (6), 253–263.

(113) Marciano, D. C.; Brown, N. G.; Palzkill, T. Analysis of the Plasticity of Location of the Arg244 Positive Charge within the Active Site of the TEM-1 β-Lactamase. *Protein Sci.* **2009**, *18* (10), 2080–2089.

(114) Dunn, G. L. Ceftizoxime and Other Third-Generation Cephalosporins: Structure-Activity Relationships. *J. Antimicrob. Chemother.* **1982**, *10*, 1–10.

(115) Medeiros, A. A. Evolution and Dissemination of β-Lactamases Accelerated by Generations of β-Lactam Antibiotics. *Clin. Infect. Dis.* **1997**, *24*, S19–S45.

(116) Salverda, M. L. M.; de Visser, J. A. G. M.; Barlow, M. Natural Evolution of TEM-1 β-Lactamase: Experimental Reconstruction and Clinical Relevance. *FEMS Microbiol. Rev.* **2010**, *34* (6), 1015–1036.

(117) Bershtein, S.; Goldin, K.; Tawfik, D. S. Intense Neutral Drifts Yield Robust and Evolvable Consensus Proteins. *J. Mol. Biol.* **2008**, *379* (5), 1029–1044.

(118) Haidar, G.; Nguyen, M. H.; Clancy, C. J.; Shields, R. K.; Cheng, S.; Nguyen, M. H.; Clancy, C. J.; Shields, R. K.; Hao, B.; Nguyen, M. H.; et al. Mutations in BlaKPC-3 That Confer Ceftazidime-Avibactam Resistance Encode Novel KPC-3 Variants That Function as Extended-Spectrum β-Lactamases. *Antimicrob. Agents Chemother.* **2017**, *61* (5).

(119) Shields, R. K.; Chen, L.; Cheng, S.; Chavda, K. D.; Press, E. G.; Snyder, A.; Pandey, R.; Doi, Y.; Kreiswirth, B. N.; Nguyen, M. H.; et al. Emergence of Ceftazidime-Avibactam Resistance Due to Plasmid-Borne BlaKPC-3 Mutations during Treatment of Carbapenem-Resistant Klebsiella Pneumoniae Infections. *Antimicrob. Agents Chemother.* **2017**, *61* (3), e02097-16/1-e02097-16/11.

(120) Ehmann, D. E.; Jahic, H.; Ross, P. L.; Gu, R.-F.; Hu, J.; Kern, G.; Walkup, G. K.; Fisher, S. L. Avibactam Is a Covalent, Reversible, Non-β-Lactam β-Lactamase Inhibitor. *Proc. Natl. Acad. Sci. U. S. Am. Early Ed.* **2012**, No. July 2 2012, 1–6, 6 pp.

(121) Fisher, J.; Belasco, J. G.; Khosla, S.; Knowles, J. R. β-Lactamase Proceeds via an Acyl-Enzyme Intermediate. Interaction of the Escherichia Coli RTEM Enzyme with Cefoxitin. *Biochemistry* **1980**, *19* (13), 2895–2901.

(122) Delaire, M.; Lenfant, F.; Labia, R.; Masson, J. Michel. Site-Directed Mutagenesis on TEM-1 β-Lactamase: Role of Glu166 in Catalysis and Substrate Binding. *Protein Eng.* **1991**, *4* (7), 805–810.

(123) Matagne, A.; Misselyn-Bauduin, A. M.; Joris, B.; Erpicum, T.; Granier, B.; Frere, J. Marie. The Diversity of the Catalytic Properties of Class A β-Lactamases. *Biochem. J.* **1990**, *265* (1), 131–146.

(124) Imtiaz, U.; Manavathu, E. K.; Lerner, S. A.; Mobashery, Shahriar. Critical Hydrogen Bonding by Serine 235 for Cephalosporinase Activity of TEM-1 β-Lactamase. *Antimicrob. Agents Chemother.* **1993**, *37* (11), 2438–2442.

(125) Brink, A. J.; Coetzee, J.; Clay, C. G.; Sithole, S.; Richards, G. A.; Poirel, L.; Nodrmann, Patrice. Emergence of New Delhi Metallo-Beta-Lactamase (NDM-1) and Klebsiella Pneumoniae Carbapenemase (KPC-2) in South Africa. *J. Clin. Microbiol.* **2012**, *50* (2), 525–527.

(126) Hendriksen, R. S.; Joensen, K. G.; Lukwesa-Musyani, C.; Kalondaa, A.; Leekitcharoenphon, P.; Nakazwe, R.; Aarestrup, F. M.; Hasman, H.; Mwansa, J. C. L. Extremely Drug-Resistant Salmonella Enterica Serovar Senftenberg Infections in Patients in Zambia. *J. Clin. Microbiol.* **2013**, *51* (1), 284–286.

(127) Cooper, A.; Dryden, D. T. F. Allostery without Conformational Change - A Plausible Model. *Eur. Biophys. J.* **1984**, *11* (2), 103–109.

(128) Pimenta, A. C.; Martins, J. M.; Fernandes, R.; Moreira, I. S. Ligand-Induced Structural Changes in TEM-1 Probed by Molecular Dynamics and Relative Binding Free Energy Calculations. *J. Chem. Inf. Model.* **2013**, *53* (10), 2648–2658.

(129) Saves, I.; Burlet-Schiltz, O.; Maveyraud, L.; Samama, J.-P.; Prome, J.-C.; Masson, J.-Michel. Mass Spectral Kinetic Study of Acylation and Deacylation During the Hydrolysis of Penicillins and Cefotaxime by β-Lactamase TEM-1 and the G238S Mutant. *Biochemistry* **1995**, *34* (37), 11660–11667.

(130) Bratulic, S.; Gerber, F.; Wagner, Andreas. Mistranslation Drives the Evolution of Robustness in TEM-1 β-Lactamase. *Proc. Natl. Acad. Sci. U. S. A.* **2015**, *112* (41), 12758–12763.

(131) Majiduddin, F. K.; Palzkill, Timothy. An Analysis of Why Highly Similar Enzymes Evolve Differently. *Genetics* **2003**, *163* (2), 457–466.

(132) Ghuysen, J. Marie. Serine β-Lactamases and Penicillin-Binding Proteins. *Annu. Rev. Microbiol.* **1991**, *45*, 37–67.

(133) Matagne, A.; Lamotte-Brasseur, J.; Frère, J.-M. Catalytic Properties of Class A β-Lactamases: Efficiency and Diversity. *Biochem. J.* **1998**, *330*, 581–598.

(134) Khrenova, M. G.; Nemukhin, A. V. Modeling the Transient Kinetics of the L1 Metallo-β-Lactamase. *J. Phys. Chem. B* **2018**, *122 (4),* 1378-1386.

(135) Azumah, R.; Dutta, J.; Somboro, A. M.; Ramtahal, M.; Chonco, L.; Parboosing, R.; Bester, L. A.; Kruger, H. G.; Naicker, T.; Essack, S. Y.; et al. In Vitro Evaluation of Metal Chelators as Potential Metallo- β-Lactamase Inhibitors. *J. Appl. Microbiol.* **2016**, *120* (4), 860–867.

(136) De Wals, P.-Y.; Doucet, N.; Pelletier, J. N. High Tolerance to Simultaneous Active-Site Mutations in TEM-1 β-Lactamase: Distinct Mutational Paths Provide More Generalized β-Lactam Recognition. *Protein Sci.* **2009**, *18* (1), 147–160.

(137) Bush, Karen. Classification of β-Lactamases: Group 1, 2a, 2b, and 2b'. *Antimicrob. Agents Chemother.* **1989**, *33*, 264–270.

(138) Yang, Y.; Rasmussen, B. A.; Shlaes, D. M. Class A β-Lactamases-Enzyme-Inhibitor Interactions and Resistance. *Pharmacol. Ther.* **1999**, *83*, 141–151.

(139) Vakulenko, S. B.; Geryk, B.; Kotra, L. P.; Mobashery, S.; Lerner, S. A. Selection and Characterization of β-Lactam-β-Lactamase Inactivator-Resistant Mutants Following PCR Mutagenesis of the TEM-1 β-Lactamase Gene. *Antimicrob. Agents Chemother.* **1998**, *42*, 1542–1548.

(140) Huang, W.; Palzkill, Timothy. A Natural Polymorphism in β-Lactamase Is a Global Suppressor. *Proc. Natl. Acad. Sci. U. S. A.* **1997**, *94*, 8801–8806.

(141) Osuna, J.; Perez-Blancas, A.; Soberon, Xavier. Improving a Circularly Permuted TEM-1 β-Lactamase by Directed Evolution. *Protein Eng.* **2002**, *15*, 463–470.

(142) Dellus-Gur, E.; Elias, M.; Caselli, E.; Prati, F.; Salverda, M. L. M.; De Visser, J. A. G. M.; Fraser, J. S.; Tawfik, D. S. Negative Epistasis and Evolvability in TEM-1 β-Lactamase - The Thin Line between an Enzyme's Conformational Freedom and Disorder. *J. Mol. Biol.* **2015**, *427* (14), 2396–2409.

(143) Golemi-Kotra, D.; Meroueh, S. O.; Kim, C.; Vakulenko, S. B.; Bulychev, A.; Stemmler, A. J.; Stemmler, T. L.; Mobashery, Shahriar. The Importance of a Critical Protonation State and the Fate of the Catalytic Steps in Class A β-Lactamases and Penicillin-Binding Proteins. *J. Biol. Chem.* **2004**, *279* (33), 34665–34673.

(144) Minasov, G.; Wang, X.; Shoichet, B. K. An Ultrahigh Resolution Structure of TEM-1 β-Lactamase Suggests a Role for Glu166 as the General Base in Acylation. *J. Am. Chem. Soc.* **2002**, *124* (19), 5333–5340.

(145) Maveyraud, L.; Pratt, R. F.; Samama, J.-Pierre. Crystal Structure of an Acylation Transition-State Analog of the TEM-1 β-Lactamase. Mechanistic Implications for Class A β-Lactamases. *Biochemistry* **1998**, *37* (8), 2622–2628.

(146) Mustafi, D.; Sosa-Peinado, A.; Makinen, M. W. ENDOR Structural Characterization of a Catalytically Competent Acylenzyme Reaction Intermediate of Wild-Type TEM-1 β-Lactamase Confirms Glutamate-166 as the Base Catalyst. *Biochemistry* **2001**, *40* (8), 2397–2409.

(147) Ambler, R. P. The Structure of β-Lactamases. *Philos. Trans. R. Soc. Lond. B. Biol. Sci.* **1980**, *289* (1036), 321–331.

(148) Jelsch, C.; Mourey, L.; Masson, J. M.; Samama, J. P. Crystal Structure of Escherichia Coli TEM1 Beta-Lactamase at 1.8 A Resolution. *Proteins* **1993**, *16* (4), 364–383.

(149) Strynadka, N. C. J.; Adachi, H.; Jensen, S. E.; Johns, K.; Sielecki, A.; Betzel, C.; Sutoh, K.; James, M. N. G. Molecular Structure of the Acyl-Enzyme Intermediate in β-Lactam Hydrolysis at 1.7 Å Resolution. *Nat. Lond. U. K.* **1992**, *359* (6397), 700–705.

(150) Chen, C. C. H.; Herzberg, Osnat. Inhibition of β-Lactamase by Clavulanate. Trapped Intermediates in Cryocrystallographic Studies. *J. Mol. Biol.* **1992**, *224* (4), 1103–1113.

(151) Pimenta, A. C.; Martins, J. M.; Fernandes, R.; Moreira, I. S. Ligand-Induced Structural Changes in TEM-1 Probed by Molecular Dynamics and Relative Binding Free Energy Calculations. *J. Chem. Inf. Model.* **2013**, *53* (10), 2648–2658.

(152) Bowman, G. R.; Geissler, P. L. Equilibrium Fluctuations of a Single Folded Protein Reveal a Multitude of Potential Cryptic Allosteric Sites. *Proc. Natl. Acad. Sci. U. S. A.* **2012**, *109*, 11681–11686.

(153) Horn, J. R.; Shoichet, B. K. Allosteric Inhibition Through Core Disruption. *J. Mol. Biol.* **2004**, *336*, 1283–1291.

(154) Luchini, A.; Espina, V.; Liotta, L. a. Protein Painting Reveals Solvent-Excluded Drug Targets Hidden within Native Protein-Protein Interfaces. *Nat. Commun.* **2014**, *5*, 4413–4413.

(155) Guenebaut, V.; Schlitt, A.; Weiss, H.; Leonard, K.; Friedrich, Thorsten. Consistent Structure between Bacterial and Mitochondrial NADH-Ubiquinone Oxidoreductase (Complex I). *J. Mol. Biol.* **1998**, *276*, 105–112.

(156) Nixon, J. E. J.; Wang, A.; Field, J.; Morrison, H. G.; McArthur, A. G.; Sogin, M. L.; Loftus, B. J.; Samuelson, John. Evidence for Lateral Transfer of Genes Encoding Ferredoxins, Nitroreductases, NADH Oxidase, and Alcohol Dehydrogenase 3 from Anaerobic Prokaryotes to Giardia Lamblia and Entamoeba Histolytica. *Eukaryot. Cell* **2002**, *1*, 181–190.

(157) Thoden, J. B.; Frey, P. A.; Holden, H. M. Molecular Structure of the NADH/UDP-Glucose Abortive Complex of UDP-Galactose 4-Epimerase from Escherichia Coli: Implications for the Catalytic Mechanism. *Biochemistry* **1996**, *35*, 5137–5144.

(158) Belenky, P.; Bogan, K. L.; Brenner, C. NAD+ Metabolism in Health and Disease. *Trends Biochem. Sci.* **2007**, *32* (1), 12–19.

(159) Harden Arthur; Young William John; Martin Charles James. The Alcoholic Ferment of Yeast-Juice. *Proc. R. Soc. Lond. Ser. B Contain. Pap. Biol. Character* **1906**, *77* (519), 405–420.

(160) Warburg, O.; Christian, Walter. Pyridine, the Hydrogen-Transferring Component of the Fermentation Enzymes. (Pyridine Nucleotide). *Biochem. Z.* **1936**, *287*, 291–328.

(161) Warburg, O.; Christian, W.; Griese, Alfred. Hydrogen-Transferring Coenzyme, Its Composition and Mode of Action. *Biochem. Z.* **1935**, *282*, 157–205.

(162) Williamson, D. H.; Lund, P.; Krebs, H. A. The Redox State of Free Nicotinamide-Adenine Dinucleotide in the Cytoplasm and Mitochondria of Rat Liver. *Biochem. J.* **1967**, *103* (2), 514–527.

(163) Lesk, A. M. NAD-Binding Domains of Dehydrogenases. *Curr. Opin. Struct. Biol.* **1995**, *5* (6), 775–783.

(164) Bahnson, B. J.; Colby, T. D.; Chin, J. K.; Goldstein, B. M.; Klinman, J. P. A Link between Protein Structure and Enzyme Catalyzed Hydrogen Tunneling. *Proc. Natl. Acad. Sci. U. S. A.* **1997**, *94*, 12797–12802.

(165) Raj, S. B.; Ramaswamy, S.; Plapp, B. V. Yeast Alcohol Dehydrogenase Structure and Catalysis. *Biochemistry* **2014**, *53*, 5791–5803.

(166) Bennetzen, J. L.; Hall, B. D. The Primary Structure of the Saccharomyces Cerevisiae Gene for Alcohol Dehydrogenase. *J. Biol. Chem.* **1982**, *257*, 3018–3025.

(167) Kleifeld, O.; Frenkel, A.; Martin, J. M. L.; Sagi, I. Active Site Electronic Structure and Dynamics during Metalloenzyme Catalysis. *Nat. Struct. Biol.* **2003**, *10*, 98–103.

(168) Klinman, J. P. An Integrated Model for Enzyme Catalysis Emerges from Studies of Hydrogen Tunneling. *Chem. Phys. Lett.* **2009**, *471*, 179–193.

(169) Pauling, Linus. Molecular Architecture and Biological Reactions. *Chem. Eng. News* **1946**, *24*, 1375–1377.

(170) Schramm, V. L. Enzymatic Transition State Theory and Transition State Analogue Design. *J. Biol. Chem.* **2007**, *282*, 28297–28300.

(171) Nagel, Z. D.; Klinman, J. P. Tunneling and Dynamics in Enzymatic Hydride Transfer. *Chem. Rev. Wash. DC U. S.* **2006**, *106*, 3095–3118.

(172) Meadows, C. W.; Balakrishnan, G.; Kier, B. L.; Spiro, T. G.; Klinman, J. P. Temperature-Jump Fluorescence Provides Evidence for Fully Reversible Microsecond Dynamics in a Thermophilic Alcohol Dehydrogenase. *J. Am. Chem. Soc.* **2015**, *137*, 10060–10063.

(173) Nagel, Z. D.; Meadows, C. W.; Dong, M.; Bahnson, B. J.; Klinman, J. P. Active Site Hydrophobic Residues Impact Hydrogen Tunneling Differently in a Thermophilic Alcohol Dehydrogenase at Optimal versus Nonoptimal Temperatures. *Biochemistry* **2012**, *51,* 4147–4156.

(174) Cha, Y.; Murray, C. J.; Klinman, J. P. Hydrogen Tunneling in Enzyme Reactions. *Sci. Wash. DC U. S.* **1989**, *243*, 1325–1330.

(175) Rubach, J. K.; Plapp, B. V. Amino Acid Residues in the Nicotinamide Binding Site Contribute to Catalysis by Horse Liver Alcohol Dehydrogenase. *Biochemistry* **2003**, *42*, 2907–2915.

(176) Northrop, D. B. Uses of Isotope Effects in the Study of Enzymes. *Methods San Diego CA U. S.* **2001**, *24*, 117–124.

(177) Chin, J. K.; Klinman, J. P. Probes of a Role for Remote Binding Interactions on Hydrogen Tunneling in the Horse Liver Alcohol Dehydrogenase Reaction. *Biochemistry* **2000**, *39*, 1278–1284.

(178) Liuni, P.; Olkhov-Mitsel, E.; Orellana, A.; Wilson, D. J. Measuring Kinetic Isotope Effects in Enzyme Reactions Using Time-Resolved Electrospray Mass Spectrometry. *Anal. Chem. Wash. DC U. S.* **2013**, *85*, 3758–3764.

(179) Alhambra, C.; Corchado, J. C.; Sanchez, M. L.; Gao, J.; Truhlar, D. G. Quantum Dynamics of Hydride Transfer in Enzyme Catalysis. *J. Am. Chem. Soc.* **2000**, *122*, 8197–8203.

(180) Cho, Y.-K.; Northrop, D. B. Effects of Pressure on the Kinetics of Capture by Yeast Alcohol Dehydrogenase. *Biochemistry* **1999**, *38*, 7470–7475.

(181) Dickinson, F. M.; Monger, G. P. Kinetics and Mechanism of Yeast Alcohol Dehydrogenase with a Variety of Substrates. *Biochem. J.* **1973**, *131*, 261–270.

(182) Martin, M. T.; Waley, S. G. Kinetic Characterization of the Acyl-Enzyme Mechanism for Beta-Lactamase I. *Biochem. J.* **1988**, *254*, 923–925.

(183) Imtiaz, U.; Manavathu, E. K.; Lerner, S. A.; Mobashery, Shahriar. Critical Hydrogen Bonding by Serine 235 for Cephalosporinase Activity of TEM-1 β-Lactamase. *Antimicrob. Agents Chemother.* **1993**, *37* (11), 2438–2442.

(184) Dubus, A.; Wilkin, J.-M.; Raquet, X.; Normark, S.; Frere, J.-Marie. Catalytic Mechanism of Active-Site Serine β-Lactamases: Role of the Conserved Hydroxy Group of the Lys-Thr(Ser)-Gly Triad. *Biochem. J.* **1994**, *301*, 485–494.

(185) Bratulic, S.; Gerber, F.; Wagner, A. Mistranslation Drives the Evolution of Robustness in TEM-1 β-Lactamase. *Proc. Natl. Acad. Sci.* **2015**, *112* (41), 201510071.

(186) Matagne, A.; Misselyn-Bauduin, A. M.; Joris, B.; Erpicum, T.; Granier, B.; Frere, J. Marie. The Diversity of the Catalytic Properties of Class A β-Lactamases. *Biochem. J.* **1990**, *265*, 131–146. 1.

(187) Sulton, D.; Pagan-Rodriguez, D.; Zhou, X.; Liu, Y.; Hujer, A. M.; Bethel, C. R.; Helfand, M. S.; Thomson, J. M.; Anderson, V. E.; Buynak, J. D.; et al. Clavulanic Acid Inactivation of SHV-1 and the Inhibitor-Resistant S130G SHV-1 β-Lactamase: Insights into the Mechanism of Inhibition. *J. Biol. Chem.* **2005**, *280*, 35528–35536.

(188) Deng, B.; Zhu, S.; Macklin, A. M.; Xu, J.; Lento, C.; Sljoka, A.; Wilson, D. J. Suppressing Allostery in Epitope Mapping Experiments Using Millisecond Hydrogen / Deuterium Exchange Mass Spectrometry. *mAbs* **2017**, *9*, 1327–1336.

(189) Rob, T.; Liuni, P.; Gill, P. K.; Zhu, S.; Balachandran, N.; Berti, P. J.; Wilson, D. J. Measuring Dynamics in Weakly Structured Regions of Proteins Using Microfluidics-Enabled Subsecond H/D Exchange Mass Spectrometry. *Anal. Chem.* **2012**, *84* (8), 3771–3779.

(190) Reddington, S. C.; Howarth, Mark. Secrets of a Covalent Interaction for Biomaterials and Biotechnology: SpyTag and SpyCatcher. *Curr. Opin. Chem. Biol.* **2015**, *29*, 94–99.

(191) Knowles, J. R. Penicillin Resistance: The Chemistry of β-Lactamase Inhibition. *Acc. Chem. Res.* **1985**, *18* (4), 97–104.

(192) Brenner, D. G.; Knowles, J. R. 6-(Methoxymethylene)Penicillanic Acid: Inactivator of RTEM β-Lactamase from Escherichia Coli. *Biochemistry* **1984**, *23*, 5839–5846.

(193) Imtiaz, U.; Billings, E.; Knox, J. R.; Manavathu, E. K.; Lerner, S. A.; Mobashery, Shahriar. Inactivation of Class A β-Lactamases by Clavulanic Acid: The Role of Arginine-244 in a Proposed Nonconcerted Sequence of Events. *J. Am. Chem. Soc.* **1993**, *115*, 4435–4442.

(194) Brown, R. P. A.; Aplin, R. T.; Schofield, C. J. Inhibition of TEM-2 β-Lactamase from Escherichia Coli by Clavulanic Acid: Observation of Intermediates by Electrospray Ionization Mass Spectrometry. *Biochemistry* **1996**, *35*, 12421–12432.

(195) Drawz, S. M.; Bonomo, R. A. Three Decades of β-Lactamase Inhibitors. *Clin. Microbiol. Rev.* **2010**, *23*, 160–201.

(196) Li, Z.; Song, F.; Zhuang, Z.; Dunaway-Mariano, D.; Anderson, K. S. Monitoring Enzyme Catalysis in the Multimeric State: Direct Observation of Arthrobacter 4-Hydroxybenzoyl-Coenzyme A Thioesterase Catalytic Complexes Using Time-Resolved Electrospray Ionization Mass Spectrometry. *Anal. Biochem.* **2009**, *394*, 209–216.

(197) Horn, J. R.; Shoichet, B. K. Allosteric Inhibition Through Core Disruption. *J. Mol. Biol.* **2004**, *336* (5), 1283–1291.

(198) Zafaralla, G.; Manavathu, E. K.; Lerner, S. A.; Mobashery, Shahriar. Elucidation of the Role of Arginine-224 in the Turnover Processes of Class A β-Lactamases. *Biochemistry* **1992**, *31* (15), 3847–3852.

(199) Brown, N. G.; Shanker, S.; Prasad, B. V. V.; Palzkill, Timothy. Structural and Biochemical Evidence That a TEM-1 β-Lactamase N170G Active Site Mutant Acts via Substrate-Assisted Catalysis. *J. Biol. Chem.* **2009**, *284* (48), 33703–33712.

(200) Moews, P. C.; Knox, J. R.; Dideberg, O.; Charlier, P.; Frere, J. Marie. β-Lactamase of Bacillus Licheniformis 749/C at 2 Å Resolution. *Proteins Struct. Funct. Genet.* **1990**, *7*, 156–171.

(201) Salverda, M. L. M.; De, V. J. A. G. M.; Barlow, M. Natural Evolution of TEM-1 β-Lactamase: Experimental Reconstruction and Clinical Relevance. *FEMS Microbiol. Rev.* **2010**, *34*, 1015–1036.

(202) Chaibi, E. B.; Sirot, D.; Paul, G.; Labia, R. Inhibitor-Resistant TEM β-Lactamases: Phenotypic, Genetic and Biochemical Characteristics. *J. Antimicrob. Chemother.* **1999**, *43*, 447–458.

(203) Matagne, A.; Lamotte-Brasseur, J.; Frere, J.-Marie. Catalytic Properties of Class A β-Lactamases: Efficiency and Diversity. *Biochem. J.* **1998**, *330* (2), 581–598.

(204) Mira, P. M.; Meza, J. C.; Nandipati, A.; Barlow, Miriam. Adaptive Landscapes of Resistance Genes Change as Antibiotic Concentrations Change. *Mol. Biol. Evol.* **2015**, *32*, 2707–2715.

(205) Wiesmann, C.; Barr, K. J.; Kung, J.; Zhu, J.; Erlanson, D. A.; Shen, W.; Fahr, B. J.; Zhong, M.; Taylor, L.; Randal, M.; et al. Allosteric Inhibition of Protein Tyrosine Phosphatase 1B. *Nat. Struct. Mol. Biol.* **2004**, *11*, 730–737.

(206) Hardy, J. A.; Lam, J.; Nguyen, J. T.; O'Brien, T.; Wells, J. A. Discovery of an Allosteric Site in the Caspases. *Proc. Natl. Acad. Sci. U. S. A.* **2004**, *101*, 12461–12466.

(207) Wellington, S.; Nag, P. P.; Johnston, S. E.; Kaushik, V. K.; McCarren, P.; Bajrami, B.; Fisher, S. L.; Schreiber, S. L.; Hung, D. T.; Wellington, S.; et al. A Small-Molecule Allosteric Inhibitor of Mycobacterium Tuberculosis Tryptophan Synthase. *Nat. Chem. Biol.* **2017**, *13*, 943–950.

(208) Fast, C. S.; Vahidi, S.; Konermann, L. Changes in Enzyme Structural Dynamics Studied by Hydrogen Exchange-Mass Spectrometry: Ligand Binding Effects or Catalytically Relevant Motions? *Anal. Chem.* **2017**, *89* (24), 13326–13333.

(209) Chakrabarti, K. S.; Agafonov, R. V.; Pontiggia, F.; Otten, R.; Higgins, M. K.; Schertler, G. F. X.; Oprian, D. D.; Kern, Dorothee. Conformational Selection in a Protein-Protein Interaction Revealed by Dynamic Pathway Analysis. *Cell Rep.* **2016**, *14*, 32–42.

(210) Weikl, T. R.; Paul, Fabian. Conformational Selection in Protein Binding and Function. *Protein Sci.* **2014**, *23*, 1508–1518.

(211) Vallurupalli, P.; Sekhar, A.; Yuwen, T.; Kay, L. E. Probing Conformational Dynamics in Biomolecules via Chemical Exchange Saturation Transfer: A Primer. *J. Biomol. NMR* **2017**, *67* (4), 243–271.

(212) Rob, T.; Gill, P. K.; Golemi-Kotra, D.; Wilson, D. J. An Electrospray Ms-Coupled Microfluidic Device for Sub-Second Hydrogen/Deuterium Exchange Pulse-Labelling Reveals Allosteric Effects in Enzyme Inhibition. *Lab. Chip* **2013**, *13* (13), 2528–2532.

(213) Brown, K. A.; Sharifi, S.; Hussain, R.; Donaldson, L.; Bayfield, M. A.; Wilson, D. J. Distinct Dynamic Modes Enable the Engagement of Dissimilar Ligands in a Promiscuous Atypical RNA Recognition Motif. *Biochemistry* **2016**, *55* (51), 7141–7150.

(214) Jacoby, G. A.; Carreras, Isabel. Activities of β-Lactam Antibiotics against Escherichia Coli Strains Producing Extended-Spectrum β-Lactamases. *Antimicrob. Agents Chemother.* **1990**, *34* (5), 858–862.

(215) Bret, L.; Chaibi, E. B.; Chanal-Claris, C.; Sirot, D.; Labia, R.; Sirot, J. Inhibitor-Resistant TEM (IRT) β-Lactamases with Different Substitutions at Position 244. *Antimicrob. Agents Chemother.* **1997**, *41*, 2547–2549.

(216) Bush, K.; Macalintal, C.; Rasmussen, B. A.; Lee, V. J.; Yang, Youjun. Kinetic Interactions of Tazobactam with β-Lactamases from All Major Structural Classes. *Antimicrob. Agents Chemother.* **1993**, *37*, 851–858.

(217) Teleb, M.; Soto-Ruiz, E.; Dominguez, D. C.; Antony, Suresh. ESBL E Coli and P. Aeruginosa Resistance to Ceftolozane-Tazobactam in a Patient with a Liver Abscess. The Search for an Omnipotent Antibiotic Goes On!. *Infect. Disord. Drug Targets* **2018**, *18*, 81–85.

(218) Papp-Wallace, K. M.; Bethel, C. R.; Distler, A. M.; Kasuboski, C.; Taracila, M.; Bonomo, R. A. Inhibitor Resistance in the KPC-2 β-Lactamase, a Preeminent Property of This Class A β-Lactamase. *Antimicrob. Agents Chemother.* **2010**, *54*, 890–897.

(219) Danishuddin, Mohd.; Khan, A.; Faheem, M.; Kalaiarasan, P.; Hassan Baig, Mohd.; Subbarao, N.; Khan, A. U. Structure-Based Screening of Inhibitors against KPC-2: Designing Potential Drug Candidates against Multidrug-Resistant Bacteria. *J. Biomol. Struct. Dyn.* **2014**, *32*, 741–750.

(220) Yang, Y.; Janota, K.; Tabei, K.; Huang, N.; Siegel, M. M.; Lin, Y.-I.; Rasmussen, B. A.; Shlaes, D. M. Mechanism of Inhibition of the Class A β-Lactamases PC1 and TEM-1 by Tazobactam. Observation of Reaction Products by Electrospray Ionization Mass Spectrometry. *J. Biol. Chem.* **2000**, *275*, 26674–26682.

(221) Kuzin, A. P.; Nukaga, M.; Nukaga, Y.; Hujer, A.; Bonomo, R. A.; Knox, J. R. Inhibition of the SHV-1 β-Lactamase by Sulfones: Crystallographic Observation of Two Reaction Intermediates with Tazobactam. *Biochemistry* **2001**, *40*, 1861–1866.

(222) Rodkey, E. A.; Winkler, M. L.; Bethel, C. R.; Pagadala, S. R. R.; Buynak, J. D.; Bonomo, R. A.; van den Akker, Focco. Penam Sulfones and β-Lactamase Inhibition: SA2-13 and the Importance of the C2 Side Chain Length and Composition. *PLoS One* **2014**, *9*, e85892/1-e85892/11.

(223) Rob, T.; Gill, P. K.; Golemi-Kotra, D.; Wilson, D. J. An Electrospray Ms-Coupled Microfluidic Device for Sub-Second Hydrogen/Deuterium Exchange Pulse-Labelling Reveals Allosteric Effects in EnzRob, T., Gill, P. K., Golemi-Kotra, D., & Wilson, D. J. (2013). An Electrospray Ms-Coupled Microfluidic Device for s. *Lab. Chip* **2013**, *13* (13), 2528–2532.

(224) Pike, S. D.; Pernik, I.; Theron, R.; McIndoe, J. S.; Weller, A. S. Relative Binding Affinities of Fluorobenzene Ligands in Cationic Rhodium Bisphosphine H6-Fluorobenzene Complexes Probed Using Collision-Induced Dissociation. *J. Organomet. Chem.* **2015**, *784*, 75–83.

(225) Zhong, Y.; Han, L.; Ruotolo, B. T. Collisional and Coulombic Unfolding of Gas-Phase Proteins: High Correlation to Their Domain Structures in Solution. *Angew. Chem. Int. Ed.* **2014**, *53*, 9209–9212.

(226) Rob, T.; Gill, P. K.; Golemi-Kotra, D.; Wilson, D. J. An Electrospray Ms-Coupled Microfluidic Device for Sub-Second Hydrogen/Deuterium Exchange Pulse-Labelling Reveals Allosteric Effects in EnzRob, T., Gill, P. K., Golemi-Kotra, D., & Wilson, D. J. (2013). An Electrospray Ms-Coupled Microfluidic Device for s. *Lab. Chip* **2013**, *13* (13), 2528–2532.

(227) Tabei, K.; Feng, X.; Venkatesan, A. M.; Abe, T.; Hideki, U.; Mansour, T. S.; Siegel, M. M. Mechanism of Inactivation of β-Lactamases by Novel 6-Methylidene Penems Elucidated Using Electrospray Ionization Mass Spectrometry. *J. Med. Chem.* **2004**, *47*, 3674–3688.

(228) Endimiani, A.; Doi, Y.; Bethel, C. R.; Taracila, M.; Adams-Haduch, J. M.; O'Keefe, A.; Hujer, A. M.; Paterson, D. L.; Skalweit, M. J.; Page, M. G. P.; et al. Enhancing Resistance to Cephalosporins in Class C β-Lactamases: Impact of Gly214Glu in CMY-2. *Biochemistry* **2010**, *49*, 1014–1023.

(229) Hugonnet, J.-E.; Blanchard, J. S. Irreversible Inhibition of the Mycobacterium Tuberculosis β-Lactamase by Clavulanate. *Biochemistry* **2007**, *46*, 11998–12004.

(230) Ferguson, P. L.; Konermann, Lars. Nonuniform Isotope Patterns Produced by Collision-Induced Dissociation of Homogeneously Labeled Ubiquitin: Implications for Spatially Resolved Hydrogen/Deuterium Exchange ESI-MS Studies. *Anal. Chem. Wash. DC U. S.* **2008**, *80*, 4078–4086.

(231) Bush, K.; Jacoby, G. A. Updated Functional Classification of β-Lactamases. *Antimicrob. Agents Chemother.* **2010**, *54* (3), 969–976.

(232) Imtiaz, U.; Manavathu, E. K.; Mobashery, S.; Lerner, S. A. Reversal of Clavulanate Resistance Conferred by a Ser-244 Mutant of TEM-1 Beta-Lactamase as a Result of a Second Mutation (Arg to Ser at Position 164) That Enhances Activity against Ceftazidime. *Antimicrob. Agents Chemother.* **1994**, *38*, 1134–1139.

(233) Delaire, M.; Lenfant, F.; Labia, R.; Masson, J. Michel. Site-Directed Mutagenesis on TEM-1 β-Lactamase: Role of Glu166 in Catalysis and Substrate Binding. *Protein Eng.* **1991**, *4* (7), 805–810.

(234) Strohalm, M.; Kavan, D.; Novak, P.; Volny, M.; Havlicek, Vladimir. MMass 3: A Cross-Platform Software Environment for Precise Analysis of Mass Spectrometric Data. *Anal. Chem. Wash. DC U. S.* **2010**, *82*, 4648–4651.

(235) Rey, M.; Sarpe, V.; Burns, K.; Buse, J.; Baker, C. A. H.; van Dijk, M.; Wordeman, L.; Bonvin, A. M. J. J.; Schriemer, D. C. Mass Spec Studio for Integrative Structural Biology. *Struct. Oxf. U. K.* **2014**, *22*, 1538–1548.

(236) Otten, R.; Villali, J.; Kern, D.; Mulder, F. A. A. Probing Microsecond Time Scale Dynamics in Proteins by Methyl (1)H Carr−Purcell−Meiboom−Gill Relaxation Dispersion NMR Measurements. Application to Activation of the Signaling Protein NtrC(r). *J. Am. Chem. Soc.* **2010**, *132* (47), 17004–17014.

(237) Jornvall, H.; Eklund, H.; Branden, C. Ivar. Subunit Conformation of Yeast Alcohol Dehydrogenase. *J. Biol. Chem.* **1978**, *253*, 8414–8419.

(238) Hayes, J. E., Jr.; Velick, S. F. Yeast Alcohol Dehydrogenase: Molecular Weight, Coenzyme Binding, and Reaction Equilibria. *J. Biol. Chem.* **1954**, *207*, 225–244.

(239) Trivic, S.; Leskovac, Vladimir. Structure and Function of Yeast Alcohol Dehydrogenase. *J. Serbian Chem. Soc.* **2000**, *65*, 207–227.

(240) Wills, C.; Joernvall, Hans. The Two Major Isozymes of Yeast Alcohol Dehydrogenase. *Eur. J. Biochem.* **1979**, *99*, 323–331.

(241) Wills, Christopher. Production of Yeast Alcohol Dehydrogenase Isoenzymes by Selection. *Nat. Lond. U. K.* **1976**, *261*, 26–29.

(242) Magonet, E.; Hayen, P.; Delforge, D.; Delaive, E.; Remacle, Jose. Importance of the Structural Zinc Atom for the Stability of Yeast Alcohol Dehydrogenase. *Biochem. J.* **1992**, *287*, 361–365.

(243) Kagi, J. H. R.; Vallee, B. L. Role of Zinc in Alcohol Dehydrogenase. V. Effect of Metal-Binding Agents on the Structure of the Yeast Alcohol Dehydrogenase Molecule. *J. Biol. Chem.* **1960**, *235*, 3188–3192.

(244) Li, H.; Wongkongkathep, P.; Van, O. S. L.; Ogorzalek, L. R. R.; Loo, J. A. Revealing Ligand Binding Sites and Quantifying Subunit Variants of Noncovalent Protein Complexes in a Single Native Top-down FTICR MS Experiment. *J. Am. Soc. Mass Spectrom.* **2014**, *25*, 2060–2068.

(245) Bhuiya, S.; Haque, L.; Pradhan, A. B.; Das, Suman. Inhibitory Effects of the Dietary Flavonoid Quercetin on the Enzyme Activity of Zinc(II)-Dependent Yeast Alcohol Dehydrogenase: Spectroscopic and Molecular Docking Studies. *Int. J. Biol. Macromol.* **2017**, *95*, 177–184.

(246) Kim, K.; Plapp, B. V. Substitution of Cysteine-153 Ligated to the Catalytic Zinc in Yeast Alcohol Dehydrogenase with Aspartic Acid and Analysis of Mechanisms of Related Medium Chain Dehydrogenases. *Chem. Biol. Interact.* **2019**, *302*, 172–182.

(247) Santra, M. K.; Dasgupta, D.; Panda, Dulal. Pyrene Excimer Fluorescence of Yeast Alcohol Dehydrogenase: A Sensitive Probe to Investigate Ligand Binding and Unfolding Pathway of the Enzyme. *Photochem. Photobiol.* **2006**, *82*, 480–486.

(248) Plapp, B. V.; Charlier, H. A., Jr.; Ramaswamy, S. Mechanistic Implications from Structures of Yeast Alcohol Dehydrogenase Complexed with Coenzyme and an Alcohol. *Arch. Biochem. Biophys.* **2016**, *591*, 35–42.

(249) Yang, Y.; Zhou, H.-M. Effect of Zinc Ions on Conformational Stability of Yeast Alcohol Dehydrogenase. *Biochem. Mosc. Russ. Fed. Biokhimiya Mosc. Russ. Fed.* **2001**, *66*, 47–54.

(250) Balestrieri, C.; Colonna, G.; Irace, Gaetano. Amino Acid Sequence around a Reactive Cysteine of Yeast Alcohol Dehydrogenase. *Biochem. Biophys. Res. Commun.* **1975**, *66*, 900–906.

(251) Klinman, J. P.; Welsh, Katherine. The Zinc Content of Yeast Alcohol Dehydrogenase. *Biochem. Biophys. Res. Commun.* **1976**, *70*, 878–884.

(252) Liang, Z.-X.; Lee, T.; Resing, K. A.; Ahn, N. G.; Klinman, J. P. Thermal-Activated Protein Mobility and Its Correlation with Catalysis in Thermophilic Alcohol Dehydrogenase. *Proc. Natl. Acad. Sci. U. S. A.* **2004**, *101*, 9556–9561.

(253) Ganzhorn, A. J.; Plapp, B. V. Carboxyl Groups near the Active Site Zinc Contribute to Catalysis in Yeast Alcohol Dehydrogenase. *J. Biol. Chem.* **1988**, *263*, 5446–5454.

(254) Park, H.; Girdaukas, G. G.; Northrop, D. B. Effect of Pressure on a Heavy-Atom Isotope Effect of Yeast Alcohol Dehydrogenase. *J. Am. Chem. Soc.* **2006**, *128*, 1868–1872.

(255) Dickinson, F. M.; Monger, G. P. A Study of the Kinetics and Mechanism of Yeast Alcohol Dehydrogenase with a Variety of Substrates. *Biochem. J.* **1973**, *131* (2), 261–270.

(256) Leskovac, V.; Trivic, S.; Pericin, D.; Popovic, M.; Kandrac, Julijan. Binding of Coenzymes to Yeast Alcohol Dehydrogenase. *J. Serbian Chem. Soc.* **2010**, *75*, 185–194.

(257) Green, D. W.; Sun, H. W.; Plapp, B. V. Inversion of the Substrate Specificity of Yeast Alcohol Dehydrogenase. *J. Biol. Chem.* **1993**, *268*, 7792–7798.

(258) Chew, A. D.; Cameron, A.; Goodwin, D.; Hamilton, J.; Hawley-Jones, T.; Meares, P.; Pumfrey, J.; Ramsden, J.; Steele, D. *Considerations for Primary Vacuum Pumping in Mass Spectrometry Systems*; 2005; Vol. 20.

(259) Zhang, H.; Cui, W.; Wen, J.; Blankenship, R. E.; Gross, M. L. Native Electrospray and Electron-Capture Dissociation in FTICR Mass Spectrometry Provide Top-Down Sequencing of a Protein Component in an Intact Protein Assembly. *J. Am. Soc. Mass Spectrom.* **2010**, *21*, 1966–1968.

(260) Antoniou, D.; Schwartz, S. D. Internal Enzyme Motions as a Source of Catalytic Activity: Rate-Promoting Vibrations and Hydrogen Tunneling. *J. Phys. Chem. B* **2001**, *105*, 5553–5558.

(261) Pucciarelli, S.; Bonacucina, G.; Bernabucci, F.; Cespi, M.; Mencarelli, G.; Fronzo, G. S.; Natalini, P.; Palmieri, G. Filippo. A Study on the Stability and Enzymatic Activity of Yeast Alcohol Dehydrogenase in Presence of the Self-Assembling Block Copolymer Poloxamer 407. *Appl. Biochem. Biotechnol.* **2012**, *167*, 298–313.

(262) De, W. Z.; Pande, J.; Kagi, J. H. Interdependence of Coenzyme-Induced Conformational Work and Binding Potential in Yeast Alcohol and Porcine Heart Lactate Dehydrogenases: A Hydrogen-Deuterium Exchange Study. *Biochemistry* **1987**, *26*, 4769–4776.

(263) Fan, F.; Lorenzen, J. A.; Plapp, B. V. An Aspartate Residue in Yeast Alcohol Dehydrogenase I Determines the Specificity for Coenzyme. *Biochemistry* **1991**, *30*, 6397–6401.

(264) Cai, W.; Wang, E.; Chen, P.-W.; Tsai, Y.-H.; Langouche, L.; Lo, Y.-Hwa. A Microfluidic Design for Desalination and Selective Removal and Addition of Components in Biosamples. *Biomicrofluidics* **2019**, No. Copyright (C) 2019 American Chemical Society (ACS). All Rights Reserved., Ahead of Print.

(265) Asghar, W.; Sher, M.; Khan, N. S.; Vyas, J. M.; Demirci, Utkan. Microfluidic Chip for Detection of Fungal Infections. *ACS Omega* **2019**, *4*, 7474–7481.

(266) Patra, B.; Lafontaine, J.; Bavoux, M.; Zerouali, K.; Glory, A.; Ahanj, M.; Carrier, J.-F.; Gervais, T.; Wong, Philip. On-Chip Combined Radiotherapy and Chemotherapy Testing on Soft-Tissue Sarcoma Spheroids to Study Cell Death Using Flow Cytometry and Clonogenic Assay. *Sci. Rep.* **2019**, *9*, 1–9.

(267) Bae, C. W.; Toi, P. T.; Kim, B. Y.; Lee, W. I.; Lee, H. B.; Hanif, A.; Lee, E. H.; Lee, N.-Eung. Fully Stretchable Capillary Microfluidics-Integrated Nanoporous Gold Electrochemical Sensor for Wearable Continuous Glucose Monitoring. *ACS Appl. Mater. Interfaces* **2019**, *11*, 14567–14575.

(268) Hoffmann, Jochen. Low-Reactivity for a Microfluidic Device and Process for the Determination of a Nucleotide Sequence [Machine Translation]., April 25, 2019.

(269) Yager, P.; Edwards, T.; Fu, E.; Helton, K.; Nelson, K.; Tam, M. R.; Weigl, B. H. Microfluidic Diagnostic Technologies for Global Public Health. *Nat. Lond. U. K.* **2006**, *442*, 412–418.

(270) Sacks, D.; Noben-Trauth, Nancy. The Immunology of Susceptibility and Resistance to Leishmania Major in Mice. *Nat. Rev. Immunol.* **2002**, *2*, 845–858.

(271) Kaye, P.; Scott, Phillip. Leishmaniasis: Complexity at the Host-Pathogen Interface. *Nat. Rev. Microbiol.* **2011**, *9*, 604–615.

(272) Croft, S. L.; Sundar, S.; Fairlamb, A. H. Drug Resistance in Leishmaniasis. *Clin. Microbiol. Rev.* **2006**, *19*, 111–126.

(273) Ovalle-Bracho, C.; Londono-Barbosa, D.; Salgado-Almario, J.; Gonzalez, Camila. Evaluating the Spatial Distribution of Leishmania Parasites in Colombia from Clinical Samples and Human Isolates (1999 to 2016). *PLoS One* **2019**, *14*, e0214124.

(274) Terreros, M. J. S.; de Luna, L. A. V.; Giorgio, Selma. Evaluation of Antileishmanial Drugs Activities in an Ex Vivo Model of Leishmaniasis. *Parasitol. Int.* **2019**, *71*, 163–166.

(275) Olivier, M.; Gregory, D. J.; Forget, Genevieve. Subversion Mechanisms by Which Leishmania Parasites Can Escape the Host Immune Response: A Signaling Point of View. *Clin. Microbiol. Rev.* **2005**, *18*, 293–305.

(276) Ouellette, M.; Drummelsmith, J.; Papadopoulou, Barbara. Leishmaniasis: Drugs in the Clinic, Resistance and New Developments. *Drug Resist. Updat.* **2004**, *7*, 257–266.

(277) Alves, C. R.; Souza, R. S. de; Charret, K. dos S.; Cortes, L. M. de C.; Sa-Silva, M. P. de; Barral-Veloso, L.; Oliveira, L. F. G.; da Silva, F. Souza. Understanding Serine Proteases Implications on Leishmania Spp Lifecycle. *Exp. Parasitol.* **2018**, *184*, 67–81.

(278) Subramanian, A.; Sarkar, R. R. Perspectives on Leishmania Species and Stage-Specific Adaptive Mechanisms. *Trends Parasitol.* **2018**, *34*, 1068–1081.

(279) McDonald, J. C.; Whitesides, G. M. Poly(Dimethylsiloxane) as a Material for Fabricating Microfluidic Devices. *Acc. Chem. Res.* **2002**, *35*, 491–499.

(280) Xu, S.; Nie, Z.; Seo, M.; Lewis, P.; Kumacheva, E.; Stone, H. A.; Garstecki, P.; Weibel, D. B.; Gitlin, I.; Whitesides, G. M. Generation of Monodisperse Particles by Using Microfluidics: Control over Size, Shape, and Composition. *Angew. Chem. Int. Ed.* **2005**, *44*, 724–728.

(281) El-Ali, J.; Sorger, P. K.; Jensen, K. F. Cells on Chips. *Nat. Lond. U. K.* **2006**, *442*, 403–411.

(282) Huber, D. L.; Manginell, R. P.; Samara, M. A.; Kim, B.-I.; Bunker, B. C. Programmed Adsorption and Release of Proteins in a Microfluidic Device. *Sci. Wash. DC U. S.* **2003**, *301*, 352–354.

Appendix A

Supplemental Figures for Chapter 2

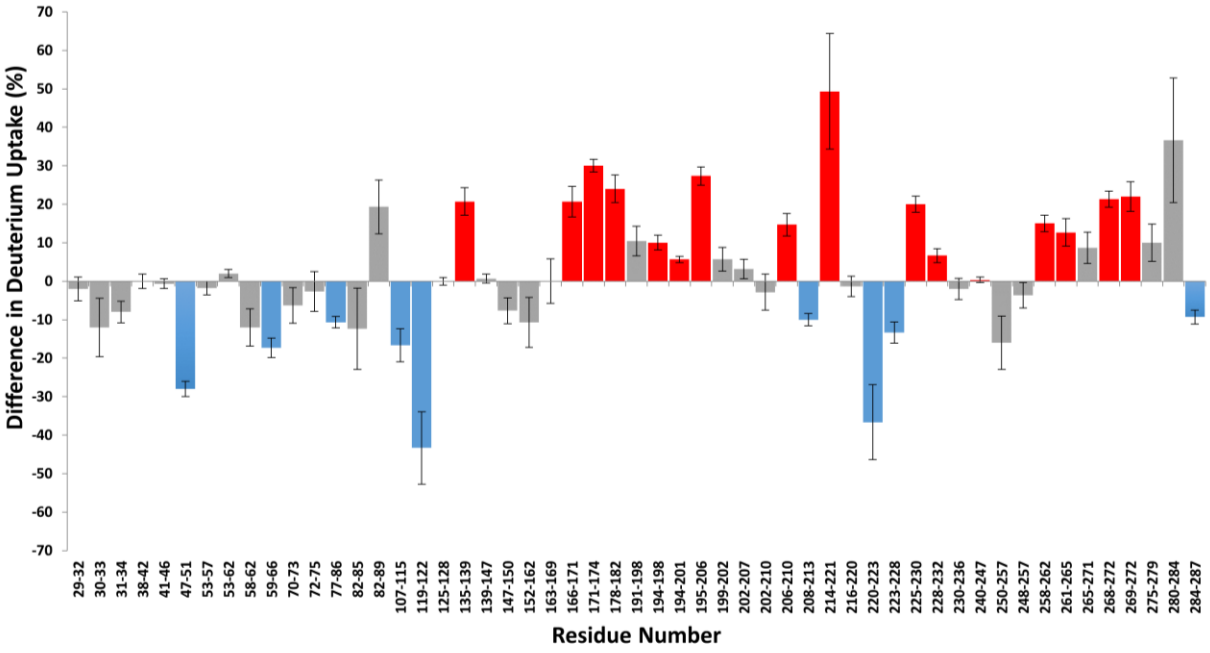

Supplemental Figure A1 Equilibrated Local HDX Coverage for TEM-1 with Ampicillin.

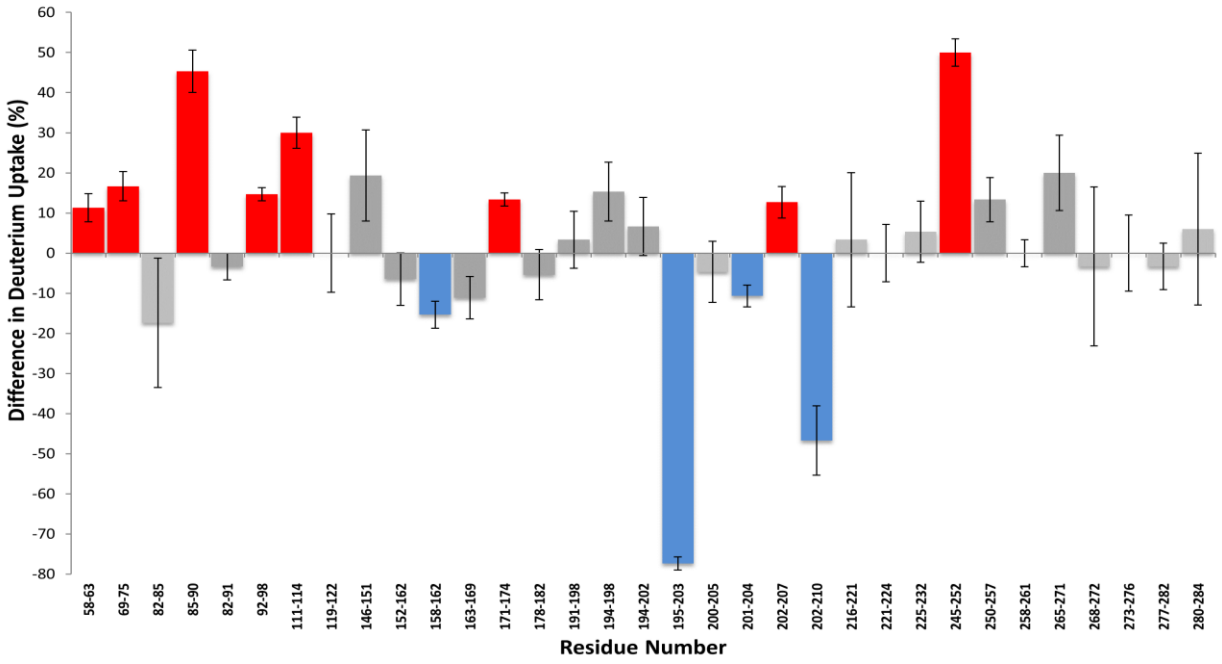

Supplemental Figure A2 Equilibrated Local HDX Coverage for TEM-1 with Cephalexin.

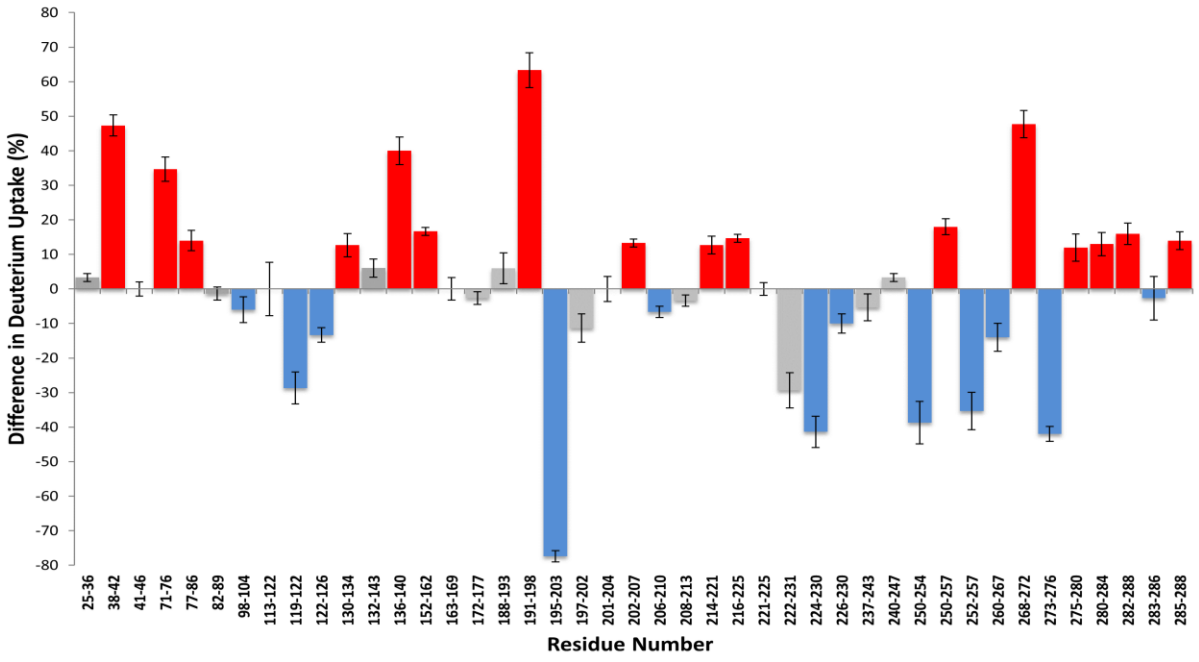

Supplemental Figure A3 Equilibrated Local HDX Coverage for TEM-1 with Clavulanate.

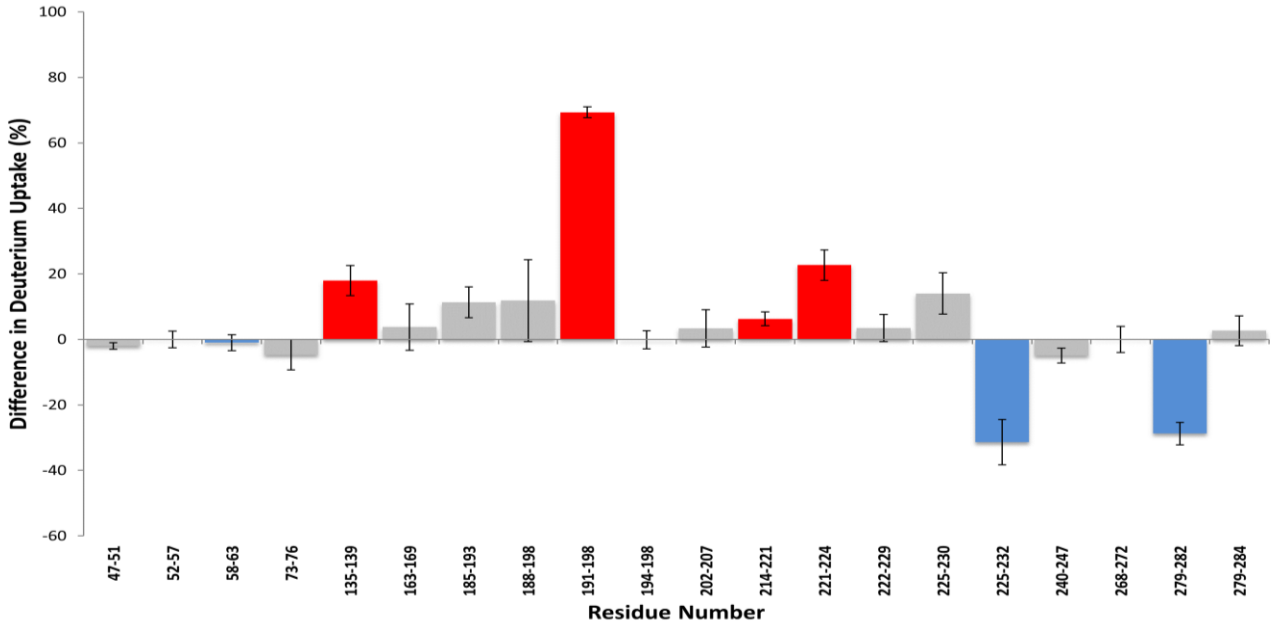

Supplemental Figure A4 Kinetic Local HDX Coverage for TEM-1 with Ampicillin after 0.34s of deuteration.

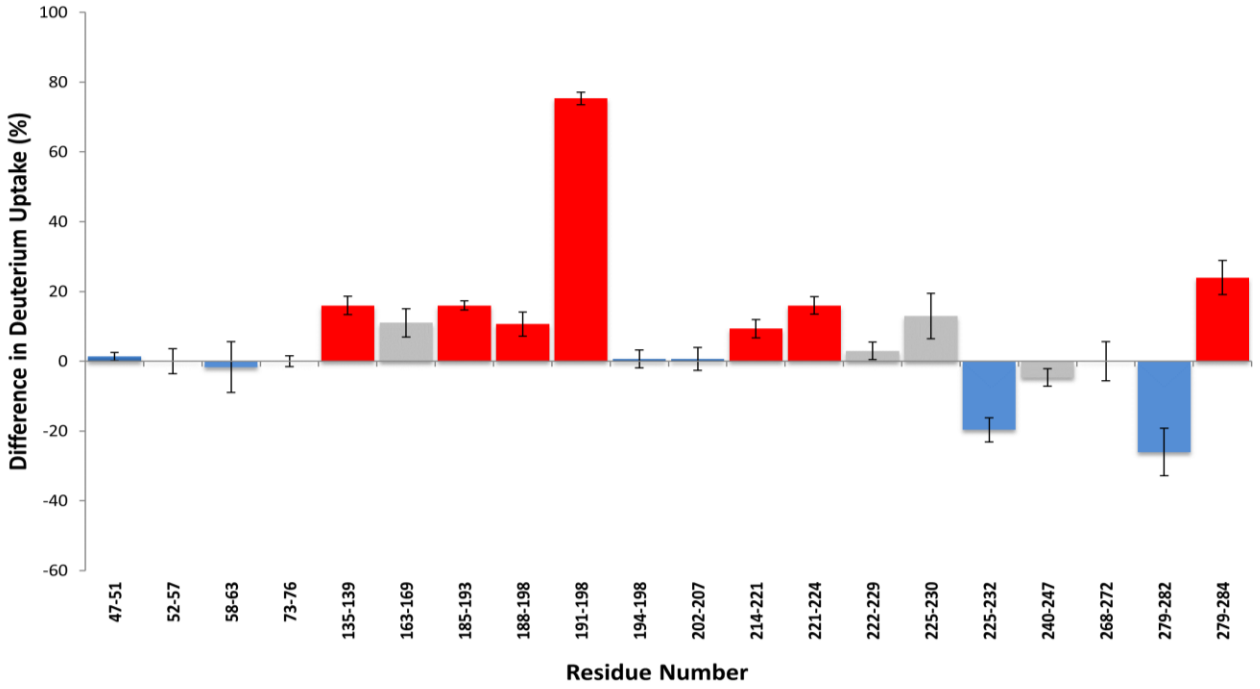

Supplemental Figure A5 Kinetic Local HDX Coverage for TEM-1 with Ampicillin after 0.63s of deuteration.

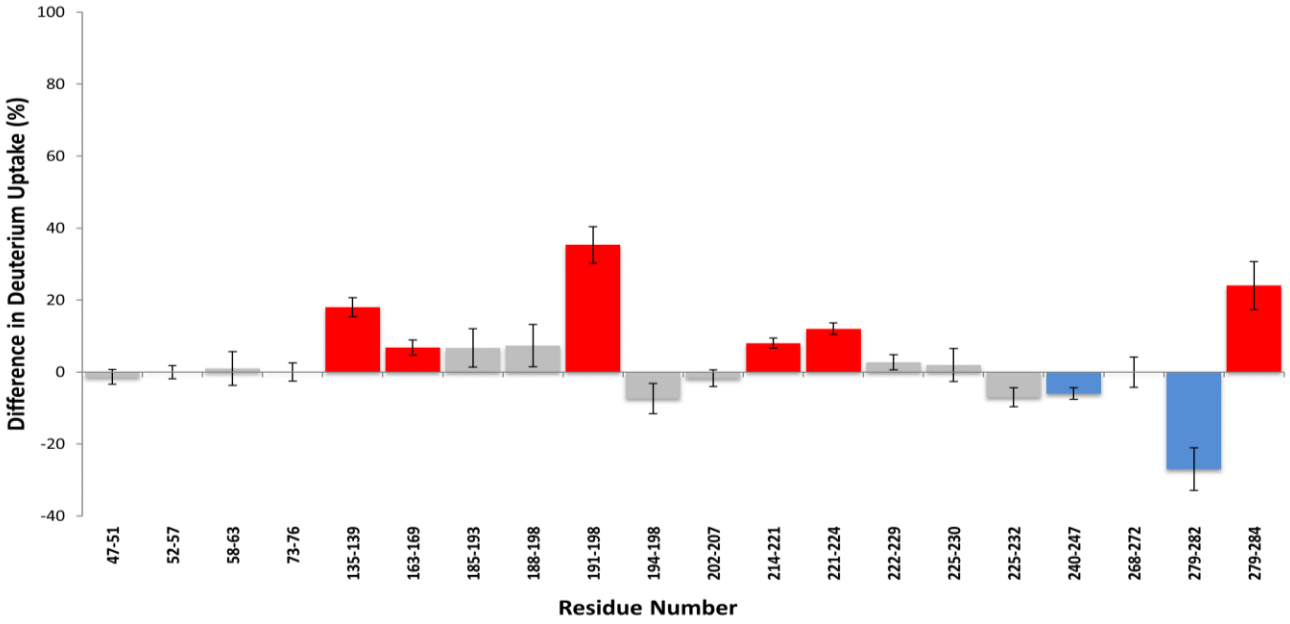

Supplemental Figure A6 Kinetic Local HDX Coverage for TEM-1 with Ampicillin after 0.88s of deuteration.

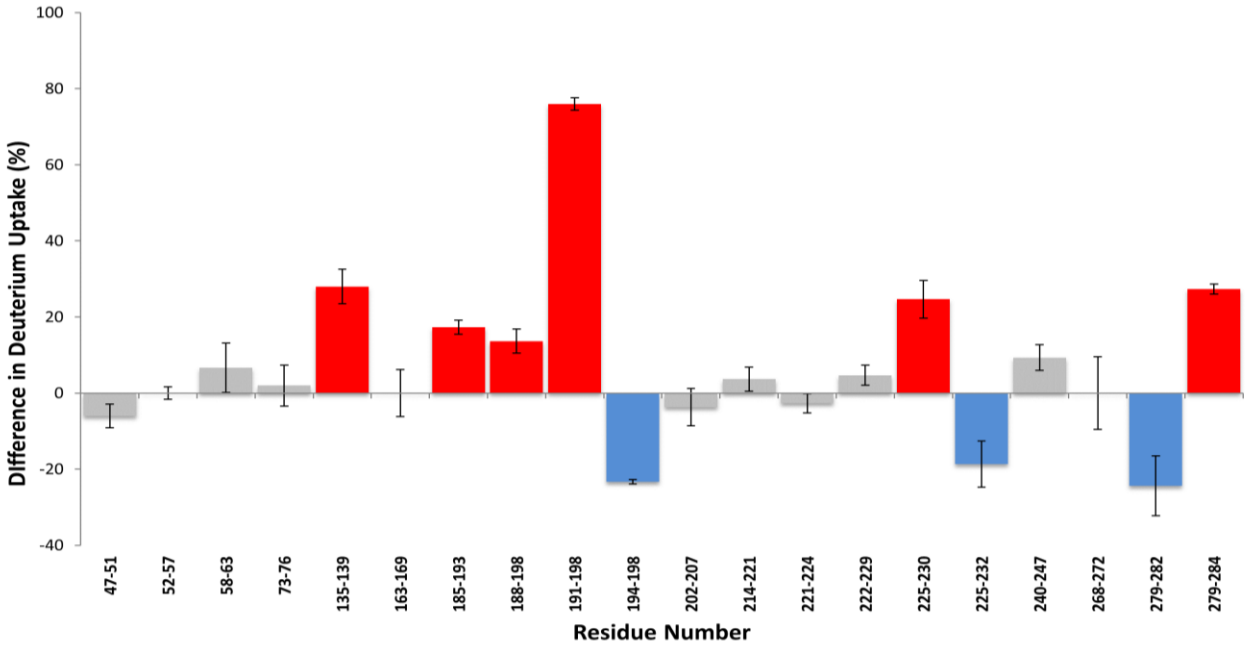

Supplemental Figure A7 Kinetic Local HDX Coverage for TEM-1 with Ampicillin after 1.54s of deuteration.

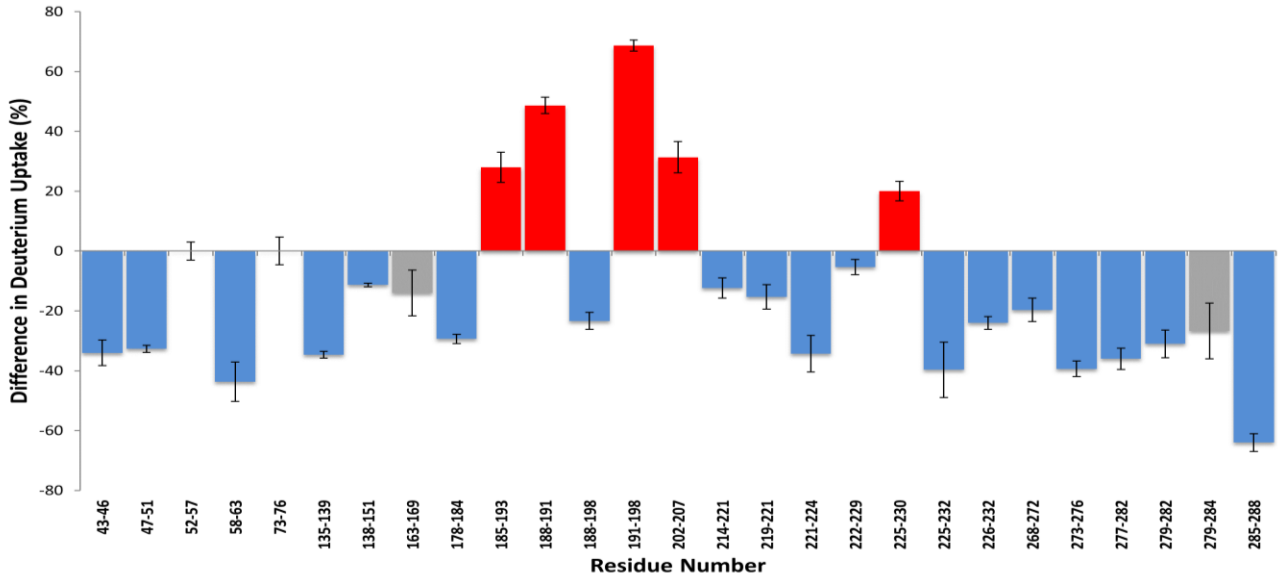

Supplemental Figure A8 Kinetic Local HDX Coverage for TEM-1 with Cephalexin after 0.34s of deuteration.

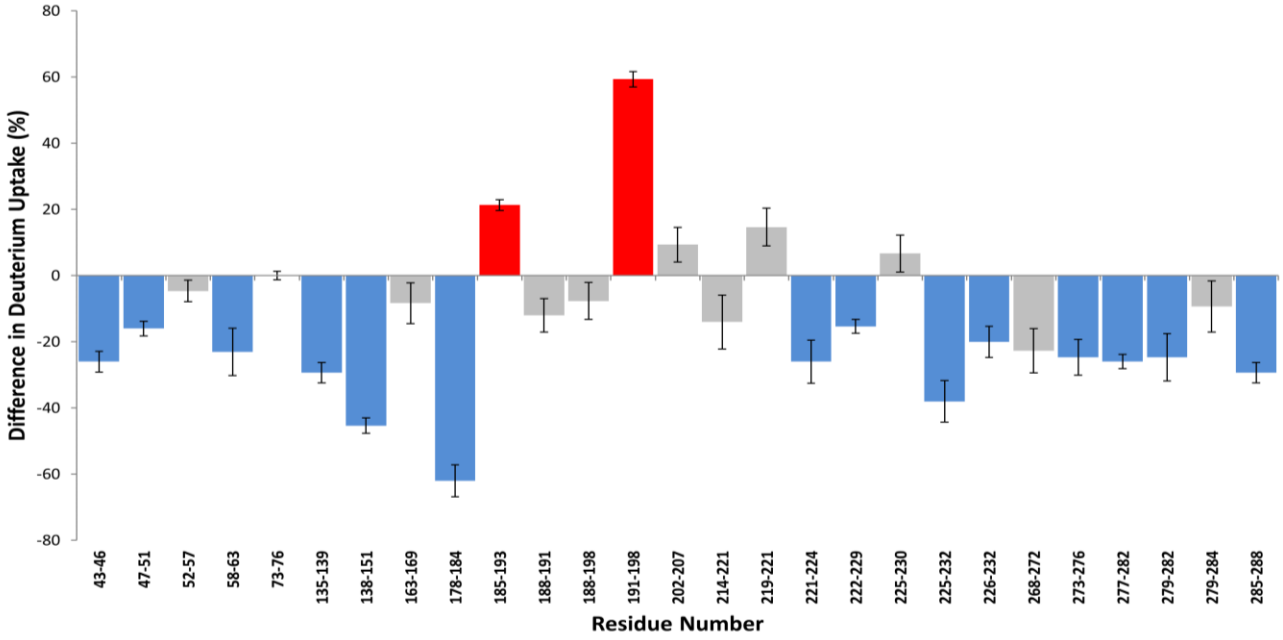

Supplemental Figure A9 Kinetic Local HDX Coverage for TEM-1 with Cephalexin after 0.63s of deuteration.

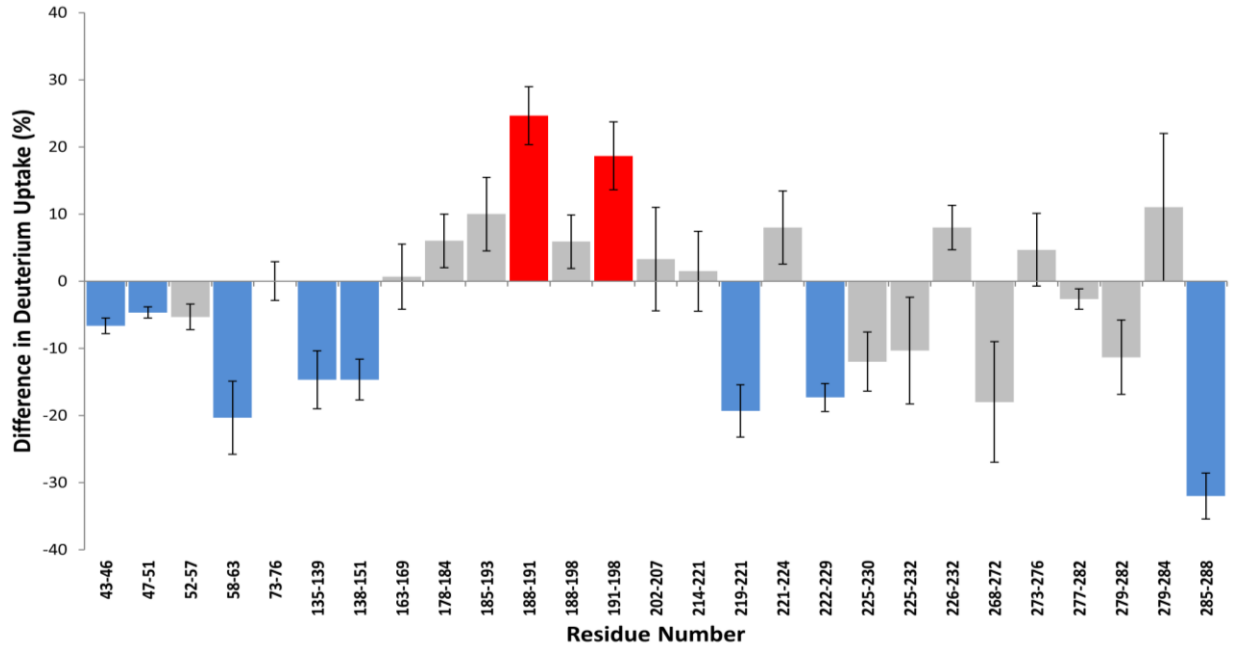

Supplemental Figure A10 Kinetic Local HDX Coverage for TEM-1 with Cephalexin after 0.88s of deuteration.

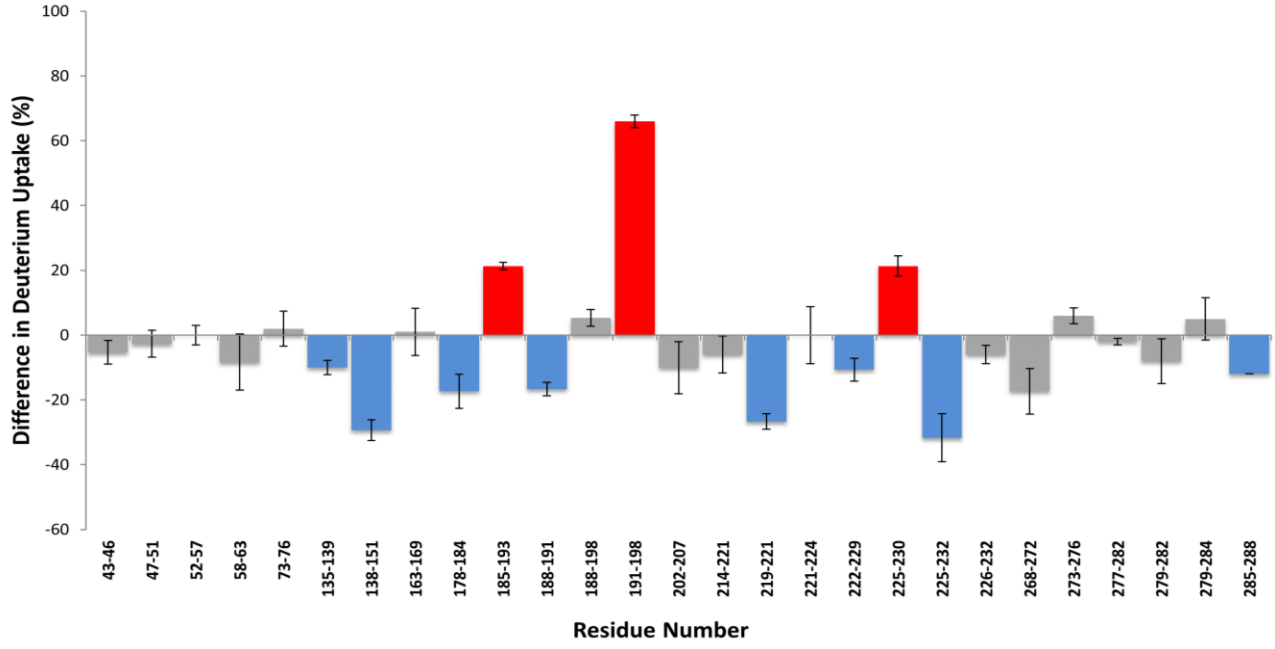

Supplemental Figure A11 Kinetic Local HDX Coverage for TEM-1 with Cephalexin after 1.54s of deuteration.

Appendix B

Supplemental Figures for Chapter 3

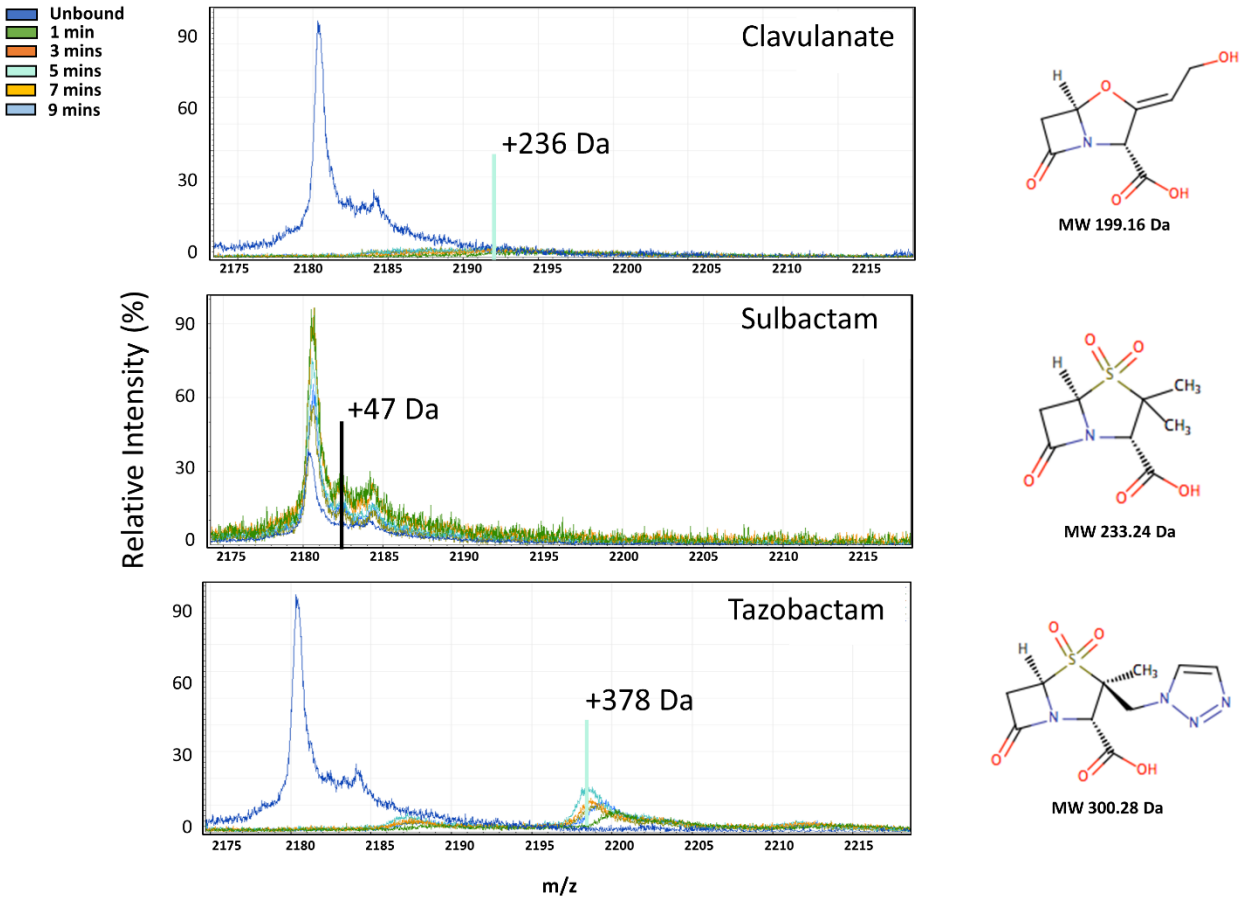

Supplemental Figure B1 Native mass spectra of TEM-1 incubated with each drug substrate at a ratio of 1000:1 inhibitor to TEM-1 on a shorter timescale. Protein spectra at 5 time points (1 min, 3 mins, 5 mins, 7 mins, 9 mins) are overlaid to demonstrate the small shifts in spectra noted over the time course.

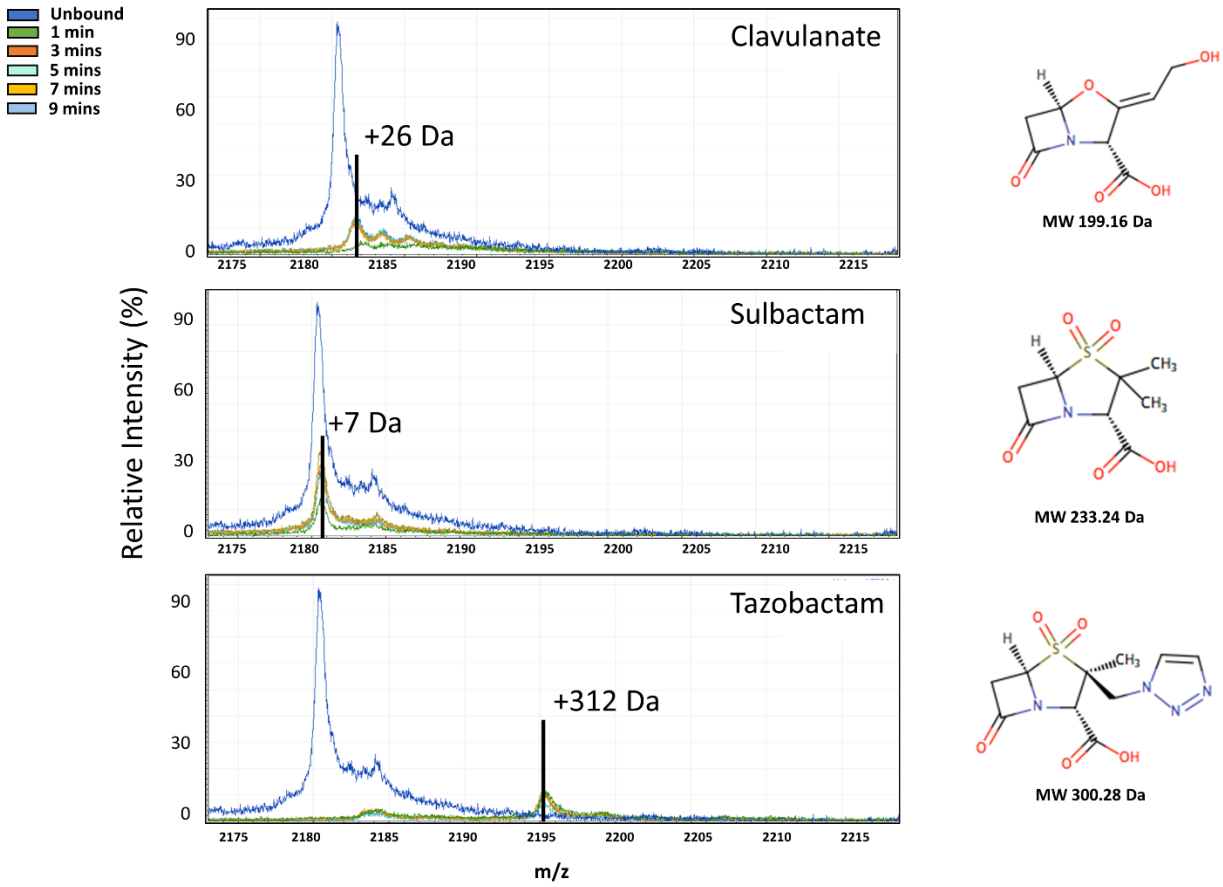

Supplemental Figure B2 Native mass spectra of TEM-1 incubated with each drug substrate at a ratio of 10:1 inhibitor to TEM-1 on a shorter timescale. Protein spectra at 5 time points (1 min, 3 mins, 5 mins, 7 mins, 9 mins) are overlaid to demonstrate the small shifts in spectra noted over the time course.

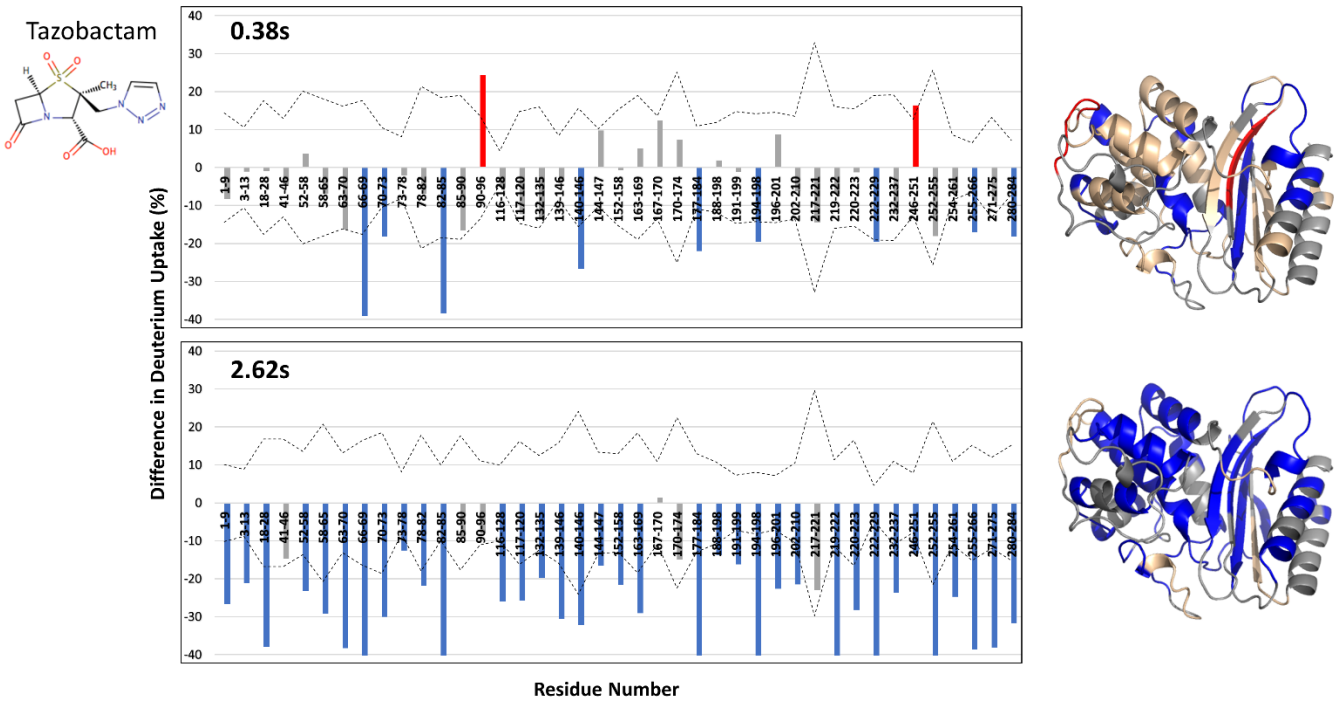

Supplemental Figure B3 Equilibrated Local HDX results for Tazobactam incubation (1000:1 ratio) at the first (0.38s) and last (2.62s) time points recorded using the TRESI setup with 10 minutes incubation prior to deuteration. Peptide fragments in colour (grey, insignificant; red, increasing; blue, decreasing) signify differences in deuterium uptake between the holo and apo enzyme forms (>2σ, dotted black line).Pymol image (PBD ID: 1BTL) displays the significant changes in dynamics. Regions with no significant change are displayed in gold, decreasing in blue, increasing in red and unrecorded regions are in grey.

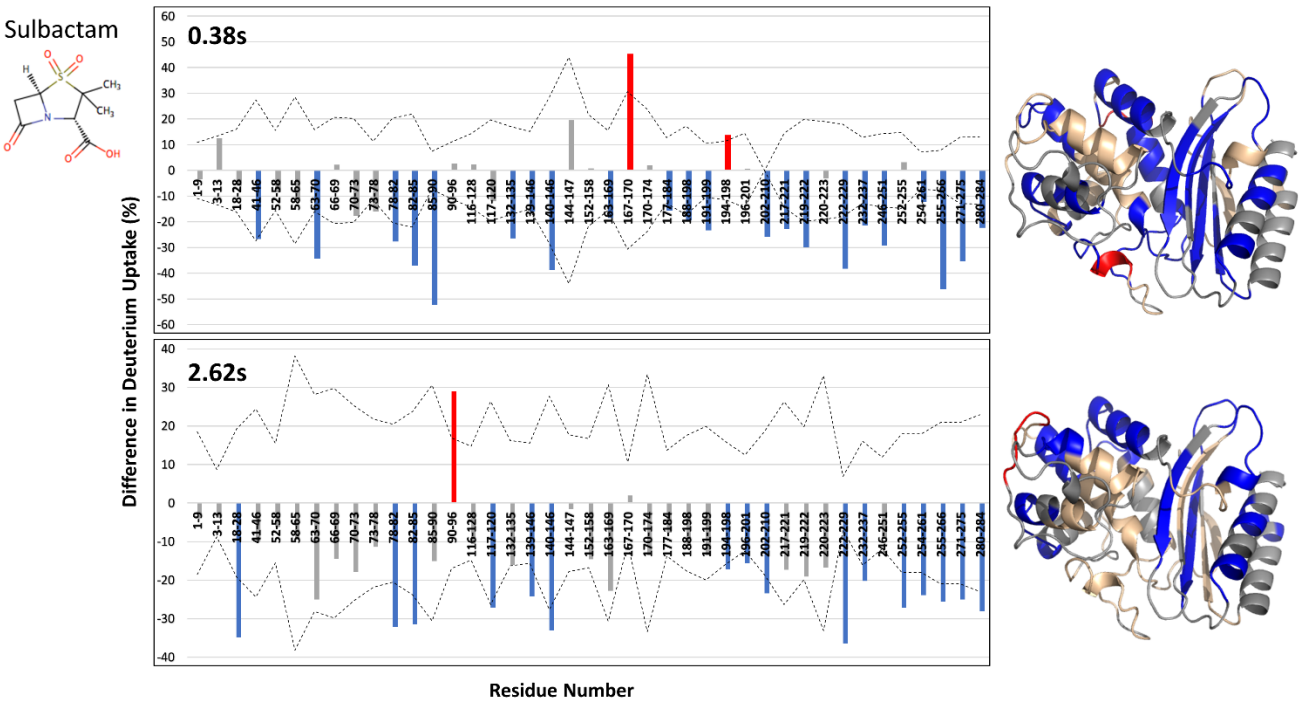

Supplemental Figure B4 Equilibrated Local HDX results for Sulbactam incubation (1000:1 ratio) at the first (0.38s) and last (2.62s) time points recorded using the TRESI setup. Peptide fragments in colour (grey, insignificant; red, increasing; blue, decreasing) signify differences in deuterium uptake between the holo and apo enzyme forms (>2σ, dotted black line).Pymol image (PBD ID: 1BTL) displays the significant changes in dynamics. Regions with no significant change are displayed in gold, decreasing in blue, increasing in red and unrecorded regions are in grey.

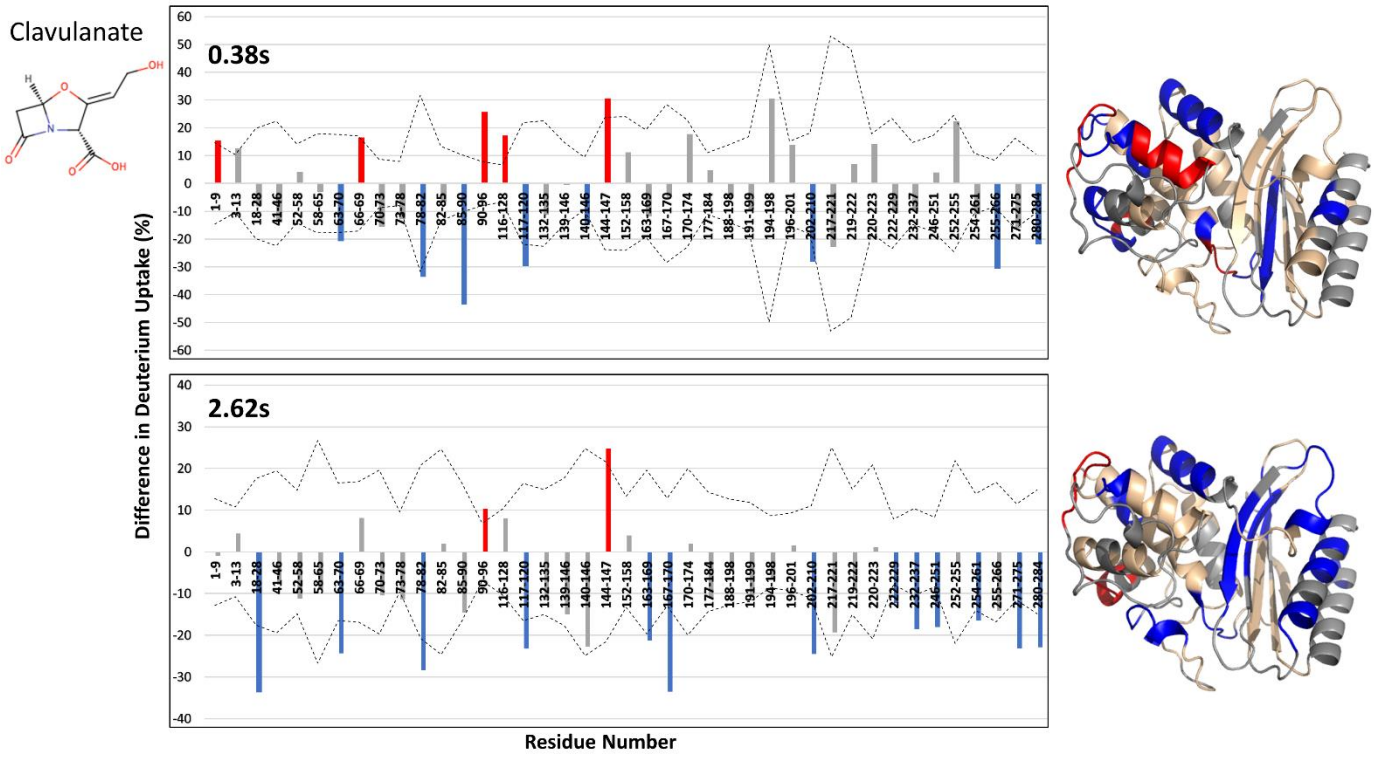

Supplemental Figure B5 Equilibrated Local HDX results for Clavulanate incubation (1000:1 ratio) at the first (0.38s) and last (2.62s) time points recorded using the TRESI setup. Peptide fragments in colour (grey, insignificant; red, increasing; blue, decreasing) signify differences in deuterium uptake between the holo and apo enzyme forms (>2σ, dotted black line).Pymol image (PBD ID: 1BTL) displays the significant changes in dynamics. Regions with no significant change are displayed in gold, decreasing in blue, increasing in red and unrecorded regions are in grey.

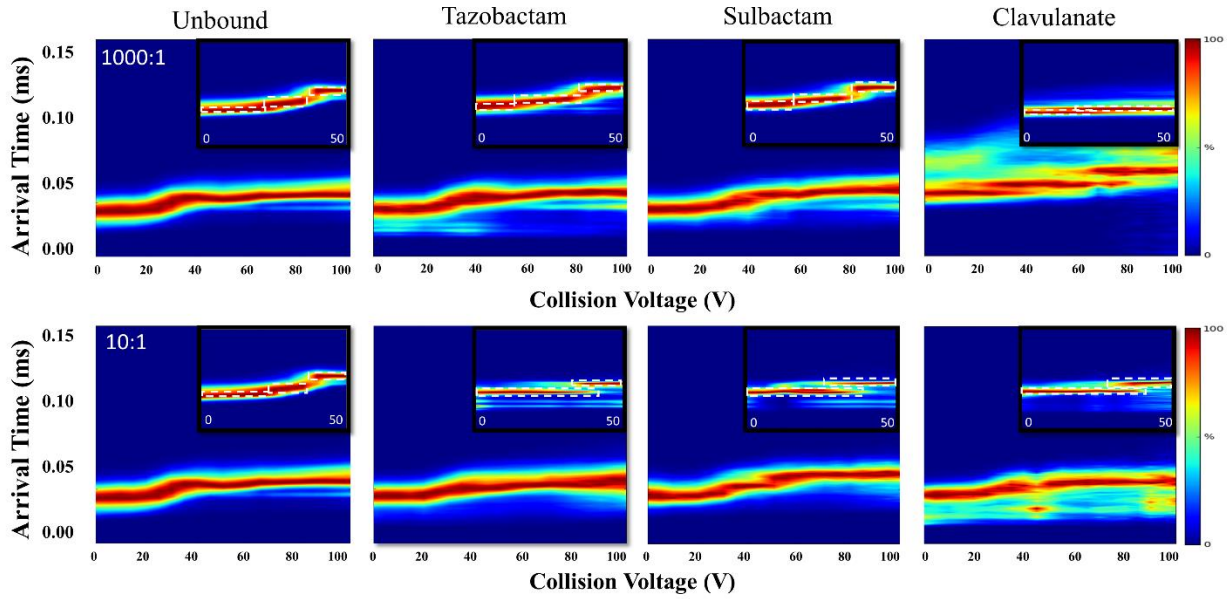

Supplemental Figure B6 CIU Heat Maps of Binding Affinity for TEM-1 and Inhibitors. Top) CIU spectra of inhibitor-bound TEM-1 for the 1000:1 experiment at collisional voltages from 0-100 V, taken in 5V increments. Inset into each CIU plot is a magnification of the unfolding conformations occurring in the lower 0-50 V range. Changes in folding states are outlined with the dotted white line. All spectra were recorded for the +16-charge state. Bottom) CIU spectra of inhibitor-bound TEM-1 for the 10:1 experiment, with identical voltage increments and charge state selection as the 1000:1 presentation.